Structural and Magnetic Phases in Pressure-Tuned Quantum Materials

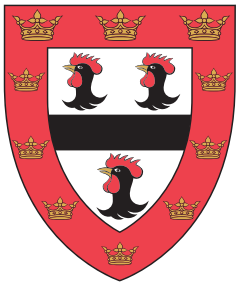

David Matthew Jarvis

Dr S. S. Saxena

Department of Physics
University of Cambridge

This thesis is submitted for the degree of
Doctor of Philosophy

Jesus College

September 2020

Declaration

This thesis is the result of my own work and includes nothing which is the outcome of work done in collaboration except as declared in the Preface and specified in the text. It is not substantially the same as any that I have submitted, or, is being concurrently submitted for a degree or diploma or other qualification at the University of Cambridge or any other University or similar institution except as declared in the Preface and specified in the text. I further state that no substantial part of my thesis has already been submitted, or, is being concurrently submitted for any such degree, diploma or other qualification at the University of Cambridge or any other University or similar institution except as declared in the Preface and specified in the text. It does not exceed the prescribed word limit for the relevant Degree Committee.

David Matthew Jarvis
September 2020

Abstract

Structural and Magnetic Phases in Pressure-Tuned Quantum Materials

David Matthew Jarvis

This thesis presents work exploring the use of pressure as a tuning parameter for exploring the phase diagrams and properties of magnetically ordered insulators, to add understanding to several areas of current interest in condensed matter research. It shows the versatility of pressure as an experimental technique for exploring material properties free from complicating factors which arise with similar techniques such as chemical doping.

The properties of low-dimensional magnetic materials, and how these systems respond as they are pushed toward a more three-dimensional nature is explored through studies of both the crystal and magnetic structures of the family of quasi-two-dimensional magnetic insulators $M\mathrm{PS_3}$ (M = Fe, Ni, Mn). With previous work largely being specific to individual compounds, this thesis contributes to a more unified understanding of their properties. It shows that Ni and $\mathrm{MnPS_3}$ undergo similar structural transitions under pressure to those previous observed in $\mathrm{FePS_3}$, the highest pressure of which is linked to an insulator-to-metal transition in that system. Through record high-pressure neutron diffraction measurements, the evolution of the antiferromagnetic order in $\mathrm{FePS_3}$ through this metallisation is studied for the first time. In contradiction to previous indirect measurements, it is seen that magnetism persists into the metallic phase, with long range antiferromagnetism giving way to a previously unobserved short-range order. This work is relevant on a broader scale for numerous layered magnetic materials such as cuprate high temperature superconductors.

Secondly, pressure is used to explore the magnetocaloric properties of the antiferromagnet $\mathrm{EuTiO_3}$. Recent work has shown that this compound compares favourably to many materials commonly used in magnetic refrigeration. Measurements show that these properties are suppressed by the application of pressure and point towards the potential existence of a previously undiscussed transition in the material between 0.4 GPa and 0.5 GPa.

Acknowledgements

There are many people to whom I owe sincere thanks for helping to make this work possible. I am extremely grateful to my supervisor Montu Saxena for his continual support, guidance and the many opportunities which I have had thanks to him. I would have very few results to discuss were it not for the constant support and endless patience of Cheng Liu, whose guidance has helped bring so much of this work to fruition. To Matt Coak and Phil Brown I am very grateful for not only their scientific contributions and exceedingly helpful software for analysis, but also for pulling me through and always being there with a positive word.

Members of QM, Siân Dutton, Patricia Alireza, Keiron Murphy, Jiasheng Chen and many others have always been incredibly generous in offering both advice and assistance and I have benefited no end from their range of expertise. With the facilities experiments in both planning and execution I am indebted to Andrew Wildes and Thomas Hansen at the ILL, Dominik Daisenberger at Diamond and Helen Walker at ISIS.

Thanks go to the friends I have made here at Jesus College and in Cambridge who have made my time spent here so enjoyable: Phil and Ruth, Harry and Olga, Ramsay and James, Taylor, Bee, Darren and many others. Thanks to Keenan (and Rory and Kiera) for keeping me sane in the latter stages of writing.

For helping me get here and for always supporting me in my research and the writing of this thesis I cannot express my gratitude enough to my wife Robyn who has listened to me tirelessly whether I have been excited or complaining. Finally, thank you to my parents, Andrew Jarvis and Amanda Williams, for always being behind me, encouraging my interest in science and helping me through everything to get to this point.

Table of contents

Chapter 1

Introduction

This thesis explores the effective use of pressure as a tuning parameter for exploring the phase diagrams of magnetically ordered materials. The effect of pressure is to tune the underlying crystal structure of the materials. This direct manipulation of the crystal lattice may induce a great number of changes in both magnetism and the electrical properties of materials, modifying for instance magnetic exchange parameters by changing the relative positions and separation of ions.

A key advantage of pressure as a tuning parameter for exploring physical properties lies in its cleanliness. Other comparable methods such as chemical doping or substitution may directly change the occupation of electronic bands in the material and thereby influence their electrical and magnetic characteristics. With the use of hydrostatic pressure, only the crystal structure itself is directly modified, and therefore any changes in other material properties arise from this changing of the atomic unit cell in real space. In this way, the energies of bands in the electronic structure are modified, giving rise to various measurable effects.

Such manipulation of physical systems allows for a great number of questions in condensed matter physics to be explored. A variety of model systems may be used to explore the behaviour of materials as high temperature superconductors, multiferroics and compounds exhibiting low-dimensional magnetic order.

1.1 Quantum Criticality

In using pressure as a tuning parameter in magnetic materials, the critical temperature for transitions between ordered and disordered states may be modified. The appearance of a quantum critical point follows from the continued suppression of a second order phase transition towards absolute zero temperature and brings to the fore several of the key aspects of the study of phase transitions in condensed matter physics. In a second order transition at

finite temperature, thermal fluctuations in the system are responsible for destabilising order in the system by overcoming the reduction in entropy for which the order is responsible, or the free energy in the system. A second order phase transition may be driven to lower temperature by some tuning parameter such that the transition occurs at zero temperature, arriving at a quantum critical point (QCP) in the phase diagram. At low temperatures near to this point, thermal fluctuations are negligible in energy and it is instead quantum fluctuations between the ordered and disordered state which act to destabilise order. In addition, as the QCP exists at zero temperature, the third law of thermodynamics requires that the ordered and disordered phase be of equal entropy. This implies the existence of some form of order in the "disordered" phase.

The fluctuations in a system's order parameter due to these quantum effects can result a number of emergent effects dependent on the nature of the material, which can persist up to unintuitively high temperatures despite the absolute zero temperature nature of their origin. Such effects include the emergence of unconventional superconductivity and other new forms of electric or magnetically mediated order.

Pressure has long been used as a tuning parameter to explore quantum critical phenomena in magnetically ordered systems. The suppression of either ferromagnetic or antiferromagnetic transition temperatures towards a quantum critical point at absolute zero temperature reveals the emergence of new behaviours including the emergence of unconventional superconductivity in, for example, the ferromagnetic pure system UGe_2[1]. A pressure-temperature phase diagram of this material is shown in figure 1.1.

This emergent superconductivity in UGe_2 is seen to coexist with the bulk ferromagnetism in the material, and whilst the trend of the magnetic transition temperature with pressure is continuous, the transition to a ferromagnetic state is seen to become first-order below the expected pressure of the QCP. This change prevents experimental access to the precise pressure of the QCP, due to it being an effect unique to second-order transitions.

Similar behaviour is observed in antiferromagnetic materials such as $CePd_2Si_2$ and $CeIn_3$ in which superconductivity similarly emerges around an antiferromagnetic QCP[2]. Besides superconductivity, other new electronic behaviour is revealed at high pressures such as changes in the behaviour of resistivity with temperature away from the metallic T^2 exponent expected from traditional Fermi liquid theory.

Quantum critical effects are not however limited to magnetic materials, with recent work using pressure to demonstrate a number of effects in ferroelectric materials[3, 4, 5]. Such work provides further examples of the coupling of quantum critical effects with other excitations in a system. Quantum effects are significant event at ambient pressures in the quantum paraelectric class of materials, existing under ambient conditions near to a

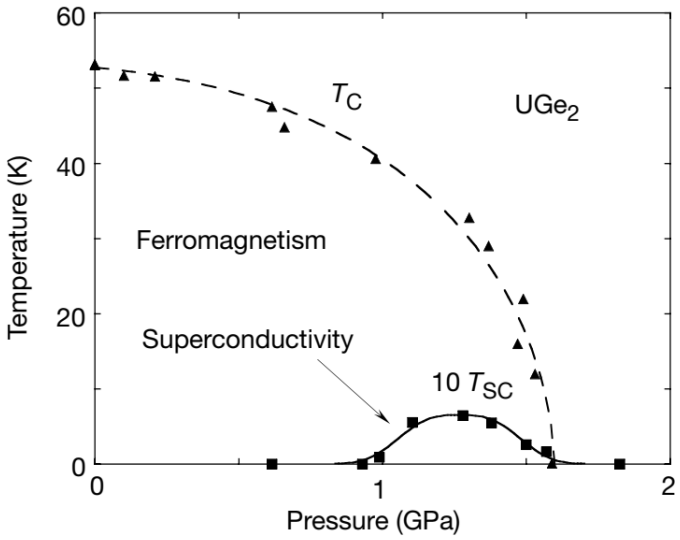

Fig. 1.1 Pressure-Temperature phase diagram of the heavy-fermion superconductor UGe_2. The emergence of superconductivity under pressure in this compound follows the suppression of the Curie temperature towards zero at a ferromagnetic quantum critical point. Taken from reference [1].

quantum critical point in their phase diagram. With electrons in these ferroelectrics being non-itinerant, the ferroelectric quantum critical point may be approached without the emergence of superconductivity or the transitions becoming measurably first order.

1.2 Low-dimensional Magnetic Materials

A particular class of magnetically ordered systems which have yielded a great deal of new physics under pressure is that of low-dimensional magnetic insulators. High-temperature cuprate superconductors are key examples of this in which an insulating antiferromagnetic phase is gradually suppressed, with unconventional superconductivity emerging as the ground state system appears to approach a quantum critical point.

The antiferromagnetic heavy-fermion compounds discussed previously are also relevant in this context. Side-by-side, $CePd_2Si_2$ and $CeIn_3$ illustrate the prediction from mean-field theory that magnetically mediated superconductive pairing becomes more robust on moving from a cubic to a more tetragonal symmetry[6, 7, 8, 9]. Both the maximum T_c and the pressure range over which superconductivity is observed is larger in the tetragonal $CePd_2Si_2$ than in CeIn which has a cubic symmetry. This evolution of pairing as ones moves away from a cubic system is taken to the extreme in materials like the high T_c superconductors

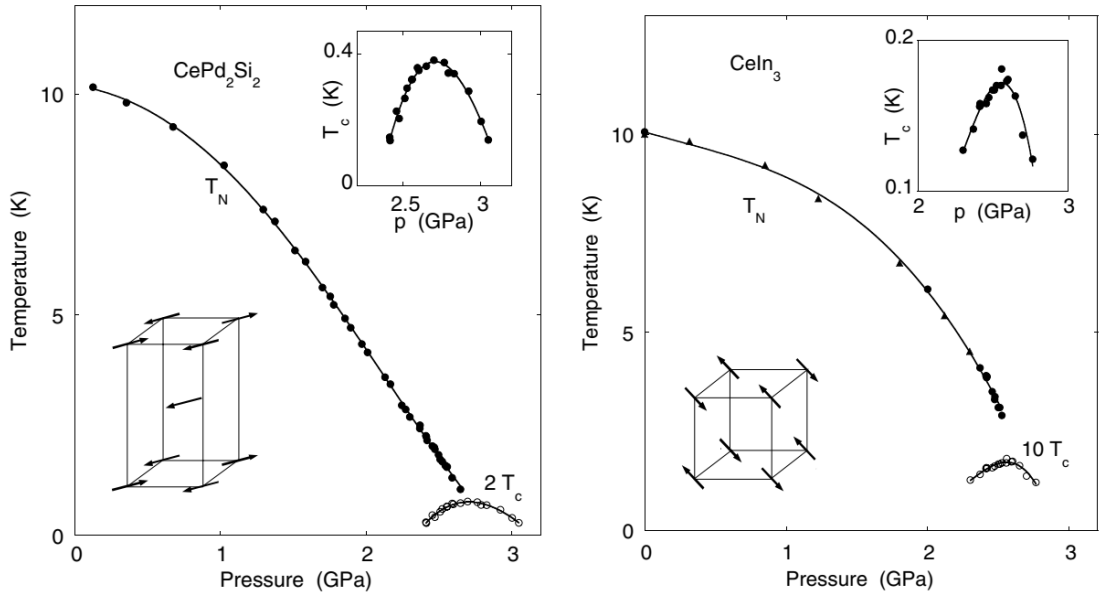

Fig. 1.2 Temperature-pressure phase diagrams for two antiferromagnetic systems which show superconductivity under pressure. Taken from reference [2].

which may be considered as quasi-two-dimensional systems with very limited interactions along one direction.

The phase diagrams of such cuprate high T_c superconductors are often very complex: with the suppression of antiferromagnetic order comes not only unconventional superconductivity but new behaviour at higher temperatures in the so called pseudogap regime which remains poorly understood, such as an unusual density of states at the Fermi energy. Whilst much work on the cuprate family of high-temperature superconductors has focussed on the use of chemical doping as a tuning parameter, pressure has previously been used in tandem to explore the phase diagram of these complex materials[10]. Pressure can be used to access regions of the phase diagram which are difficult to reach using chemical techniques, including the high doping terminus of the superconducting dome in YBCO which is above the maximum hole concentration which can be achieved with oxygen doping.

The phase diagrams of the aforementioned heavy-fermions are broadly simpler than those of the cuprate superconductors. As such, these systems can act as models for the effects of pressure and doping in more complex materials, with the important distinction that the heavy-fermion compounds are not insulating in the antiferromagnetic phase, which prevents some direct comparison.

The family of materials $M\mathrm{PS}_3$, where M is a first-row transition metal ion, provides a wide space for exploring how quasi-two-dimensional magnetic insulators respond in terms of magnetic, electric and structural properties as pressure is used to push them towards a more

three dimensional nature. In this instance this change is achieved as the separation of the weakly coupled van der Waals planes is more easily reduced than distances within the planes, resulting in inter-planar interactions no longer being effectively negligible. With a range of model magnetic behaviour from Heisenberg to Ising to more complex interactions achievable in this family by varying the transition metal species, the evolution of each of these systems under pressure may be studied. The use of pressure here again highlights the importance of the crystal structure for the properties of this family. New physics in both electric and magnetic order may be accessed solely through manipulation of the structure and phonons, without artificial changes of valence, bonding or other properties through such techniques as chemical doping.

Alongside their varied magnetic structures this family of materials exhibit interesting electrical behaviour, being either Mott or charge-transfer insulators which simple band calculations predict to be metallic but in experiment being extremely insulating under ambient conditions. Some of these insulating phases are seen to give way to metallic behaviour under pressure as good examples of Mott insulator-metal transitions. A great deal of work remains to be done however to explore how these transitions are related to observed structural transitions under pressure and how these differ between members of the family. The combination of behaviours in both magnetism and conduction allows for a great variety of physics to be tested in systems which are free from impurities and other more complex behaviours. A temperature-pressure phase diagram of $FePS_3$ is shown in figure 1.3, which shows the rich range of electrical and magnetic behaviour which accompanies structural transitions in the compound.

Consideration of the model of magnetically mediated superconductivity further motivates interest in the MPS$_3$ family of materials, being model two-dimensional antiferromagnets, which under pressure have been seen to become metallic. The observation of superconductivity under pressure alongside a structural transition in the related $FePSe_3$ supports the notion that these materials are an ideal space in which to explore magnetically mediated superconductivity alongside the crossover from two to three-dimensional magnetism. Many materials of interest which show high temperature superconductivity are extremely complex and are commonly affected by the presence of impurities and imperfections in the crystal lattice. This, combined with how the emergence of effects such as superconductivity can mask physics occurring in the underlying state, motivates study of simpler systems such as the MPS$_3$ family which share common behaviour of interest. More than this, the study of the phase diagrams of low-dimensional magnetic materials has revealed other new behaviours besides unconventional superconductivity. The action of pressure in these two-dimensional crystals to effectively push them towards a more three-dimensional character by modifying

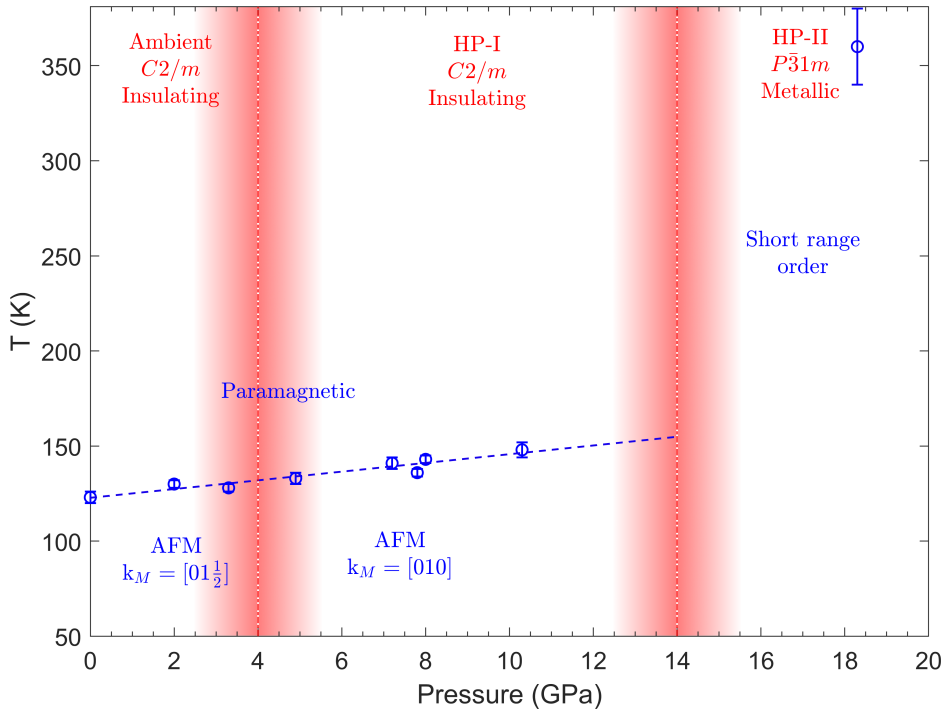

Fig. 1.3 Phase diagram of the quasi-two-dimensional antiferromagnet $FePS_3$. Changes in magnetic order accompany structural transitions under pressure as the system is pushed towards a more three dimensional nature. Metallisation coincides with the loss of long range magnetic order.

inter-layer spacing, is seen to be strongly linked to the observed Mott insulator-to-metal transitions and the emergence of superconductivity but the precise mechanisms of this link remain to be explored. Many parallels may be drawn then between simpler model systems of this type, and the more complex high T_c compounds as well as a number of other systems, beyond simply electric or magnetic order to a more complete understanding of the structures as a whole. Studying these compounds under extremes of pressure and temperature is an effective step between some of the previously examined simple model systems and materials such as the high temperature superconductors, and understanding here will help to shed light on this area of extensive current interest.

1.3 Magnetocalorics

The magnetocaloric effect has for many years been exploited in research as a companion and extension to other methods of cryogenic refrigeration. The adiabatic demagnetisation refrigerator (ADR), utilising the magnetocaloric effect in a cycle has a number of advantages over the use of liquid cryogens such as ^{4}He, ^{3}He and dilution refrigerators exploiting a mixture of these.

Foremost for ease of use, ADRs do not necessarily require a continuous supply of helium, and so when paired with other dry cryogenic technologies such as pulse-tube refrigerators, allow for cooling from room temperature to millikelvin temperatures with a closed loop system alone, removing requirements of cryogen transport and the recapturing of boil off vapour. In contrast, the cost for the use of these systems is predominantly the cost of electricity for powering helium compressors and magnet power supplies.

The base temperature of an ADR, effective starting temperature and other characteristics depend on the magnetocaloric properties of the material used in the system, and as such the choice of this pill material is vital for optimising the capabilities of an ADR system. With the use of these systems expanding not just in research but into more commercial purposes, it is desirable that systems can be designed for specific capabilities and lifespan. More than ever this motivates the study of materials for this use to allow for the magnetocaloric effect to be exploited. Alongside the development of new materials with this purpose in mind, the study of how existing materials may be tuned or modified to enhance their magnetocaloric properties is also of use, and through changing the magnetic exchange parameters by manipulation of the lattice, pressure is a valuable tool for exploring magnetocaloric materials in this way.

$EuTiO_3$ (ETO) has attracted interest in recent year for its favourable properties for use in magnetic refrigeration about the temperature required for the liquefaction of hydrogen. It has also been demonstrated that the magnetism in ETO is strongly linked to both its crystal

structure and the incipient ferroelectricity also present in the system, and each of these may be controlled by the application of a field which couples to the other systems.

Such perovskite oxides showing quantum paraelectricity have recently demonstrated new behaviour under pressure linked to the theoretical ferroelectric quantum critical point. The dependence of the dielectric behaviour on temperature is changed by coupling between the soft phonon which would give rise to ferroelectricity and and other phonon modes in the system. The addition of magnetism to this interaction is a valuable next step to build a proper theoretical framework, and this investigation will be valuable to examine such a material as ETO is suitable for the continued development of this theory. The near-multiferroic nature of ETO is also of interest in light of predictions of unusual coupling between the dielectric and magnetic when both systems are tuned towards their respective quantum critical points. Whilst achieving this may require the application of two or more tuning parameters such as an external electric field alongside pressure, studying how the magnetism in this compound is affected by tuning its crystal structure by hydrostatic pressure is valuable as a stepping stone to a full study of potential multiferroic quantum criticality in the system. Simultaneously, the lens of magnetocaloric properties is a valuable way to explore related magnetic properties in this compound.

This is again linked back to the magnetocaloric effect in ETO by work demonstrating an increase in magnetic entropy useful for cooling in materials driven towards magnetic quantum critical points[11, 12]. This concept has been demonstrated in magnetocaloric materials in both model low-dimensional systems and more typical three-dimensional magnets which are driven to a critical point by the application of magnetic field. The potential exploration of this effect in materials with an added layer of complexity in the form of potential charge ordering is further reason to to examine the magnetocaloric effect in materials such as ETO which are quantum paraelectrics and may potentially be pushed towards magnetic quantum criticality by turning parameters other than magnetic field.

Together the materials presented in this work present a valuable opportunity for exploring the coupling of magnetism and crystal structure in a range of both effective dimensionality and coupling between magnetic and electrical ordering. Furthermore, studying how magnetism evolves across metal-to-insulator transitions probes new physics which will be valuable for the study of emergent superconductivity in related compounds. To achieve this goal, a number of related developments in measuring both magnetic susceptibility and structure under extreme conditions will also be explored and implemented.

By examining both materials with low-dimensional magnetic order and those with significant magnetocaloric properties, the work presented here will explore how the direct

manipulation of the crystal lattice allows for exploration of new phases, and the discussion of new emergent behaviours in insulating magnetic systems.

Chapter 2

Theoretical background

2.1 Low-dimensional Magnetism

For the case of localised wavefunctions where the hopping integral is small, a Heisenberg Hamiltonian may be used to describe the magnetic systems. Thus it is most applicable for insulators, and metals are not well described with it.

The magnetic exchange parameter in this model may be written as

$$J \simeq 2J_D - 4\frac{t^2}{U} \tag{2.1}$$

where J_D is the exchange integral responsible for ferromagnetism in the systems and t is the small hopping integral which leads to antiferromagnetism.

A Heisenberg Hamiltonian for two spins may be defined as

$$H_H = -J\underline{S}_1 \cdot \underline{S}_2 \tag{2.2}$$

which can equally be rewritten as

$$H_H = -J\left(S_{1x}S_{2x} + S_{1y}S_{2y} + S_{1z}S_{2z}\right). \tag{2.3}$$

This can be further generalised by allowing for variation of the relative strengths of the x, y and z components as

$$H = -J\left[\alpha\left(S_{1x}S_{2x} + S_{1y}S_{2y}\right) + \beta S_{1z}S_{2z}\right]. \tag{2.4}$$

The nature of the Hamiltonian then depends on the values of the constants α and β. $\alpha = \beta = 1$ recovers the isotropic Heisenberg Hamiltonian; $\alpha \neq \beta \neq 0$ an anisotropic Heisenberg; $\alpha = 1$, $\beta = 0$ the XY Hamiltonian and $\alpha = 0$, $\beta = 1$ the Ising Hamiltonian.

2.1.1 Metal-Insulator Transitions

Separation between insulating and conductive behaviour may be initially seen in the approximation of nearly free electrons in crystalline materials[13]. In this model insulators are materials where all energy bands are completely empty or filled, due to the fact that for every state with wave function $\psi = e^{ikx}u(x,y,z)$ there is also an occupied state with $\psi = e^{-ikx}u^*(x,y,z)$. Contrarily, materials in which one or more energy bands are partially filled are metals. This filling arises from the exclusion principle as only two electrons, spin up and down, may occupy the same orbital state. States are filled up to the Fermi energy and momentum, E_F and k_F.

In the insulating case, there will be a finite energy gap Δ between the highest energy filled band and the lowest energy empty band, termed the valence and conduction bands respectively.

One may consider the transition from insulating to metallic behaviour in this simple model as the reduction of the energy gap Δ to zero by some manipulation of the potentials arising from the crystal structure. This may be achieved experimentally by the reduction of the unit cell volume by the application of pressure. This will result in a discontinuous change in the number of mobile charge carriers in the material and resultantly in conduction.

Such a model neglects interaction between charge carriers and resultantly predicts metallic behaviour in some materials which are experimentally seen to be insulating. Furthermore in these strongly correlated systems, it is observed that tuning the bandwidth or filling can induce metallisation, suggesting competing interactions which include electron-electron interaction in these systems. Two classes of such materials are Mott and charge transfer insulators.

The Hubbard Model

The Hubbard model describes transitions between insulating and metallic physics in such systems. A Hamiltonian for an array of single electron centres may be defined as[14]:

$$\hat{H} = \sum_{i,j} t_{ij} a_{i\sigma} a_{j\sigma} + U \sum_{i} n_{i\uparrow} n_{i\downarrow} \tag{2.5}$$

where t is the hopping integral, subscripts i and j refer to nearest neighbour sites, $a_{i\sigma}$ is the creation operator for site i and spin direction σ, $n_{i\uparrow(\downarrow)}$ is the number of electrons on site i with spin up (down), and U is the intra-atomic interaction defined as

$$U = \left\langle \frac{e^2}{r_{12}} \right\rangle = \int\int \frac{e^2}{R_{12}} \left|\psi(r_1)^2\right| \left|\psi(r_2)^2\right| \mathrm{d}^3x_1 \, \mathrm{d}^3x_2 \tag{2.6}$$

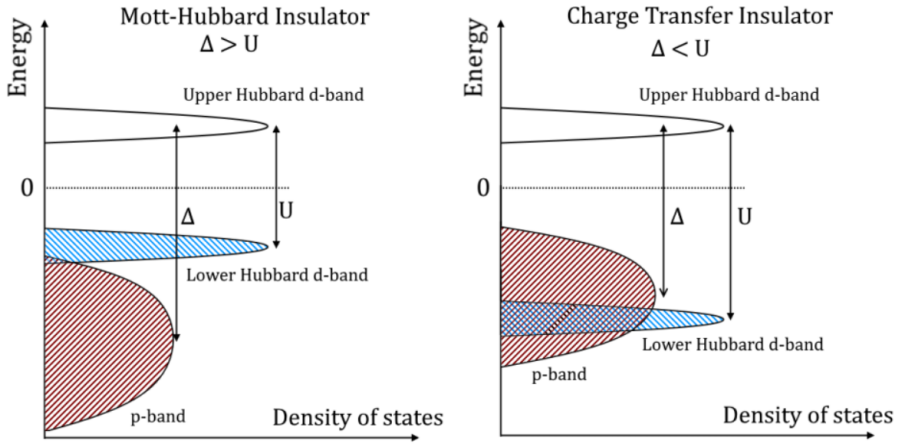

Fig. 2.1 Band structure schematic for typical Mott (left) and charge-transfer (right) insulators. The zero value of the energy axis is defined as the Fermi energy of the system.

where braces average over a single site and $\psi(r)$ is the electron wave function on the site. The second sum in equation 2.5 is non-zero only if both an up and down spin electron are present at site i, and the Hubbard U is an intra-atomic energy cost for this double occupancy.

The conductive behaviour of the system is thus determined by competition of the energy scales determined by t and U in equation 2.5. For the case $t \gg U$, the intra-atomic energy cost is negligible as is the on-site repulsion and the standard half-filled band conduction model is recovered[15].

For the case $t \ll U$, electrons are localised one to each site and the system is insulating. This case also results in the sites having non-zero net magnetic moments, giving rise to antiferromagnetic order with an exchange integral dependant on the hopping integral and intra-atomic interaction as $J = \frac{4t^2}{U}$.

These two extremes of t and U, then in the simplest case correspond to a non-magnetic metal and an antiferromagnetic insulator. The intermediate case where the magnitudes of t and U are similar is not rigorously solved and remains of interest.

For large U, Hubbard showed that the half-occupied band will split in two to an upper and lower band separated by an energy gap equal to U (or more fully $U - \frac{1}{2}(W_1 + W_2)$ where $W_{1,2}$ are the bandwidths of the two bands, being much smaller than U). A schematic of this is shown in figure 2.1.

Insulator to metal transitions in systems such as this can be induced in a similar manner to that previously discussed for the simple non-interacting case. Pressure or doping may be used to reduce U to the point where the two Hubbard bands to overlap, giving an effective metallic band structure: this is a Mott transition.

Other compounds exhibiting similar behaviour are transition metal compounds in which the Hubbard U splits the half-filled d-band of the transition metal ion. In this case, the ligand p-band in the material lies closer in energy to the upper Hubbard band than the lower Hubbard band does. The energy gap is therefore between the ligand p-band and the upper Hubbard band, and this hopping mechanism will determine the conduction in the system. The energy gap between these states is denoted Δ and is smaller than the Hubbard U in these materials. Being dependant on the species involved, Δ may be tuned by the chemistry between the anion and cation. Commonly these materials have a p-band ligand between metal ions in their unit cell, like sulphur in the $M\mathrm{PS}_3$ family. As Mott-Hubbard insulating behaviour describes electron transfer between metal sites in separate unit cells, such a charge-transfer insulating description is appropriate for electron transfer between anion and metal ions.

In both Mott and charge-transfer insulators, there is the potential for the emergence of new physics around metallisation. Fluctuations in the crystal and magnetic structure have the potential to couple to the new conduction electrons, which may themselves be correlated, potentially leading to electronic states not seen at ambient conditions or the emergence of superconductivity in this class of materials.

2.2 Magnetic Superexchange

In a number of magnetic materials, the interactions between magnetic ions does not occur directly, but is instead mediated by either conduction electrons or other ions in the system.

A common example of this, which is relevant for the transition metal $M\mathrm{PS}_3$ compounds is that of two magnetic d orbitals linked by the p orbital of another ion (the pathway Fe-P-Fe in FePS_3 for example).

The nature of the overall interaction in this case depends on the relative orientation of these orbitals and its effect on the electron configurations in accordance with the Pauli exclusion principle. This is described by the Goodenough-Kanamori rules, which state that magnetic interactions between two magnetic d ions connected by a p ion depends on the angle of the pathway d-p-d[16].

180° gives maximum overlap of the d and p orbitals and so maximum hopping. Possible spin arrangements in this case give antiferromagnetic interaction. For the 90° case of orthogonal d and p orbitals, there is zero overlap and only one possible spin configuration, which gives ferromagnetic interaction between the magnetic ions.

For the case of a d ion surrounded by an octahedron of p ions, these two cases are equivalently stated as the octahedra around two d ions being corner sharing, giving the

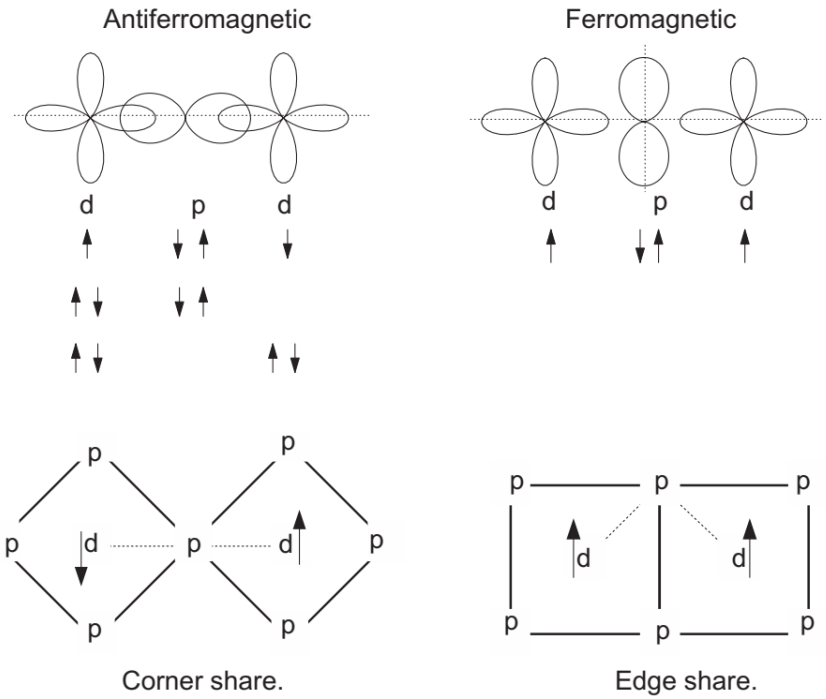

Fig. 2.2 Schematic depiction of the Goodenough-Kanamori rules for magnetic superexchange for the case of two d orbitals connected by ligand p orbitals. Adapted from reference [16].

antiferromangnetic 180° case; or edge sharing, giving rise to the ferromagnetic 90° case. This is illustrated in figure 2.2.

2.3 Quantum Criticality

The existence of a quantum critical point follows from the suppression of a second order phase transition to zero temperature by the application of some tuning parameter. This has been discussed for some time in the framework of magnetic ordering in metallic systems, and more recently for the case of electrical ordering in insulating quantum paraelectrics[3, 17].

Quantum critical phenomena in both classes of systems may be intuited from a mean-field theoretical approach to the phase transition[18]. The Landau theory of phase transitions approaches this by the consideration of some ordering parameter which is for temperatures above the transition and takes some finite value below the transition temperature. This is the magnetisation and polarisation for ferromagnetic and ferroelectric systems respectively. Taking first the Landau free energy for a ferromagnetic system as

$$F = \frac{a}{2}M^2 + \frac{b}{4}M^4 - \frac{c}{2}(\nabla M)^2 - HM \tag{2.7}$$

a magnetic equation of state may be derived as a function of the magnetisation, M by minimising with respect to this order parameter.

$$H(M) = aM + bM^3 - c(\nabla^2 M) \tag{2.8}$$

From this the linear term of coefficient a is observed as the linear susceptibility in a paramagnetic phase at temperatures above a ferromagnetic transition. a is an enhancement to the bare Pauli susceptibility of a non-interacting case. The magnetic susceptibility may be defined from this equation as

$$\chi_M = \frac{M}{H} = a^{-1} \tag{2.9}$$

where H is an external magnetic field strength.

For a system near to a transition where critical fluctuations are relevant, the dependence in both space and time of the magnetisation in the system as well as the external field must be considered. By the introduction of a random small change, H and M become $H+h$ and $M+m$. Taking averages and following the same approach as for the static case arrives at a modification to the linear term from a to $a+3b\bar{m}^2$.

The expansion of this method to vector fields gives modifications which depend on the time derivative of the fluctuation m. Discussed in terms of a harmonic oscillator, the variance of the fluctuation amplitude may be derived through Nyquist's theorem as

$$\bar{m^2} = \frac{2}{\pi}\int_0^\infty \mathrm{d}\omega \left(\frac{1}{2} + n_\omega\right) Im\alpha_\omega, \tag{2.10}$$

where n_ω is the Bose function.

The fluctuation amplitude of equation 2.10 may subsequently be split into contributions arising from the thermal and zero point motions as

$$\bar{m^2}_T = \sum_q \bar{m^2}_q \tag{2.11}$$

and

$$\bar{m^2}_q = \frac{2\hbar\gamma_q}{\pi}\int_0^\infty \frac{\omega n_\omega}{\omega^2 + \Gamma^2}. \tag{2.12}$$

From these, properties such as the heat capacity and resistivity may be calculated. The observable effect on materials tuned close to a quantum critical point is an increase in

the effective dimensions of the problem due to the inclusion of the dynamics of the order parameter field. The purely fluctuational terms are most relevant in lower dimensions and lead to the constraint that the mean field theory is applicable when the effective dimensionality of the system

$$d_{eff} = d + z, \tag{2.13}$$

where d is the spatial dimensions and z the dynamical exponent, is greater than four. The resultant predictions for measurable quantities that this spin fluctuation theory makes (in terms of critical exponents of temperature) are determined by the dimensions of the system, its fluctuation spectrum and the dispersion relation. Measurement of the critical exponents requires experimental access to specific regions of the phase diagram close to the quantum critical point. In temperature it requires cooling to the point where classical thermal excitations no longer dominate the dynamics of the system; and the application of some other tuning parameter to suppress the transition temperature to near absolute zero such that the quantum critical effects are the dominant dynamics in the system.

Antiferromagnetic systems may be understood in a broadly similar manner starting from a mean field approach by considering two separate magnetic sublattices which are each internally ferromagnetic with a specific positive mean field parameter, but which are coupled together through a negative mean field parameter which causes them to be aligned oppositely.

Quantum Paraelectricity

Starting from the magnetic case described above, quantum critical phenomena may also be approached in other ordered systems. For the case of (anti)ferroelectrics, in which the order parameter is the electrical polarisation, **P** rather than the magnetisation **M**, the emergence of quantum critical effects and the impact of critical fluctuations may be understood in a similar manner to in magnetic systems. A schematic phase diagram of this type of ferroelectric system is shown in figure 2.3.

Quantum criticality in ferroelectrics is interesting however for its differences from that in electrically conductive magnetic systems due to the fact that in ferroelectrics the electrons are fully localised, and as such relevant effects including those arising from quantum fluctuations are due to the crystal structure itself and mediated by phonons.

The dielectric properties of quantum paraelectrics away from quantum critical points are well described by Barrett[19] by

$$\chi = \frac{M}{\frac{1}{2}T_1 \coth(T_1/2T) - T_0} \tag{2.14}$$

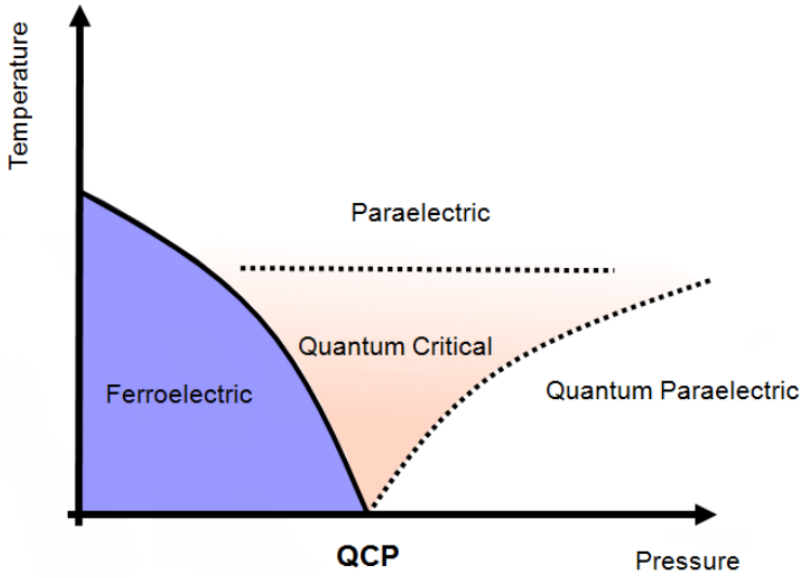

Fig. 2.3 Schematic phase diagram for ferroelectric systems. With the application of some external tuning parameter, the ferroelectric critical temperature, T_c is suppressed toward zero. Beyond this at low temperatures, a quantum paraelectric phase arises in which quantum fluctuations rather than thermal fluctuations are responsible for disrupting potential ferroelectric order.

where M is an effective Curie constant, T_0 is an effective Curie temperature and T_1 is a crossover temperature below which quantum effects are important. For high temperatures $T \gg T_1$, this equation reduces to a susceptibility of the Curie Weiss form $\chi = \frac{M}{T-T_0}$. M, T_0 and T_1 are described fully in the reference. In this region of the phase diagram, long-range order is destabilised not by thermal fluctuations as in the high temperature classical paraelectric phase, but by the quantum zero-point motion. This quantum paraelectric state is distinct from the dielectric behaviour close to the quantum critical point, where χ follows a T^{-2} behaviour. As with the moving from the classical high temperature paraelectric behaviour to the quantum paraelectric case, this is not strictly a phase transition, but a gradual crossover of the strengths of the relevant energy scales.

2.4 The Magnetocaloric Effect

The magnetocaloric effect (MCE) describes the change in temperature of a material induced by the change of an applied magnetic field. Thermodynamically this may be considered in terms of the internal energy of the system U, the entropy S, the volume V and the magnetic field H. The total differential of U may be expressed in the form

$$\mathrm{d}U = T\,\mathrm{d}S - p\,\mathrm{d}V - M\,\mathrm{d}H \tag{2.15}$$

where T is temperature and p pressure. $M\,\mathrm{d}H$ here may equivalently be replaced by $H\,\mathrm{d}M$.

Similarly the total differential of the entropy of a magnetic system may be expressed as

$$\mathrm{d}S = \left(\frac{\partial S}{\partial T}\right)_{H,p} \mathrm{d}T + \left(\frac{\partial S}{\partial H}\right)_{T,p} \mathrm{d}H + \left(\frac{\partial S}{\partial p}\right)_{T,H} \mathrm{d}p \tag{2.16}$$

which under the assumption of a process being both adiabatic and isobaric (conditions being realised in experiment) yields the magnetocaloric effect as in equation 2.17.

$$\mathrm{d}T = -\frac{T}{C_{H,p}} \left(\frac{\partial M}{\partial T}\right)_{H,p} \mathrm{d}H \tag{2.17}$$

where $C_{H,p}$ is the heat capacity at constant pressure and magnetic field[20].

This may be exploited for adiabatic demagnetisation refrigeration (ADR) using the following cycle, illustrated in figure 2.4. In the first stage, some quantity of paramagnetic salt is isothermally magnetised by the application of a external magnetic field (shown as the isotherm $a \to b$ in figure 2.4). This represents a reduction in the magnetic entropy and the total entropy of the system. Through this process heat $\Delta Q = T_1 \Delta S$ is removed from the system. In practice this is realised by the magetocaloric pill increasing in temperature when it is magnetised. The magnetically generated heat is then removed from the system, allowing it to return to its original temperature.

From this state, the applied magnetic field is adiabatically reduced to zero. As it is an adiabatic process, the total entropy of the system remains constant. The magnetic entropy is increased, requiring that the entropy associated with the system temperature decreases. As a result the system is cooled (the adiabat $b \to c$ of figure 2.4), to a final temperature $T_2 < T_1$ and the adiabatic temperature change is $T_{ad} = T_1 - T_2$. Experimentally this step requires conditions as close to adiabatic as is possible. In contrast to the first where the magnetocaloric must be in good thermal contact with the environment to lose the heat, this requires that the pill and sample stage be thermally decoupled from their surroundings. This change is achieved through a "heat switch", either superconducting, mechanical or gas based.

Materials used for their magnetocaloric properties may thus be evaluated by the comparison of three parameters particular to the material: the isothermal magnetic entropy change ΔS_{mag}, the adiabatic temperature change T_{ad} and the refrigeration capacity, RC, defined as

$$\mathrm{RC} = \int_{T_1}^{T_2} \Delta S\,\mathrm{d}T \tag{2.18}$$

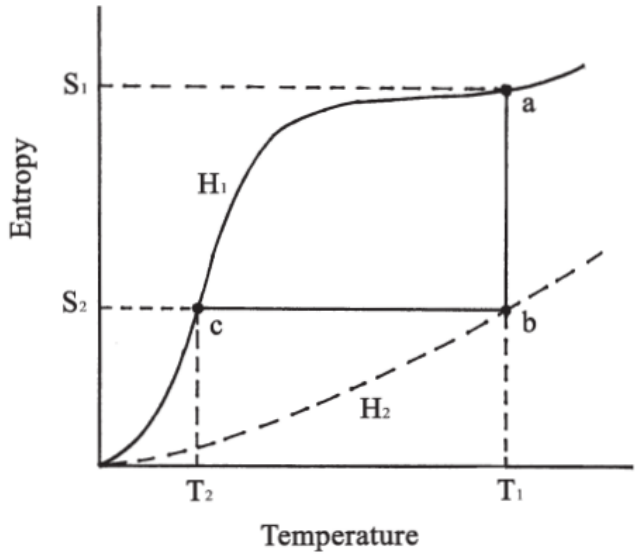

Fig. 2.4 Total entropy of a paramagnetic system as a function of temperature for zero (H_1) and non-zero (H_2) applied magnetic field. Taken from reference [20].

where T_1 and T_2 are the temperatures at the half maximum value either side of the $\Delta S(T)$ peak.

These values may be found indirectly through measurements of magnetisation and heat capacity under changing magnetic fields.

Firstly the magnetic entropy change may be found using Maxwell relations as

$$\Delta S = \int_{H_1}^{H_2} \left(\frac{\partial M}{\partial T}\right)_H \mathrm{d}H \tag{2.19}$$

where M is magnetisation, T is temperature, subscript H meaning at constant magnetic field, and H_1 and H_2 are the minimum and maximum applied fields. H_1 is commonly zero field.

For experimental magnetisation measurement, this is rendered into a more readily applicable form by McMichael, Ritter and Shull[21] as

$$\Delta S_M(T_{av}) = \frac{1}{\Delta T}\left[\int_0^H M(T+\Delta T,H)\,\mathrm{d}H - \int_0^H M(T,H)\,\mathrm{d}H\right] \tag{2.20}$$

for two magnetisation isotherms with average temperature T_{av}, separated by temperature difference ΔT.

This method requires integration of magnetisation curves as a function of field and for the application to real experimental data in the absence of a known equation $M(T,H)$ requires

some approximation or interpolation. In the absence of interpolation, a trapezoidal method for the calculation of the integrals may be used as proposed by Pecharsky and Gschneidner[22]:

$$\Delta S_M(T_{av})_{\Delta H} = \frac{\delta H}{2\delta T}\left(\delta M_1 + 2\sum_{k=2}^{n-1}\delta M_k + \delta M_n\right) \tag{2.21}$$

where δT is the temperature difference between the two isotherms, n is the number of points in field at which magnetisation M is measured, and $\delta H = \Delta H/(n-1)$ is the constant separation in field between these steps.

ΔS_M may then be calculated using this method or through fitting and numerical integration of $M(T,H)$ data. In either case the uncertainties arising from these integrations may be minimised by increasing the density of points taken in field (minimising δH).

Unlike ΔS_M, the adiabatic temperature change T_{ad} in a magnetocaloric process can not be determined from magnetisation measurements alone. This requires either measurements of heat capacity as a function of temperature and field, $C_p(T,H)$, or measurement heat capacity at zero field $C_p(T,0)$ combined with the magnetisation measurements described previously. Both again rely on the effective relation

$$S(T,H) = \int_0^T \frac{C(T,H)}{T}\,\mathrm{d}T + S_0 \tag{2.22}$$

where S_0 is the entropy at zero temperature which is usually assumed to be zero. By the calculation of total entropy from heat capacity data, both ΔS_M and T_{ad} may be determined from examination of $S(H,T)$, $S(0,T)$, $T(S,H)$ and $T(S,0)$ to determined the isotherms and adiabats in figure 2.4.

Chapter 3

Methods

The work presented here relied on a number of techniques which may be divided into those performed in the laboratory, principally measurements of magnetic susceptibility, and those reliant on large scale scattering facilities. The advantage of this approach lies in the distinct, complementary physical and material properties which may be explored through these different approaches.

3.1 SQUID Magnetometry

Magnetic measurements of samples were carried out using two Quantum Design Magnetic Property Measurements Systems (QD MPMS). One model MPMS3 (base temperature 1.8 K, maximum field 7 T) and one original MPMS (base temperature 2 K, maximum field 5 T). Both of these systems were used in the DC scan mode and results from both should be directly comparable. The pressure cell set-up detailed in 3.4.1 is compatible with both systems.

The foundation of this technique is the movement of a sample through the coils of one or more superconducting quantum interference devices (SQUID) and the measurement of the resultant induced voltage. A near-ideal voltage versus position response is shown in figure 3.1.

For most samples, a Levenberg-Marquadt least squares fit to the voltage-position data may be used to calculate the magnetic moment. This fit, as shown in equation 3.1, is used by the software supplied with the MPMS[23].

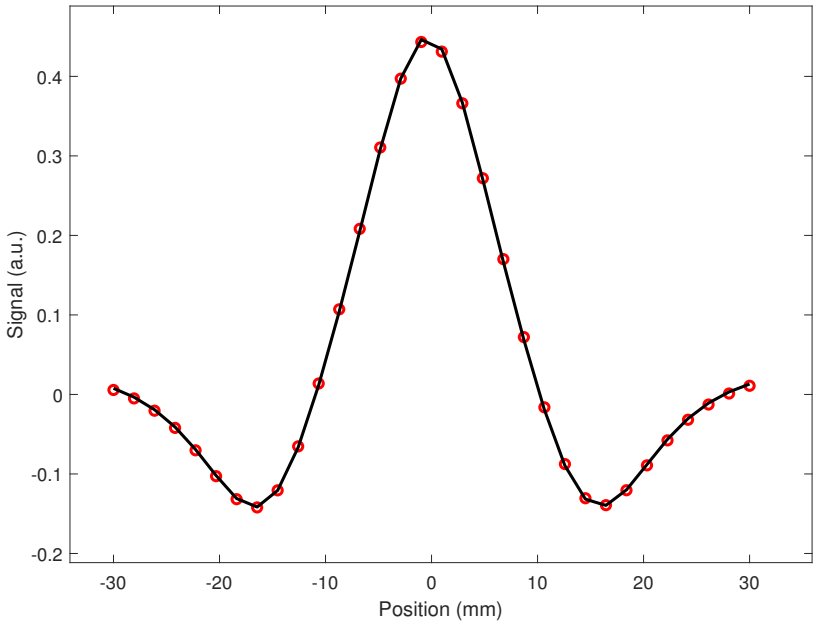

Fig. 3.1 Typical voltage versus position response (red) with Levenberg-Marquadt fit evaluated at each measured position (black).

$$V(Z) = X_1 + X_2 \cdot Z + X_3 \cdot \Big\{ 2\left[R^2 + (Z+X_4)^2\right]^{-\frac{3}{2}} - \left[R^2 + (\Lambda + (Z+X_4))^2\right]^{-\frac{3}{2}} - \left[R^2 + (-\Lambda + (Z+X_4))^2\right]^{-\frac{3}{2}} \Big\} \tag{3.1}$$

where Z is the sample position, $V(Z)$ is the induced voltage at that position, X_i are free parameters for fitting, and R and Λ are constants: longitudinal radius and longitudinal coil separation of the SQUID respectively.

In this fit X_3 is the final parameter of interest, corresponding to a voltage amplitude which is directly proportional to the measured magnetic moment by factors particular to the instrument used.

The voltage versus position data may also be fitted by the method of singular value decomposition (SVD). This is a linear algebraic technique which has previously seen use for the fitting of small magnetic signals[24].

SVD operates on the assumption that the raw measured voltage (arising from the desired signal and background) $V(z)$ may be treated as an superposition of multipole terms as

$$V(z) = \sum_{i=1}^{N} a_i f_i(z) \tag{3.2}$$

where $f_i(z)$ is the voltage signal arising at position z from the ith multipole term and a_i is the coefficient of that term. This may equally be expressed in the form

$$\mathbf{V} = F\mathbf{a} \tag{3.3}$$

where $\mathbf{V}$ is a matrix of length M being the number of data points in a scan, $\mathbf{a}$ is a matrix of length N being the maximum multipole term used and F is a $M \times N$ matrix of which the columns are the values of each multipole term.

The fit is determined by the minimization of the value:

$$r = |F\mathbf{a} - \mathbf{V}| \tag{3.4}$$

which may be solved through a least squares fitting method to give a solution

$$\mathbf{a}_{\text{fit}} = VS^{-1}U^T\mathbf{V} \tag{3.5}$$

where $USV^T = F$ is the singular value decomposition of F which may be found by standard matrix algebra.

When the size of the magnetic moment of the sample is similar to or smaller than that of the background from the sample environment, it is necessary to ensure that only contributions to the SQUID voltage from the sample are fitted. Indeed in extreme cases the raw signal may not be possible to fit with the standard methods. In these cases, post-processing of the raw data and background subtraction is required. This is particularly common when using SQUID pressure cells as in 3.4.1 due to their large mass compared to that of the sample.

The magnetic moment of the sample may be isolated by the repetition of a similar measurement (temperature, field, sample environment) without the sample present. The raw voltage-position data of this background measurement may then be subtracted from the first to recover the response due to the sample which is fit using the methods described previously. This method provides reliable isolation of the desired signal at the cost of the necessary repetition of experiments. For this to be optimally effective, conditions in the sample and background run must be matched as closely as possible. Using the SQUID pressure cell apparatus, this includes matching the effective length of the cell and position of the pistons by loading to matching pressures with only the manometer loaded.

It is accepted that repeated measurements will not perfectly reproduce the desired matching steps in both temperature and magnetic field. Using the systems described in this work,

use of the points matching most closely between the two runs in these two parameters is usually sufficient for effective background subtraction, though more advanced techniques involving the interpolation of scans in temperature and field are possible.

With the necessity of high-pressure apparatus used in this series of experiments, a software package was developed in MATLAB alongside collaborators to standardise both the magnetic background subtraction and fitting, to allow for easy comparison of results from LV and SVD fitting. An overview of this work may be found in reference [25].

3.2 Synchrotron X-ray Experiments

To determine of high-pressure crystal structures, x-ray diffraction measurements on the transition metal phosphorus sulphide $M\mathrm{PS_3}$ family of materials were carried out at the Diamond Light Source, Harwell on the beamlines I15 and I19. Experiments on both of these instruments utilised local diamond anvil cell equipment and procedure for high pressure study as detailed in 3.4.2.

3.2.1 Powder X-ray Diffraction (PXRD)

High pressure PXRD experiments on Fe, Ni and $\mathrm{MnPS_3}$ were carried out on I15, the dedicated extreme conditions beamline at the Diamond Light Source, Didcot, UK.

Powder samples of the $M\mathrm{PS_3}$ compounds were loaded by Dominik Daisenberger, instrument scientist on I15, into diamond anvil cells of culet diameter 400 µm. Pressure was applied via a gas loading membrane system. For comparison of hydrostaticity, measurements were taken both with a helium pressure medium loaded alongside the sample, and without medium, the pressure region being filled completely by the powder sample.

X-rays of wavelength $\lambda = 0.4246\,\text{Å}$ ($E = 29.2\,\text{keV}$) were used to collect diffraction patterns, this being a sufficient energy to pass through the diamond anvils used without significant attenuation. A 2D MAR345 detector was used with collection times varying between 15 s and 45 s.

Raw 2D detector intensity data was processed into a suitable *xy* format using DAWN software[26] with $\mathrm{LaB_6}$ calibration. Subsequent analysis of powder diffraction data was carried out using software packages GSAS-II[27] and Topas[28]. Initial solution of unknown high-pressure structures was approached using whole-pattern fitting methods Pawley refinement and Le Bail refinement. Accurate characterisation of the structures was then carried out by Rietveld refinement. Due to the nature of the experiments, additional parameters were

used in the refinements to account for the effects of pressure on the measured diffraction patterns.

The Rietveld refinement technique fits the measured powder diffraction pattern using both instrumental and sample characteristics as fitting parameters to minimise the function:

$$M = \sum \frac{1}{\sigma_i^2}(y_i - y_{ci})^2 \tag{3.6}$$

where σ_i is the variance of the observation y_i, y_i is the observed intensity at position i and y_{ci} is the calculated intensity at position i. The calculated intensity is determined by a number of contributing factors as

$$y_{ci} = y_{bi} + \sum_{n}^{\text{Phases}} S_n \sum_{k=k_1}^{k_2} j_{nk} \cdot L_{nk} \cdot O_{nk} \cdot |F_{nk}|^2 \cdot \Omega_{nk} \tag{3.7}$$

where y_{bi} is the background intensity at position i; S_n is the scale factor for phase n, proportional to its volume fraction; j_k is the multiplicity of the kth reflection; L is the Lorentz factor; O is a factor describing the effects of preferred orientations, or the departure from a purely random orientation distribution; $|F|$ is the structure factor; Ω is the peak profile function, approximating broadening effects from instrument and sample. The second summation runs over all reflections k_1 to k_2 contributing at position i[29]. Measured $M\text{PS}_3$ materials were assumed to be a single pure phase of the desired compound free from impurities.

Expected peak positions from the diamond anvils were calculated, and features at these positions excluded from analysis of the sample diffraction. These positions were calculated using the known incident wavelength and the cubic space-group of diamond in $Fd\bar{3}m$ with a lattice parameter $a = 3.566\,61$ Å. The unavoidable overlap of sample peaks with diamond peaks intrinsic to the experimental setup means that sample peaks falling at the same angle as those from diamond are unusable for, and excluded from, analysis.

Preferred orientations in the measured $M\text{PS}_3$ materials may affect the relative intensities of diffraction peaks such that they do not fit predictions based on the basic structure. Spherical harmonics were used as free parameters in the fits for the measured diffraction patterns to correct for this. This correction to the peak intensity is $A(h,y)$, given by

$$A(h,y) = 1 + \sum_{l=2}^{L} 4\pi/(2l+1) \sum_{m=-l}^{l} \sum_{n=-l}^{l} C_l^{mn} k_l^m(h) k_l^n(y) \tag{3.8}$$

where l is harmonic order up to the maximum used L. The harmonic terms $k_l^m(h)$ and $k_l^n(y)$ take values determined by the crystal and sample symmetry respectively and the coefficients C_l^{mn} are refined[30].

The magnitude of the texture is given by the texture index J[31]:

$$J = 1 + \sum_{l=2}^{L} 1/(2l+1) \sum_{m=-l}^{l} \sum_{n=-l}^{l} |C_l^{mn}|^2 . \tag{3.9}$$

J is equal to unity for a truly random material, increasing for textured samples, and becoming infinite for single-crystal data[32].

Strain in the measured material as is expected in high-pressure experiments also has the effect of changing the peak shapes seen in the diffraction pattern. The effects of strain include both peak broadening and asymmetry[33]. This is accounted for similarly in GSAS-II and Topaz. Peak broadening is also expected to be inversely proportional to crystallite size in the sample by the Scherrer equation:

$$\Delta(2\theta) = \frac{K\lambda}{\tau \cos\theta}. \tag{3.10}$$

where $\Delta(2\theta)$ is the line broadening at FWHM, K is a dimensionless shape factor with 0.9 being a good estimate in the absence of specific shape information, λ is the x-ray wavelength and τ is the mean crystallite size. This is most applicable to crystallite of size less than $\sim$0.2 µm.

Structureless solutions using the method of Pawley refinement are carried out in a similar fashion with the significant caveat that the intensity of the ith reflection is no longer determined by factors such as atomic species or position, but is instead a free parameter which may be varied. In this way, the relevant factors which are determined for the structure are the space group and unit cell dimensions. This may still be combined with other considerations such as spherical harmonics to account for preferred orientations to fit the observed pattern.

3.2.2 Single Crystal X-ray Diffraction

Complementary to PXRD, single crystal x-ray diffraction experiments were used to aid in structure determination of MPS$_3$ compounds. These experiments were performed at Diamond on the I19-2 "Small Molecule Single Crystal Diffraction" beamline. A similar pressure set-up as described for powder x-ray diffraction was used.

X-rays of wavelength 0.4589 Å ($E = 27$ keV) were used to collect the diffraction patterns with a Dectris area detector. Diffraction from the sample is easily separated from that arising from the gasket, due to the latter's amorphous nature giving rings of diffraction as opposed to

sharp spots. Scattering from the diamond anvils requires more consideration but is generally recognised by it being far more intense than the sample peaks due to the greater volume from which diffraction occurs.

Analysis of single crystal diffraction data was performed using Agilent CrysAlis Pro software with specifications provided by the I19 beamline scientists. Firstly the gasket rings were masked and excluded from peak searches. The UB orientation matrices for the two diamond anvils were obtained by searching found peaks for the known cubic cell of diamond which was assumed to be static with pressure. Peaks found to be corresponding to the diamonds were removed for the subsequent analysis. From the remaining peaks not attributed to the diamond or gasket rings, CrysAlis Pro was used to fit a unit cell and to integrate the diffraction patterns. Once a suitable unit cell was determined by fitting using Cryslalis Pro, the structure was refined to determine atomic positions using SHELX[34] within the WinGX package[35].

The opening angle of the diamond anvil cells used for this single crystal experiment was 28° which, depending on the orientation of the sample, further limited the accessible regions in reciprocal space in one direction. For the platelet crystals of the $M\mathrm{PS}_3$ compounds, the accessible region of reciprocal space is limited along the c^* direction. This limits the information from which relevant lattice parameters may be derived.

3.3 Neutron Scattering

Complementary to x-ray scattering methods, elastic neutron scattering was used to study the $M\mathrm{PS}_3$ materials. Neutron diffraction allows for the direct measurement of not only the atomic structure which can be examined with x-rays, but also the magnetic structure of systems containing non-zero magnetic moments. The main use of neutron scattering techniques for this work is this magnetic structure determination, as the greater intensity of x-ray scattering allows for more accurate and precise analysis of the underlying crystal structures.

3.3.1 Powder Neutron Diffraction

Powder neutron diffraction was used to study the high pressure magnetic structure of FePS_3. Experiments were carried out on the D20 beamline at the ILL, Grenoble.

Neutrons of wavelength 2.42 Å ($E = 13.97\,\mathrm{meV}$) were selected through a graphite monochromator.

The scattering of neutrons by a target within the Born approximation may be characterised by the differential cross-section for a neutron with incident wave vector $\mathbf{k}_i$ and spin σ_i and a final state with $\mathbf{k}_f$ and σ_f as follows:

$$\frac{\mathrm{d}\sigma}{\mathrm{d}\Omega}(\mathbf{k}_f\sigma_f,\mathbf{k}_i\sigma_i) = \left(\frac{m}{2\pi\hbar^2}\right)^2 \left|< \mathbf{k}_f\sigma_f|V(\mathbf{r})|\mathbf{k}_i\sigma_i >\right|^2 \tag{3.11}$$

where $V(r)$ is the potential experienced by a neutron at distance r from the scatterer and m is the neutron's mass. For elastic scattering wherein $\left|\mathbf{k}_f\right| = |\mathbf{k}_i|$ the scattering vector may be defined as $\mathbf{Q} = \mathbf{k}_i - \mathbf{k}_f$.

Due to the non-zero magnetic moment the neutron, scattering occurs by two separate mechanisms. Nucleon-nucleon scattering from sample nuclei is effectively isotropic due to the range of the relevant interaction being much shorter than the wavelength of thermal neutrons. Additional scattering arises from coupling of the neutron spin with magnetic fields arising from unpaired electrons in magnetic materials. For an incident beam of unpolarised neutrons, interference between nuclear and magnetic scattering does not occur, and the differential cross section may be simply broken up into nuclear and magnetic components as

$$\frac{\mathrm{d}\sigma}{\mathrm{d}\Omega}(\mathbf{Q}) = \frac{\mathrm{d}\sigma_N}{\mathrm{d}\Omega}(\mathbf{Q}) + \frac{\mathrm{d}\sigma_M}{\mathrm{d}\Omega}(\mathbf{Q}) \tag{3.12}$$

In an identical manner to powder x-ray diffraction methods, intensity is measured as a function of scattering angle 2θ from which scattering as a function of $Q = \frac{2\pi}{d}$ may be derived by Bragg's law.

$$n\lambda = 2d\sin\theta \tag{3.13}$$

where λ is the neutron wavelength used, d is the plane spacing.

The separation of magnetic scattering from that arising from the crystal structure may be achieved in a number of ways. Spin-polarised measurements may be performed which can differentiate between scattering from spin-flip and non-spin-flip processes. In the simpler case utilised here, this is achieved by measurements at temperatures above and below expected magnetic transitions. Peaks appearing only at temperatures below T_c can be attributed to magnetic effects as long as there is no simultaneous structural transition. Similarly, for a known crystal structure, Bragg peaks at d-spacing values corresponding to non-integer values of (hkl) are due to the magnetic ordering vector $\mathbf{k}_M$ in the absence of incommensurate crystal structures. Magnetic Bragg peaks may also appear at integer (hkl) values which are forbidden for the space group of the underlying crystal structure.

For the case of $\mathbf{k}_M = 0$ magnetic ordering, no additional peaks will be seen in the diffraction pattern, and increased intensity may be observed for existing peaks if $\mathbf{k}_M$ is equal

to an existing structural Bragg position. Such $\mathbf{k}_M = 0$ can correspond to a ferromagnetic structure, colinear antiferromagnetism or non-colinear structures depending on the underlying crystal space group. In this case it is only the intensities of the different magnetic peaks which can be used to distinguish between the possible magnetic configurations[36].

Where performed, structural solution and refinement is carried out in much the same way as for results of powder x-ray diffraction experiments.

3.4 High Pressure Methods

The methods used in this work to achieve high pressures can broadly be grouped into two categories: piston cylinder cells, and anvil cells. Within each of these classes, multiple designs of pressure cell may be used depending on the target pressure and the requirements of the measurement to be performed, being for example a low magnetic background or transparency to x-rays or neutrons.

3.4.1 SQUID Piston Cylinder Cell

For high-pressure SQUID magnetometry measurements, a miniature piston cylinder cell manufactured by CamCool was used. In this type of clamp cell, pressure is attained by the compression of a liquid pressure medium containing the sample and necessary wiring or manometer etc. This type of pressure cell has the advantage of a large sample volume compared to anvil-type cells (up to the order of 1–10 cm^3), with the drawback of a lower maximum pressure without making the cell apparatus prohibitively large. To allow for electrical measurement, such as four-point resistivity or capacitance measurements, wiring may be introduced to the pressure region through a feedthrough sealed with a rigid epoxy plug without compromising the attainable pressure in the cell, though for this study this type of cell was used only for contactless magnetisation measurements.

A disassembled cell is shown in figure 3.2. This 8.6 mm outer diameter of this cell is such that it can fit entirely within the SQUID coils in a commercial magnetometer, including those discussed in 3.1. To minimise the magnetic background from this cell inside the SQUID, the body is made from beryllium copper (BeCu). The combination of small diameter and the relatively soft alloy body limits the maximum pressure attainable in this cell to approximately 1.2 GPa, which is reached by an applied load of $\sim$6 kN.

The sample is loaded into a polytetrafluoroethylene (PTFE) cap of inner (outer) diameter 1.4 mm (2.5 mm) filled with a liquid pressure medium. Most commonly used in this study was Daphne 7373, a mixture of olefins commonly used in high pressure studies. Daphne 7373

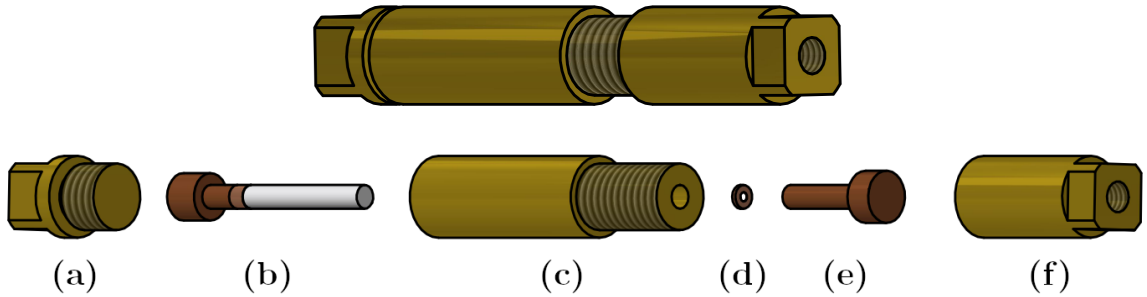

Fig. 3.2 CamCool manufactured SQUID piston cylinder cell. The outer diameter of the cell body is 8.6 mm, with the PTFE cap enclosing the sample space having an inner diameter of 1.4 mm. (Bottom) exploded view: (a) bottom lock nut, (b) bottom piston, copper ring, and PTFE cap assembly, (c) cell body, (d) anti-extrusion disk, (e) inner piston, (f) top lock nut.

solidifies at 2.2 GPa at room temperature[37] and exhibits almost no discontinuous pressure drop on solidification[38]. At pressures of up to 1 GPa, Daphne 7373 freezes at ∼200 K. The pressure loss on cooling from 300 K to 4.2 K using similar apparatus as described here has been measured to be 0.15–0.17 GPa irrespective of the initial pressure[38].

Prior to the loading of the measurement sample, a small sample of lead is loaded to function as a manometer. This lead is sized such that it does not block the PTFE cap, and the assumption is made that both the sample and the manometer are free to move under gravity inside the liquid medium, and lie in contact. Care must be taken when loading the manometer and sample that air bubbles are not trapped in the pressure medium, as this may cause the cap to fail under load due to uneven forces inside the pressure region. For the same reason the cap is filled with a slight excess of pressure medium such that air is not trapped inside when the cell is assembled in the next step.

With the sample and manometer submerged in the pressure medium inside the PTFE cap, the lower piston is inserted into the open end of the cap, with the copper ring around the piston. This copper ring is soft and is designed to deform first to seal the pressure medium and prevent the extrusion of the PTFE cap under load. This assembly is inserted into the cell body and pushed into position under a loading force of 2 kN to overcome friction between the cap and the cell bore and to ensure it is firmly in contact with the cell body. The bottom lock nut is then screwed in by hand, and gently tightened using a small spanner. At the blank end of the PTFE cap, accessed through the other end of the cell body, the anti-extrusion disk is inserted into the cell bore for the same reason as the copper ring around the lower piston. The inner piston follows this around which the top lock nut is screwed on. The loading force is applied using a hydraulic press, through the external piston pushing on the inner piston. Once the desired loading force is applied, the pressure is locked in place by tightening the

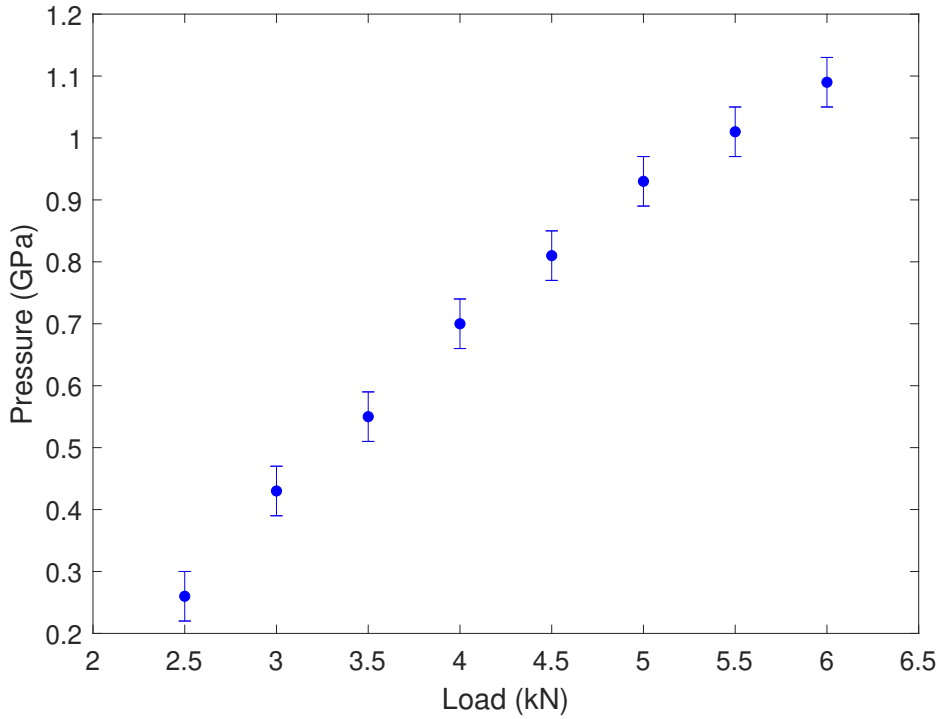

Fig. 3.3 Pressure inside the sample space of the SQUID piston cylinder cell, determined from lead mangetisation measurement and equation 3.14, against applied cell load. The uncertainty is dominated by the intrinsic width in temperatures of the superconducting transition.

top lock nut against the inner piston. An experimentally determined pressure-load relation and pressure cell length relation are shown in figure 3.3.

Sample alignment may be roughly controlled through the relative dimensions to which it is cut relative to the the known crystallographic orientation. Ideal samples are cut in a needle geometry such that possible rotation about the short axes is limited by the inner diameter of the PTFE cap. This sample geometry simultaneously helps to minimise the demagnetising field generated.

Pressure is determined from the lead manometer by the measurement of its superconducting transition temperature, T_c according to reference [39] by:

$$T_c(P) = T_c(0) - (0.365 \pm 0.003)P \tag{3.14}$$

where T_c is measured in K and P in GPa. This relation holds for pressures up to 5 GPa, well above the maximum pressure attainable in this cell.

Uncertainty in the measured pressure arises from uncertainty in the measured superconducting transition temperature. In contactless magnetisation measurements, this is dominated by the intrinsic width of the superconducting transition rather than uncertainty in the temper-

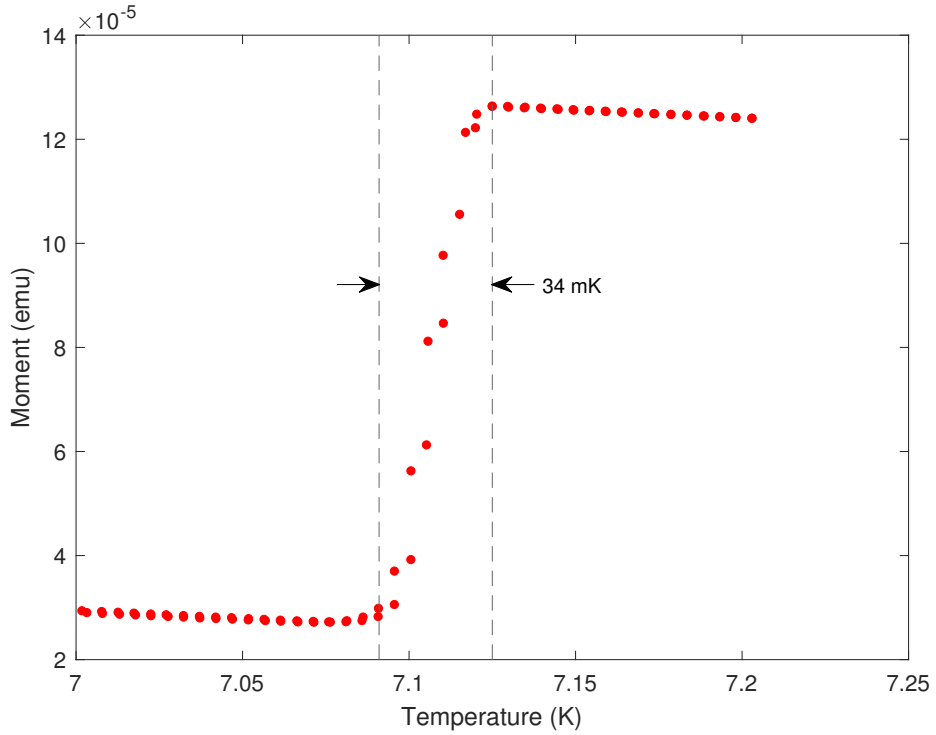

Fig. 3.4 Magnetisation measurement of the superconducting transition of lead in SQUID pressure cell loaded with 2.5 kN force corresponding to a pressure of 0.26(4) GPa.

ature measurement in the systems used. An example magnetisation measurement of the lead superconducting transition is shown in figure 3.4.

3.4.2 Diamond Anvil Cell

For pressures above those achievable with piston cylinder type pressure cells, diamond anvil cells (DAC) may be used to perform similar experiments. Wired measurements of resistivity or AC susceptibility are achievable but for the results presented here the use of DACs is limited to contactless measurements by x-ray and neutron methods.

The pressure region in these cells is enclosed by the culets of the diamonds and the metallic gasket through which a hole of diameter less than half that of the culets has been drilled (the culets are only approximately circular and thus the diameter is an average). The volume of this pressure region is as a result orders of magnitude reduced compared to PCCs. A liquid pressure medium may be used to maintain hydrostaticity up to pressures on the order of 10 GPa.

Pressure determination inside DACs was achieved using two methods. For x-ray experiments, spheres of ruby smaller than the sample ($\sim$10 µm diameter) were inserted in the

pressure region. Before and after sample measurements were performed at each pressure point, the fluorescence spectrum of the ruby was measured using an exciting laser and a spectrometer. The wavelength of the R1 fluorescence line (649.3 nm at ambient pressure) shifts to higher values with increasing pressure according to equation 3.15 which may be used to infer the pressure in the DAC[40].

$$P = \frac{A}{B}\left\{\left[1+\frac{\Delta\lambda}{\lambda_0}\right]^B - 1\right\} \tag{3.15}$$

where P is pressure in Mbar, $A = 19.04\,\text{Mbar}$, $B = 7.665$ and $\Delta\lambda/\lambda_0$ is the fractional change in wavelength of the R1 line.

Experiments at the Diamond Light Source used diamond anvils of culet size 400 µm and a rhenium gasket. The first experiment on the D20 beamline at the ILL utilised a Paris-Edinburgh type pressure cell with boron nitride (BN) anvils and used a sample of lead in the sample space for pressure determination via its known equation of state. However, to achieve the required pressures for this study in a large enough sample volume for neutron diffraction measurements, the use of a double-toroidal diamond anvil cell was necessary. This cell was provided thanks to the collaboration of Dr Stefan Klotz, Sorbonne University. By modifying the geometry of the anvils, double-toroidal cells are able to achieve higher pressures using a Paris-Edinburgh press not possible with a single-toiroidal or flat anvil shape. Such double-toroidal cells have been proposed and utilised in a number of neutron scattering experiments[41, 42, 43].

By comparison to simpler anvil cell designs, the sample volume of the double-toroidal cell is reduced by half or more to a value of $\sim$30 mm^3[44]. Loading force of up to 200 t equivalent may be applied to achieve pressures reaching 25 GPa. Sintered diamond anvils are used, chosen over tungsten carbide for its higher neutron transparency, which is made more necessary by the limited sample volume.

The powdered sample was loaded in a tin-zirconium spherical encapsulating gasket as shown in the lower diagram in figure 3.5. A 4:1 methanol:ethanol mixture by volume was used to wet the powder and act as a hydrostatic pressure medium. A detailed overview of the design and use of the double-toroidal cell may be found in reference [44].

The use of encapsulating gaskets as shown in the lower of figure 3.5 is advantageous for the improvement in hydrostaticity over a standard setup in which the fluid sample volume is in contact with the anvils themselves[45]. Such encapsulation of a fluid-like sample is also seen to reduce the occurrence of failure of the anvils at high pressures, the risk of which is higher when samples undergo structural phase transitions under pressure which result in

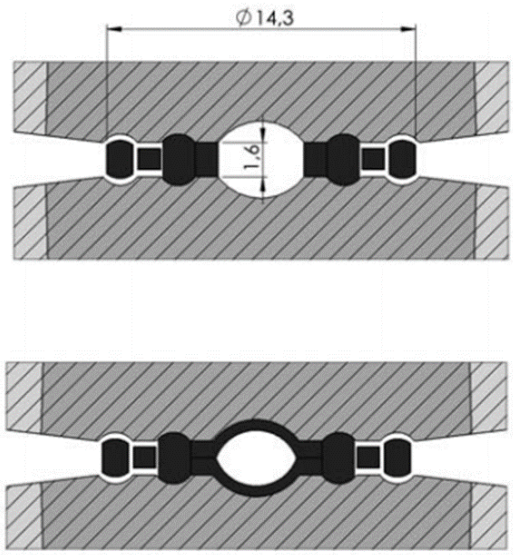

Fig. 3.5 Schematic design of the double-toroidal diamond anvils used with Paris-Edinburgh cells for the high pressure neutron diffraction experiment on D20 with a standard (upper) and encapsulating (lower) gasket. The thickness of the gasket is chosen such that on initial loading, contact is made only between the anvils and the regions of the gasket out to the inner toroid. For this work an encapsulating gasket was used. Taken from reference [44].

changes of the sample volume as is the case for certain high pressure transitions in the $M\mathrm{PS}_3$ family.

To avoid the observance of peaks from common manometers in the region of interest, pressure in the double-toroidal cell was determined by the structural peaks of the FePS_3 sample itself and comparison to previous data from synchrotron x-ray experiments. At pressures of up to 14 GPa where FePS_3 goes through its second high pressure structural transition, the measured d-spacing of the (001) peak gives good pressure information. Above this, in the HP-II phase, the position of the (131) peak becomes more sensitive to pressure and was used for pressure determination.

Chapter 4

MPS$_3$ Compounds

4.1 Overview of Previous Work

Layered materials which behave as effectively two-dimensional magnets have attracted a great deal of recent interest for both the fundamental understanding of their magnetism as well as potential future applications in new devices. Such materials which natively possess a layered magnetic structure in combination with correlated electrons provide a huge space for experimentation, free from many of the complexities in similar systems such as magnetically doped transition-metal dichalcogenides. The family of transition metal phosphorus sulphide compounds MPS$_3$ (M = Fe, Ni, Mn) offer an ideal space in which to explore the magnetic, electric and structural behaviours of this class of materials which may be readily tuned by pressure to change the dimensionality of the structures.

A number of previous studies of these compounds have explored how the magnetic and electrical properties of these materials may be affected by tuning the lattice towards either of two extremes: the application of pressure to decrease separation between the planes and hence drive system towards three-dimensionality, or delamination towards a single monolayer to study behaviour in the extreme two-dimensional limit. These contrasting approaches have revealed a range of behaviours not seen in any of the pristine compounds.

FePS$_3$, NiPS$_3$ and MnPS$_3$ all share a monoclinic space group $C2/m$ under ambient conditions, with transition metal ions lying in a honeycomb lattice in the ab planes which are weakly coupled by van der Waals forces[46]. Lattice parameters are given in table 4.1 and the structure of FePS$_3$ which is archetypal of the family is shown in figure 4.2.

	a (Å)	b (Å)	c (Å)	β	V (Å^3)
FePS$_3$	5.947(1)	10.300(1)	6.7222(8)	107.16(1)°	393.2(3)
NiPS$_3$	5.812(2)	10.070(3)	6.632(1)	106.98(3)°	371.2(4)
MnPS$_3$	6.077(1)	10.524(3)	6.796(1)	107.35(2)°	414.7(5)

Table 4.1 Ambient condition lattice parameters for the $C2/m$ MPS$_3$ materials from reference [46].

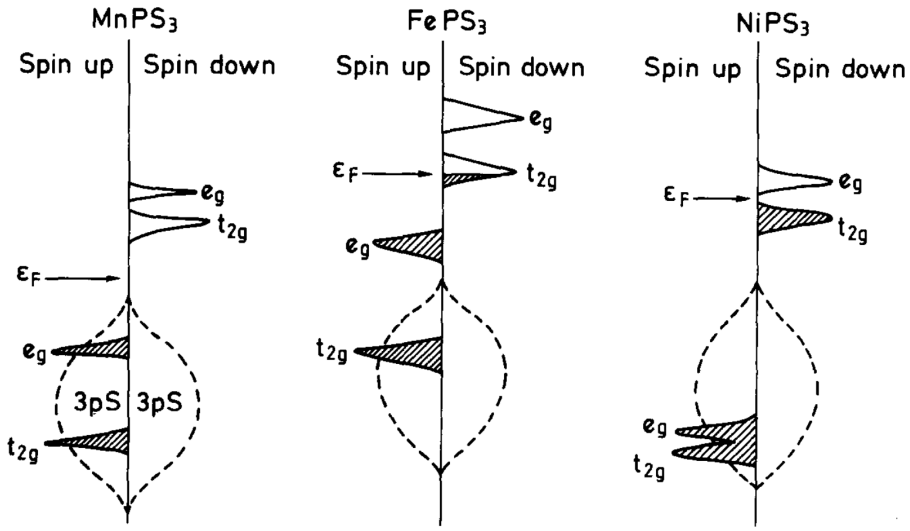

Fig. 4.1 Calculated band structures for MPS$_3$ compounds from reference [47]. Note that this predicts a half-filled band and so metallic behaviour in FePS$_3$ which is not observed in experiment.

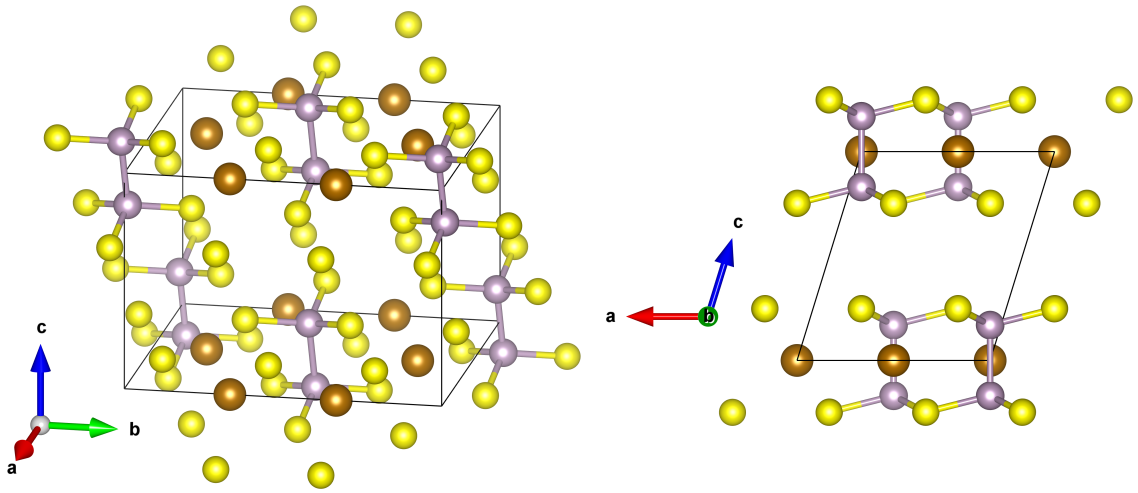

Fig. 4.2 Crystal structure of $FePS_3$ showing Fe ions in brown, P ions in grey and S ions in yellow. The structure is similar in other members of the family in the form of transition metal ions and P_2S_6 clusters separated by a van der Waals gap. The lattice parameters and precise value of the angle β near 107° vary between the compounds. Made using VESTA software[48].

J_1 (meV)	J_2 (meV)	J_3 (meV)	J' (meV)
1.46(1)	−0.04(4)	−0.96(5)	−0.0073(3)

Table 4.2 Magnetic exchange parameter values for $FePS_3$[51]. $J_{1,2,3}$ are nearest, next-nearest and next-next-nearest neighbours within the metal ion planes, and J' nearest inter-planar neighbour interaction.

$FePS_3$

$FePS_3$ is an antiferromagnet with a Néel temperature of 123 K[49]. Below this temperature the $S = 2$ moments of the Fe^{2+} ions are oriented along the c^* direction, being normal to the *ab* planes. The effective moment of the spins is $\mu_{eff} = 4.94\mu_B$[50]. The magnetic structure of this compound has been the subject of controversy, but the latest work concludes the it possesses a magnetic propagation vector of $\mathbf{k}_M = [01\frac{1}{2}]$[51]. This corresponds to ferromagnetic zig-zag chains along the *a* direction, antiferromagnetically coupled to their neighbours in the *ab* plane and also coupled antiferromagnetically along the *c* direction. This structure is shown in figure 4.3 and calculated exchange parameters are given in table 4.2 and shown in figure 4.4. Previously proposed[52, 53] was a structure with $\mathbf{k}_M = [\frac{1}{2}\frac{1}{2}l]$, $l \approx 0.34$, with the ferromagnetic chains being rotated by 120° in the *ab* plane and incomplete, short range order between the planes.

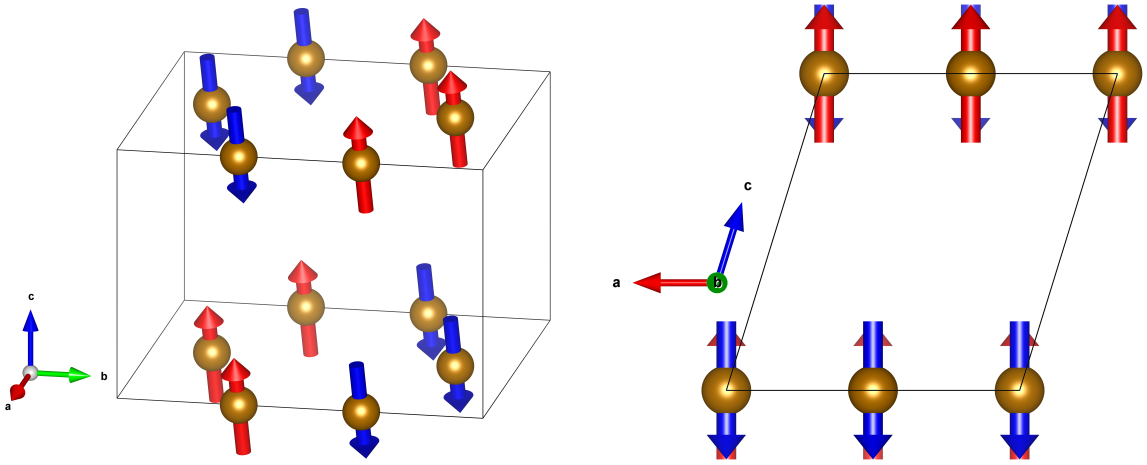

Fig. 4.3 Magnetic structure of $FePS_3$ showing Fe ions only for clarity. The two differing orientations of magnetic moments are shown in distinct colours, pointing normal to the *ab* planes, along c^*. Made using VESTA software[48].

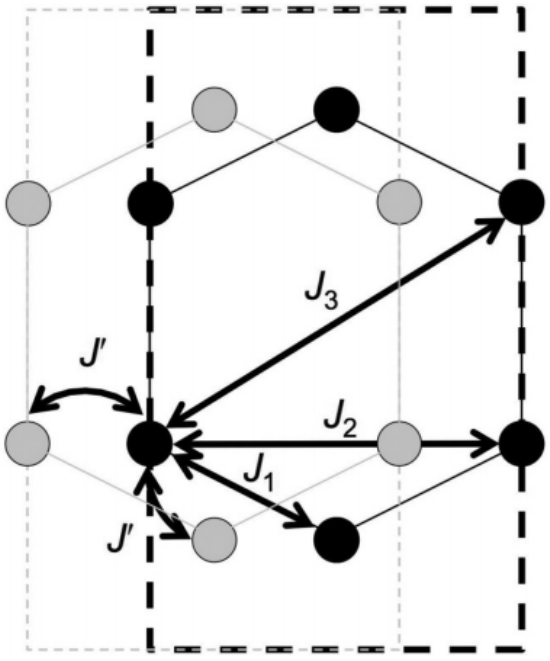

Fig. 4.4 Schematic representation of the four relevant magnetic exchange parameters in table 4.2. The planes are shown with the c^* direction normal to the page, with Fe^{2+} planes separated by one lattice unit along the c direction shown by the light and dark shading. Taken from reference [51].

With the feasibility of delaminating $FePS_3$ down to a single monolayer, recent work[54] has used Raman scattering to examine its magnetic behaviour down to the two-dimensional limit. $FePS_3$ largely retains its bulk magnetic properties, exhibiting an Ising-type antiferromagnetic order in the monolayer limit. Its transition temperature is also largely independent of thickness, with a thin-limit $T_N \sim 118\,\mathrm{K}$ indicating that the extremely weak inter-layer interactions have little effect on the antiferromagnetic order.

Other studies using a similar method however report a reduction in T_N to 104 K in monolayer samples compared to bulk, with a strong dependence on the number of layers[55]. The persistence of magnetism down to the monolayer limit is however consistent. Increasing the relative size of the inter-planar coupling J', for example through reduction of the inter-planar spacing is likely to have a very different effect on the overall magnetic structure through encouraging a more three-dimensional nature than the pristine or monolayer examples.

The magnetic transition is first order, and in the bulk material coincides with a discontinuous change in the lattice parameters[56, 57, 58]. Temperature dependent neutron diffraction measurements follow predictions for a two-dimensional Ising model on a honeycomb lattice[53]. Deviations from Ising behaviour are seen however: for example inelastic neutron scattering experiments show dispersive magnons in the ordered phase[51].

Disagreement over the magnetic ordering vector in $FePS_3$ has arisen largely due to the tendency of the material towards stacking faults giving rotational twinning with a common axis along the c^* direction. These twins, arising from a 120° rotation about c^*, give the appearance of a pseudo-three-fold symmetry which may be observed in, for example, electron diffraction patterns[56].

Recent magnetisation measurements in magnetic fields up to 65 T by Wildes et al.[59] confirm the occurrence of two first-order magnetic phase transitions above 35 T at 4 K when the field is applied parallel to the magnetic moment direction which indicate a significant magnetoelastic coupling. With the application of field along the b direction (normal to the moment direction), signifiant magnetostriction is observed at high applied fields, to the extent that the bulk sample will effectively undergo induced delamination. The requisite strain induced in the sample may well additionally induce new crystal structures.

Previous work in Quantum Matter Group, Cavendish Laboratory, has shown that $FePS_3$ undergoes two structural transitions under pressure[60]. The first transition at 4 GPa does not result in a change of space group, retaining the ambient $C2/m$, but with a decrease in the angle β from 107.34(2)° to 89.33(2)°, representing a shear along the a axis of $\sim \frac{a}{3}$. This results in a small reduction of the volume of the unit cell and an alteration of the stacking along c^* such that metal ions and ligands lie directly above others in adjacent planes. This phase is denoted HP-I.

a (Å)	b (Å)	c (Å)	β	V (Å^3)
5.7620(12)	9.988(2)	5.803(5)	89.33(2)°	333.3(3)

Table 4.3 Cell parameters (space group $C2/m$) for $FePS_3$ HP-I at 10.1 GPa from reference [60].

a (Å)	c (Å)	V (Å^3)
5.699(4)	4.818(3)	135.54(19)

Table 4.4 Cell parameters (space group $P\bar{3}1m$) for $FePS_3$ HP-II at 18.1 GPa from reference [60].

The second transition, at a pressure of 14 GPa, is an increase in symmetry from the second $C2/m$ structure to a trigonal hexagonal space group $P\bar{3}1m$, denoted HP-II. This transition involves a dramatic collapse of the spacing between the van der Waals planes of $\sim$20 %. Structural parameters for these high pressure phases are given in tables 4.3 and 4.4 respectively.

These proposed high pressure structures are supported by recent ab initio calculations[61]. Zheng et al. predict two similar transitions as observed by Haines et al. using a density functional theory (DFT) method. With the reduction of inter-layer separation in the HP-II $P\bar{3}1m$ phase, inter-layer P-P bonds are also predicted to form. In the insulating intermediate pressure phase, the calculated electronic band-gap is reduced to 1.00 eV from the 1.31 eV calculated at ambient pressure. In both structures the bottom of the conduction band is largely composed of Fe 3d and S 3p orbitals, with the top of the valence band being derived from Fe 3d orbitals.

Such calculations also suggest a spin-crossover from $S = 2$ to $S = 0$ coinciding with the higher pressure transition, similar to that which is reported by Wang et al. from x-ray emission spectroscopy measurements. This is explained by the observation that the effect of external pressure on Hund's intra-atomic exchange energy J is minimal, but it acts to increase the crystal field splitting Δ. With increasing pressure $\Delta > J$ and so the high spin state transforms to the low spin state. Also calculated are corresponding electronic band structures for the higher pressure phases, which fit with the observed insulator-to-metal transition in the material. These are shown in figure 4.5.

The transition of $FePS_3$ to HP-II approximately coincides with pressure-induced metallisation of the material. At ambient conditions, $FePS_3$ is a p-type semiconductor with an indirect band gap of $\sim$1.5 eV [50, 62]. A calculated band structure is shown in figure 4.1

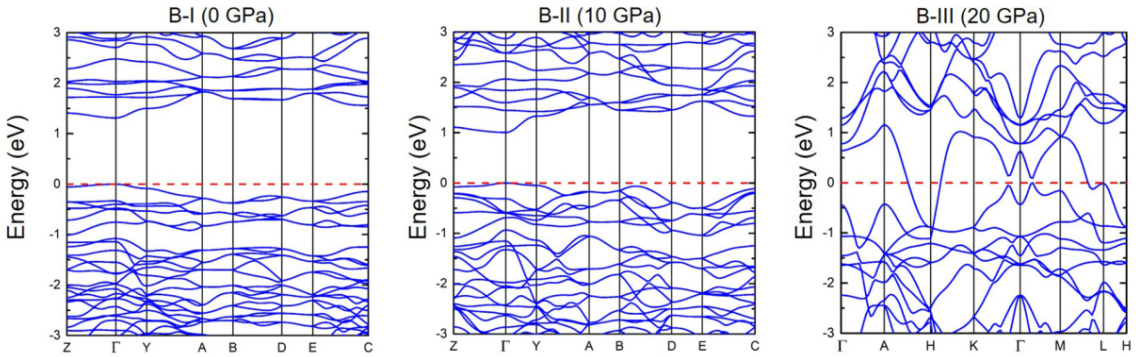

Fig. 4.5 Calculated band structures of $FePS_3$ at ambient pressure and in the two higher pressure structures from reference [61]. The overlap of valence and conduction bands in the highest pressure B-III phase suggest an insulator-to-metal transition accompanying this structural transition.

from reference [47]. This work finds the highest energy (fully) occupied band to be the S-3p $e_g(\uparrow)$ band and the lowest unoccupied band to be the $t_{2g}(\downarrow)$. This suggest splitting of the t_{2g} band through the mechanism for a Mott insulator giving rise to the insulating behaviour and the observed band gap. Pressures below the HP-II transition are seen to decrease the resistivity, and above 5 GPa a change in the temperature dependence from an Arrhenius type conduction process to a resistivity which decreases with decreasing temperature is reported, indicating metallic type behaviour. Measurements demonstrating this are shown in figure 4.6.

The metallic type relation between resistivity and temperature in the HP-II phase is an incomplete description due to a measured upturn in ρ below $\sim$50 K. Such an upturn is also measured in the related compound $V_{0.9}PS_3$[63]. These upturns are described as Kondo-like but do not properly fit the expected logarithmic dependence for such behaviour and remain to be comprehensively explained. Furthermore, the temperature dependence of the resistance above the low-temperature upturn is sub-linear, perhaps suggesting non-Fermi-liquid behaviour in the HP-II metallic phase. The phase shows a significant positive magnetoresistance, up to $\sim$4.6 % at 5 T.

The HP-II transition with pressure in $FePS_3$ is similar to that observed in the related compound $CdPS_3$ in temperature[64, 65]. In this system, a monoclinic $C2/m$ to trigonal $R3$ transition is observed from x-ray diffraction at a temperature of $\sim$228 K. This transition reaffirms the first-order character of the transition by the lack of any sub-group to group relation between the two space groups. In further similarity to the $FePS_3$ case, a 17° reduction of the monoclinic β angle is observed at the transition giving a change in the layer stacking, with the difference that in $CdPS_3$ this coincides with the collapse in the c lattice parameter.

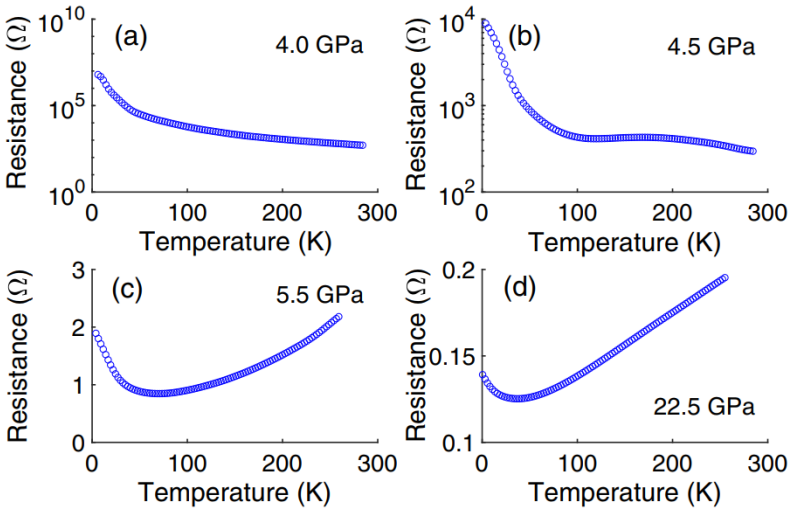

Fig. 4.6 Measured resistance against temperature with increasing pressure from reference [60]. Note the differing orders of magnitude of the ordinate. A crossover to resistivity decreasing with decreasing temperature is observed above 5 GPa.

An open question in relation to these high-pressure structural transitions is their effect on the magnetic structure. As discussed, the collapse of the inter-planar separation reduces not only the distance between Fe^{2+} ions in neighbouring layers, but also the stacking and the arrangement of the ligand ions which will impact magnetic superexchange. With J' being close to zero, the effect of the structural change may be sufficient to induce a switch to a ferromagnetic coupling between planes, or the changing environment of the Fe^{2+} ions may be a dominant effect which could result in no net magnetic moment.

The selenium analogue of this material, $FePSe_3$, which shares the $C2/m$ space group, has been seen to enter a superconducting phase at a critical pressure $P_c \approx 9.0$ GPa with an initial $T_c \approx 2.5$ K[66]. A maximum T_c of $\sim$5.5 K is reached at 26.9 GPa, and superconductivity persists up to at least 40 GPa. This materials also undergoes a similar c^* axis and volume collapse to the sulphur compound which also results in initial metallisation at the lower pressure of 8 GPa[61]. The same study reports from x-ray emission spectroscopy measurements that both the sulphur and selenium systems undergo a spin-crossover from an $S = 2$ to $S = 0$ state which coincides with the c-axis collapse and the superconductivity or metallisation. This crossover should be apparent in any neutron diffraction studies above the necessary pressures.

The observation of superconductivity in $FePSe_3$ and the similarity of the structural transitions and metallisation suggests that at higher pressures than those measured to date, $FePS_3$ may also show emergent superconductivity at low temperatures. The confirmation or denial of this state in $FePS_3$ would allow for better exploration of the nature of emergent supercon-

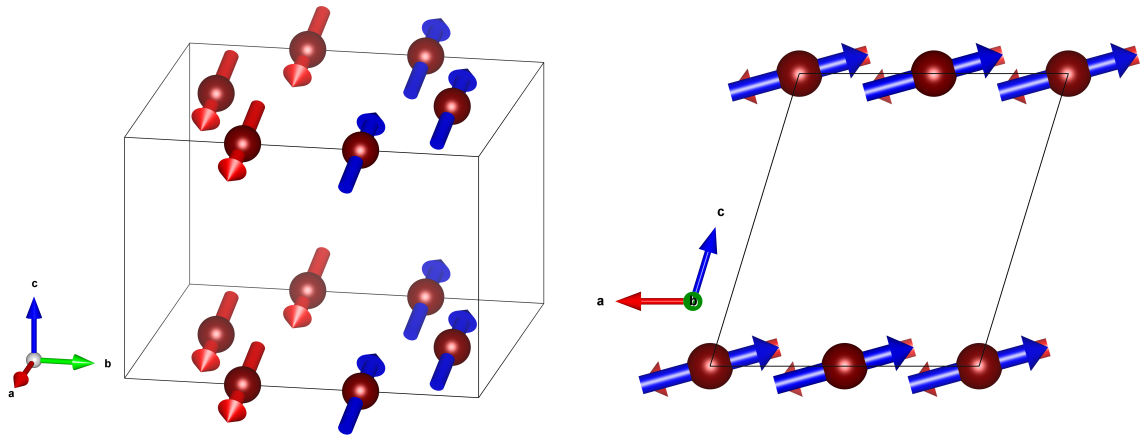

Fig. 4.7 Magnetic structure of $NiPS_3$ showing Ni ions only for clarity. The two differing orientations of magnetic moments are shown in distinct colours. Made using VESTA software[48].

ductivity in this type of system, which should have strong similarities to other unconventional superconductors such as cuprate high T_c materials and heavy fermion superconductors.

$NiPS_3$

$NiPS_3$ is another antiferromagnetic material with Ni^{2+} ions of spin $S = 1$ and a Néel temperature $T_N = 155\,\mathrm{K}$[67, 68]. Much like $FePS_3$, different magnetic structures have been proposed for the nickel compound, with scattering experimental results susceptible to preferred orientations and amorphization of powder samples due to grinding. The magnetic properties of the amorphous compound are however distinct from the crystalline form of interest here[69].

$NiPS_3$ possesses a magnetic propagation vector $\mathbf{k}_M = [010]$[70, 68] and a structure of ferromagnetic chains along the a direction coupled antiferromagnetically to their neighbours in plane, and ferromagnetically to adjacent planes. Moments point mostly along the a direction, with a small component along c[70]. This is shown in figure 4.7. The structure is best described with a Heisenberg Hamiltonian with an in-plane anisotropy. Recent calculated values for the exchange parameters in $NiPS_3$ are given in table 4.5 as measured by Lançon et al. With the honeycomb structure of $NiPS_3$ having three first, six second and three third nearest neighbours, the weighted sum of these parameters is $-5.2\,\mathrm{meV}$, which is in near agreement with the $-5\,\mathrm{meV}$ found from susceptibility measurements by Chandrasekharan and Vasudevan[67].

Anisotropy in the system is an important factor for its magnetic behaviour. The antiferromagnetic phase cannot be well fit across the entire temperature range by a single value of

J_1 (meV)	J_2 (meV)	J_3 (meV)	J' (meV)
1.9(1)	−0.1(1)	−6.90(5)	—

Table 4.5 Magnetic exchange parameter values for $NiPS_3$[71].

the critical exponent β, which at lower temperatures is low enough to be consistent with its two-dimensional magnetic nature. It does not however correspond to expected values from either Ising or XY models, the reason for which remains uncertain. Higher in temperature in the magnetic phase at $T \simeq 0.9T_N$, fitting of the intensity of the primary magnetic peak in neutron diffraction data indicates an increase in the critical exponent β to 0.3 which is more characteristic of a three-dimensional antiferromagnetic structure. Such a crossover is seemingly consistent with the emergence of three-dimensional interactions in lower dimensional XY materials[72].

As the band structure in figure 4.1 shows, $NiPS_3$ is a p-type semiconductor. The indirect band gap is 1.6 eV[73] as determined from Raman spectroscopy and consequently the room temperature resistivity are higher than that in $FePS_3$ but lower than those measured for $MnPS_3$. Calculation of the band structure has been performed [74, 75, 47]. Field-effect transistors fabricated using $NiPS_3$ show n-type semiconducting behaviour[76]. Hole doping the material at the level of 0.1 hole per atom induces a metallic state for the spin-up configuration and semiconducting for spin-down with an indirect band gap of 0.47 eV. Similarly, electron doping at the same level causes a metallic spin-down configuration, with an indirect band gap of 1.53 eV for the spin-up configuration.

In a similar manner as has been carried out on $FePS_3$, the behaviour of $NiPS_3$ as it is mechanically exfoliated down to a single monolayer has been explored.[77]. Observed Raman spectra of thin layers depend strongly on the number of layers in the sample and differ significantly from results of the bulk compound, displaying distinct features arising from two-phonon processes.

The effect of pressure on the transport properties of $NiPS_3$ has been studied up to pressures of up to the order of 20 GPa[78, 79]. The clear effect of pressure on room-temperature resistivity is shown in figure 4.8. Between ambient pressure and 20 GPa, a suppression of the measured resistance of five orders of magnitude is observed. However at lower pressures up to ∼4 GPa, the resistivity is initially seen to increase by a factor of ten. Whilst uncertainty exists in the resistance of the electrical contacts in this experimental set up, this feature may be a result of a changing spin state in the material which may be investigated by high pressure neutron diffraction experiments. At 22.5 GPa, $NiPS_3$ remains semiconducting, but with a much reduced bandgap of ∼25 meV. Whilst metallisation is not observed, the general trend

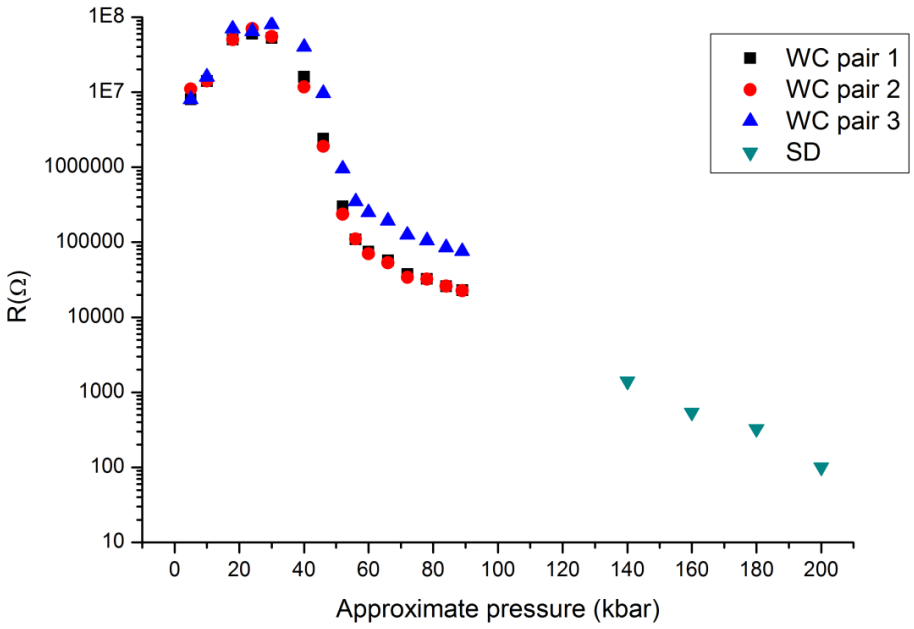

Fig. 4.8 Room temperature resistivity of $NiPS_3$ as a function of pressure. Point shape and colour indicates the anvil material of the pressure cell: WC - tungsten carbide and SD - sintered diamond. Between ambient pressure and 20 GPa an overall suppression of five orders of magnitude is observed, with resistivity increasing at lower pressures in a different manner from the general trend. Taken from reference [79].

is similar to that observed in $FePS_3$ which suggests that metallisation will be achieved at higher pressures which remain to be experimentally measured.

$MnPS_3$

$MnPS_3$ is a $\mathbf{k}_M = 0$ antiferromagnet below a Néel temperature $T_N = 78\,\mathrm{K}$[80]. The spin $\frac{5}{2}$ Mn^{2+} ions are coupled antiferromagnetically to their nearest neighbours in the *ab* plane, and ferromagnetically to adjacent planes. Moments lie almost normal to the *ab* planes, but at an angle $\sim 8°$ to the c^* direction in the c^*a plane. This structure is shown in figure 4.9. This structure sets $MnPS_3$ apart from both the iron and nickel compounds, in that it does not possess zig-zag ferromagnetic chains along the *a* direction.

The observed tilt of the magnetic moments with respect to the crystallographic axes is attributed to anisotropies, further evidence for which is seen in the gapped spin-wave dispersion curves[81]. At the Brillouin zone centre, this gap is measured to be $0.499(3)$ meV[82]. This anisotropy results in critical behaviour in the system being better described by a 2D XY Hamiltonian than a Heisenberg one, which fits well to other properties and is commonly used to describe the system[83]. Magnetic exchange constants are shown in table 4.6, where J_1,

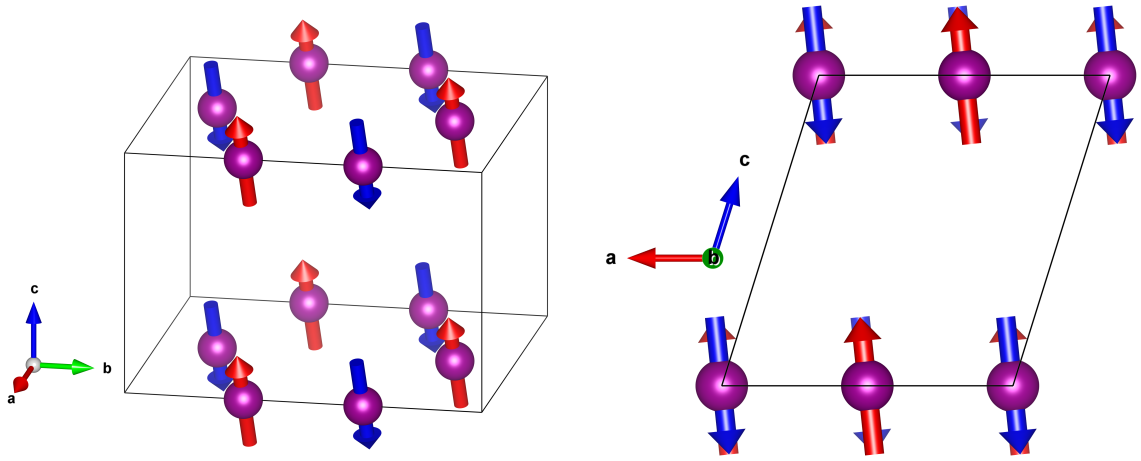

Fig. 4.9 Magnetic structure of $MnPS_3$ showing Mn ions only for clarity. The two differing orientations of magnetic moments are shown in distinct colours. Made using VESTA software[48].

J_1 (meV)	J_2 (meV)	J_3 (meV)	J' (meV)
$-0.77(9)$	$-0.07(7)$	$-0.18(1)$	$0.0019(2)$

Table 4.6 Magnetic exchange parameter values for $MnPS_3$[82].

J_2 and J_3 are the exchange integrals for first, second and third-nearest in-plane neighbours respectively and J' is the inter-plane exchange.

Just below T_N, changes in the critical exponent β indicate a crossover from two to three-dimensional critical behaviour. Wildes et al.[81] suggest that $MnPS_3$ falls between the considered models, due to the similar calculated magnitudes of the inter-plane exchange and the weak anisotropy.

$MnPS_3$ behaves as a p-type semiconductor with a room-temperature resistivity of $\sim 1 \times 10^{12}\,\Omega$cm [84]. Its band gap is the highest of the three compounds at 3.0 eV [85, 86]. Similar to the other compounds, resistivity drops with increasing pressure, and a semiconductor-to-metal transition is reported to coincide with a volume collapse of the crystal structure[87].

The structural and electronic transitions in $MnPS_3$ are accompanied by a spin-crossover (SCO) as reported by x-ray emission spectra results[55]. The ambient Mn^{2+} $S = 5/2$ state drops abruptly to $S = 1/2$. As for $FePS_3$, this reported spin crossover remains to be directly explored through techniques such as neutron scattering.

Complexities are observed in the magnetic state in Raman scattering spectra[88]. Firstly coinciding with the transition to the antiferromagnetic state, there is a strong shift of mode

frequencies which indicates strong coupling between phonon and magnon dynamics. Furthermore at low temperatures, the Raman spectra show feature which are attributed to two-magnon scattering as well as additional magnon-phonon interaction.

As other materials, $MnPS_3$ finds application in the field of non-linear optics in ultra-fast laser generation, giving good encouragement that other related MPX_3 compounds may find similar application in this capacity.

4.1.1 Aims

This work will focus on two key questions in this family of materials which pose experimental difficulties. Firstly, both DFT calculations and indirect x-ray emission spectroscopy measurements predict that the previously observed metallic phase of $FePS_3$ should be non-magnetic following a $S = 2$ to $S = 0$ spin crossover coinciding with the c-axis collapse. This will be examined directly for the first time using high-pressure powder neutron diffraction methods to track the evolution of the magnetic order in $FePS_3$ through both of its structural transitions. Further study of the high-pressure crystal structure by single crystal x-ray diffraction will be used to address questions over the precise atomic structure of the high pressure phases which have been reported and thus will also help to explain changes in magnetic structure.

Secondly, whilst some investigations in to high-pressure crystal structure have been carried out on the sister compound $FePSe_3$, similar behaviour has not been previously investigated in detail in the closely related Ni and $MnPS_3$, which related work does suggest undergo simlar volume collapses at extreme pressures. This work will present high-pressure powder and single crystal x-ray diffraction measurements on these compounds for the first time, to launch study of how the subtly different magnetic structures of the MPS_3 compounds affects how their crystal structures respond to hydrostatic pressure. This will then later serve as a starting point for future work into their high-pressure magnetic structures and potential insulator-to-metal transitions.

By exploring these properties in these materials side-by-side with pre-existing knowledge of how they differ in terms of magnetic order, this work begins to build a wider understanding of the interrelated physics at work in this family of compounds which may then be applied to a wider range of related layered magnetic systems and to similar materials which demonstrate unconventional superconductivity.

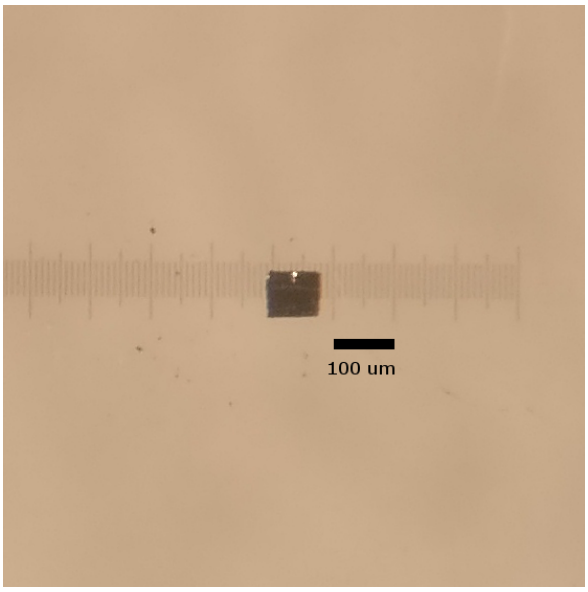

Fig. 4.10 Delaminated single crystal sample of $NiPS_3$ used for high pressure x-ray experiments on I15. Thickness normal to the image plane is ∼15 µm.

4.2 Preparation of samples

Samples of Fe, Ni and $MnPS_3$ were grown by a vapour transport method by A. Wildes at the ILL, Grenoble. Single crystal samples exist as soft platelets up to approximately 50 mm^2 and are easily manually delaminated down to the order of 10 µm thickness without apparent damage to the sample.

Production of high quality powder samples of the materials is non-trivial. Due to the weak van der Waals coupling between the *ab* planes, there is a tendency for these to slide across one another under the application of a shear force, and as a results powders often show significant texture and preferred orientations[70]. To mitigate this, samples of all three compounds were ground using a mortar and pestle being kept filled with liquid nitrogen, and grinding limited to around 1 min to reduce the increase in stacking faults.

For single crystal synchrotron x-ray experiments on I-15 samples of the three compounds were manually delaminated to 10–15 µm thickness and cut by scalpel and razor blade to squares of side length ∼80 µm. Care was taken to ensure that the exposed surface was pristine and free from obvious defects. One such sample of $NiPS_3$ is shown in figures 4.10 and 4.11.

For x-ray experiments, both powder and single crystal samples were loaded into diamond anvil cells by Dominik Daisenberger. For the double toroidal cell used at the ILL the cell was prepared and approximately 30 mm^3 of powdered sample loaded by Stefan Klotz.

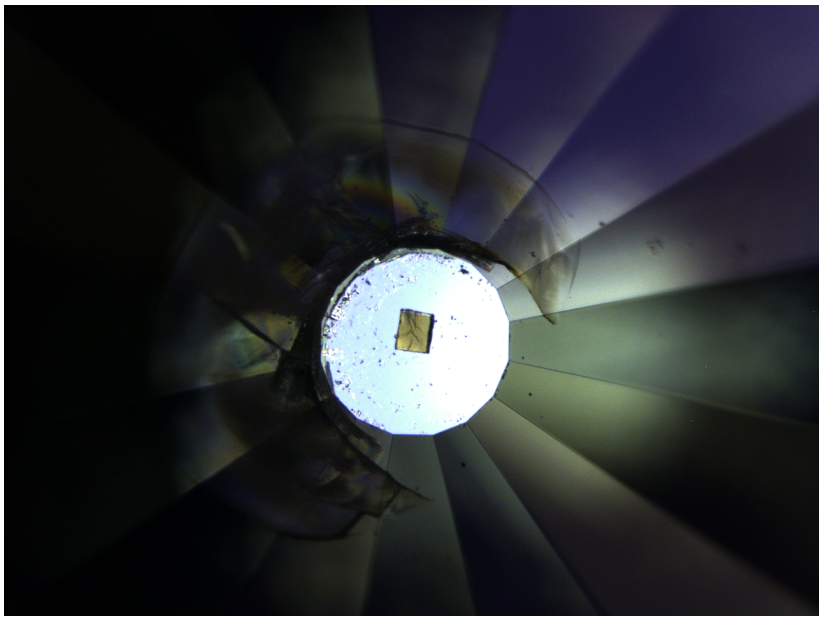

Fig. 4.11 Single crystal $NiPS_3$ sample positioned on a diamond anvil at the I19 beamline at the Diamond Light Source. The average diameter of the culet of the anvil is 400 µm. This image was taken after depressurising the diamond anvil cell and the visible discolouration of the diamond shows the breaking of the diamond which occurred on depressurisation.

4.3 Results

4.3.1 High Pressure Crystal Structures

Powder diffraction patterns at increasing pressures for Ni and $MnPS_3$ are shown in figures 4.12 and 4.13 respectively.

Initially from the observed powder diffraction patterns from both materials, as was originally reported in $FePS_3$ by Haines et al.[60], two distinct structural transitions at ambient temperatures are observed from changes in the diffraction peaks. In $NiPS_3$ the first transition occurs around 10 GPa and the second at 26 GPa. In $MnPS_3$, transitions are observed around 2 GPa and 28 GPa. Hereinafter in all materials, the three distinct phases shall be termed as ambient below the first transition, HP-I the phase existing between the first and second transitions, and HP-II above the second transition.

Good agreement is observed between powder x-ray diffraction patterns measured with the samples in a helium pressure medium and those measured without a pressure medium with the gasket simply filled with MPS_3 powder. This is good indication that both preferred orientations in the sample and the impact of effectively uniaxial pressure is consistent in this case between the different sample environments. The limitation of measurements with a helium pressure medium are in the maximum attainable pressure, which is lower than that

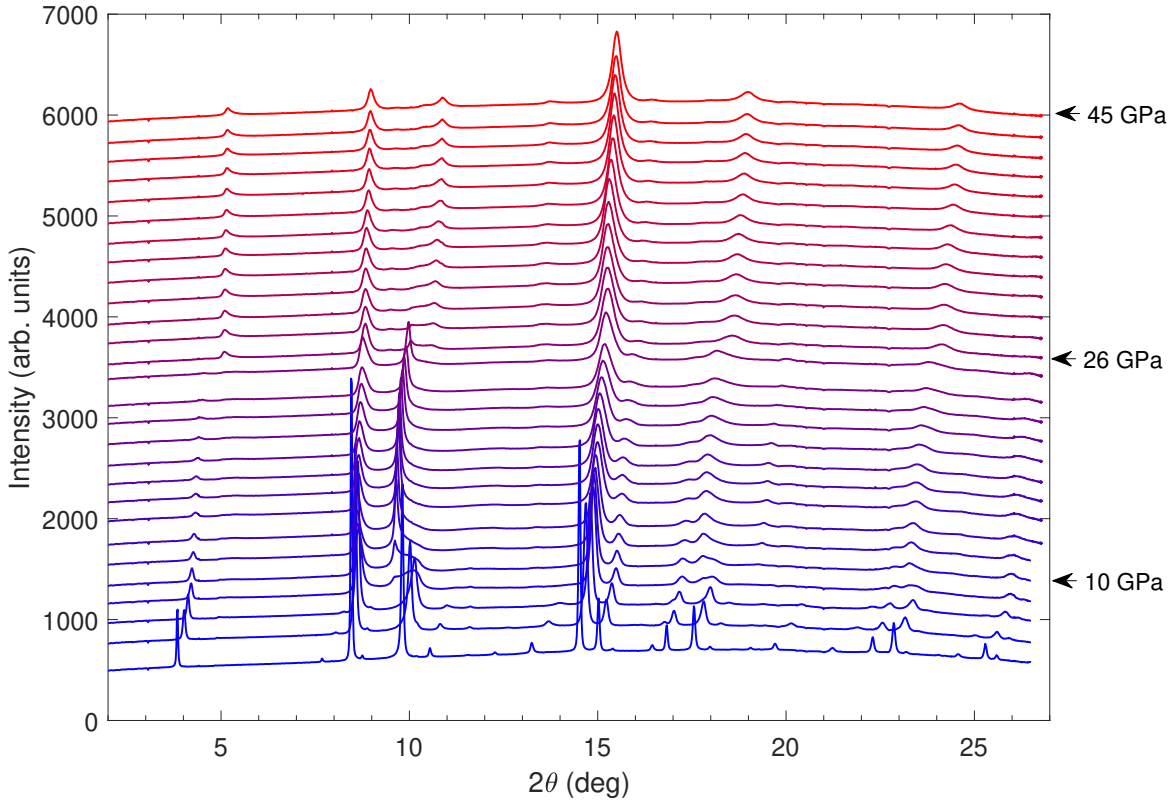

Fig. 4.12 Powder x-ray diffraction patterns for $NiPS_3$ at a range of pressures from ambient to 45.5 GPa. Patterns at increasing pressure are offset for clarity. Alongside expected gradual movement of peaks with increasing pressure, two distinct transitions are observed at pressures around 10 GPa and 26 GPa.

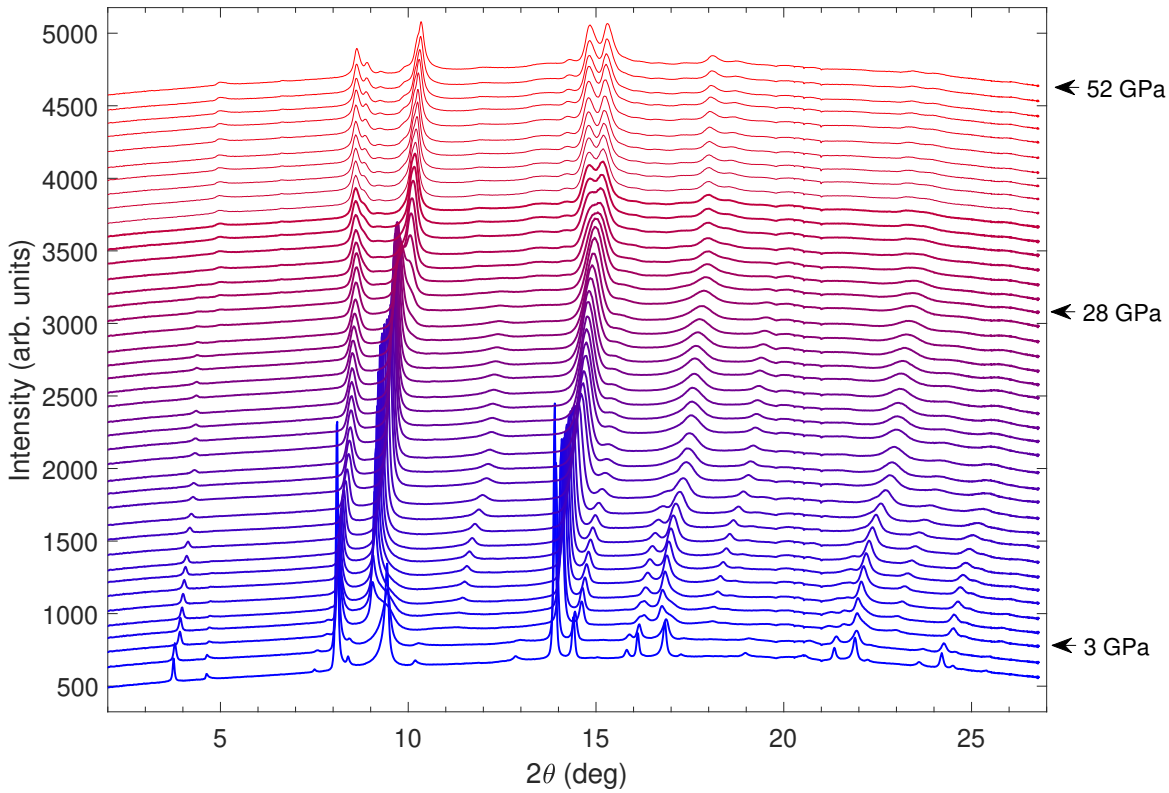

Fig. 4.13 Powder x-ray diffraction patterns for $MnPS_3$ at a range of pressures from ambient to 51.9 GPa. Alongside expected gradual movement of peaks with increasing pressure, two distinct transitions are observed at pressures around 2 GPa and 28 GPa.

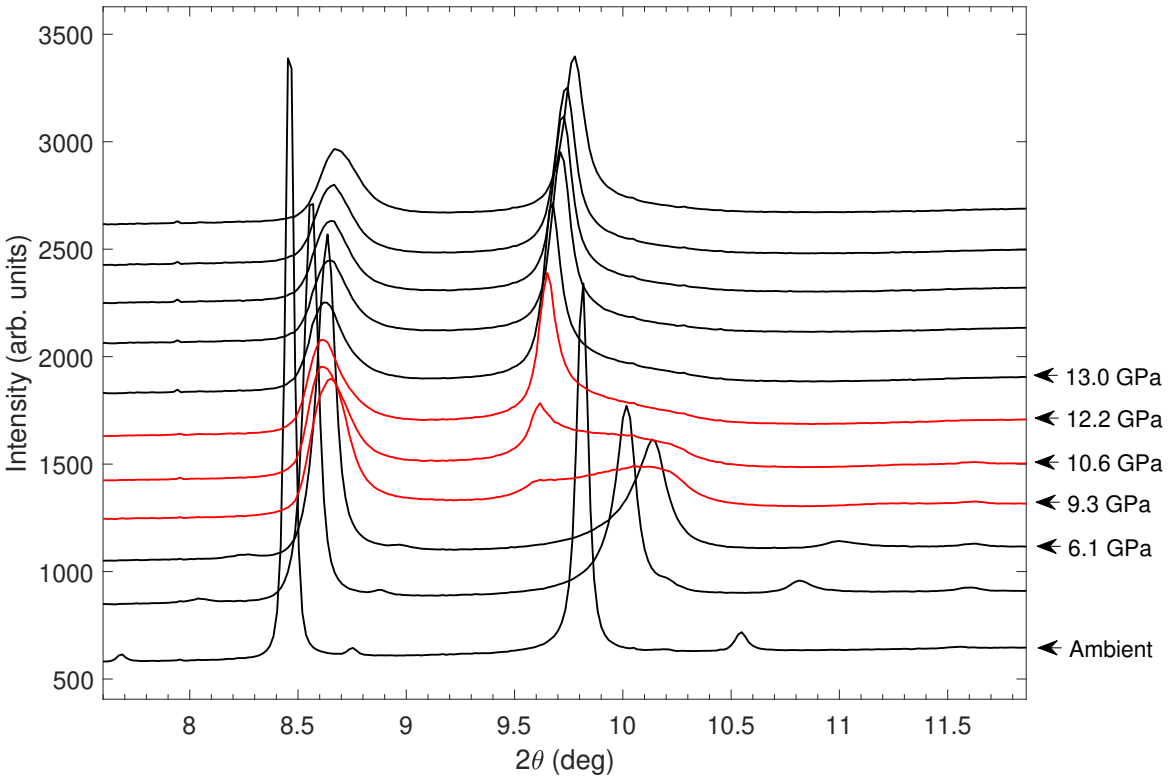

Fig. 4.14 PXRD patterns for a range of pressures across the ambient to HP-I transition in $NiPS_3$. Outside of the highlighted range peaks are seen to shift to higher angle with increasing pressure, corresponding to a gradual compression.

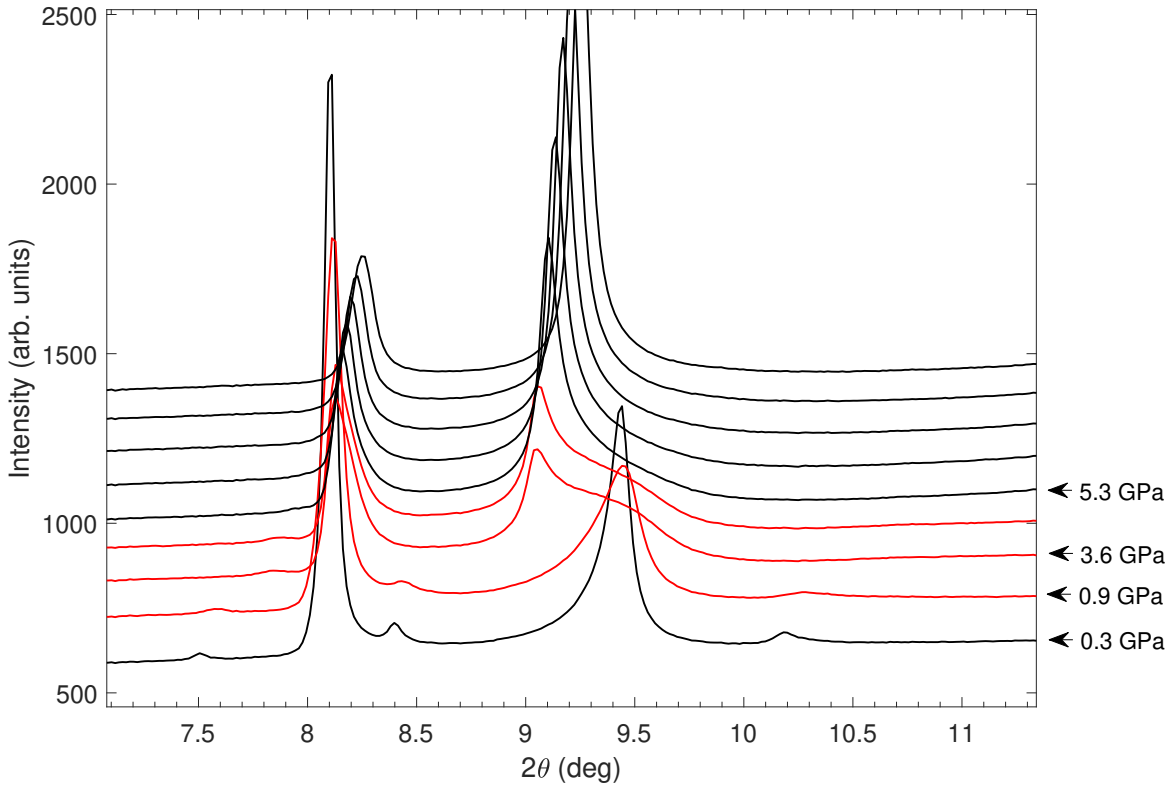

Fig. 4.15 PXRD patterns for a range of pressures across the ambient to HP-I transition in $MnPS_3$. Outside of the highlighted range peaks are seen to shift to higher angle with increasing pressure, corresponding to a gradual compression.

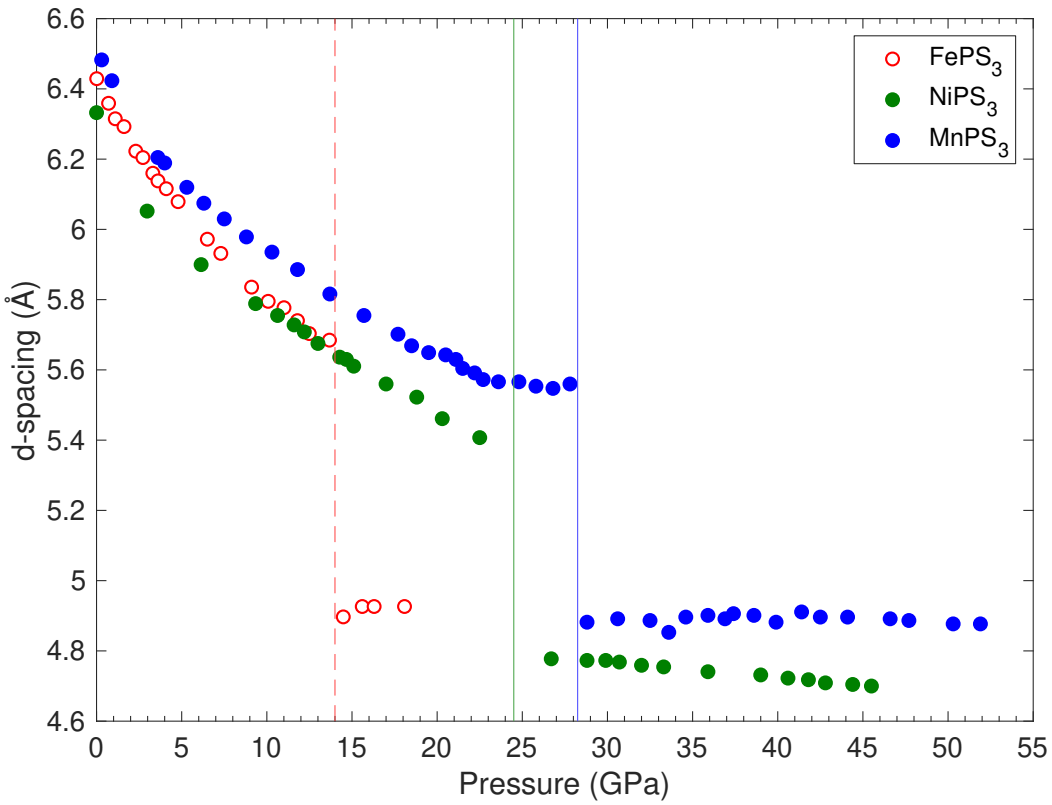

Fig. 4.16 d-spacing corresponding to the observed position of the (001) peak in Ni and $MnPS_3$ (green and blue respectively) from PXRD measurements on I15. Also shown are corresponding results for $FePS_3$ from Haines et al.[60] (red). Vertical lines indicate the structural transitions involving the collapse of the (001) spacing.

which was achieved without. In measurements of $NiPS_3$, the maximum pressure reached for PXRD measurements with medium was 24.6 GPa, which was not sufficient to observe the HP-II transition seen in measurements without. Following this, measurement of $MnPS_3$ was performed only without a pressure medium.

Initial attempts were made to fit the powder diffraction data assuming the the transitions were qualitatively similar to those in $FePS_3$, with HP-I maintaining the $C2/m$ space group with a decrease in angle β and HP-II being a transition to a higher symmetry trigonal-hexagonal space group $P\bar{3}1m$.

Much like the transition in the iron compound, in both Ni and $MnPS_3$, the higher pressure of the two observed transitions from PXRD data appears to involve a collapse of the inter-planar spacing in the layered materials. This is inferred by observation of the monoclinic (001) peak and calculation of the corresponding d-spacing. This d-spacing is shown for the two compounds studied here and for $FePS_3$ from Haines et al. in figure 4.16.

In $NiPS_3$ this transition occurs between the measured pressure points at 22.5 GPa and 26.7 GPa, where the (001) peak changes position from 5.407 Å to 4.778 Å. This decrease of 12 % is similar to that seen in $FePS_3$ alongside metallisation. Above the transition, the (001) spacing is reduced linearly with pressure without further transitions, in agreement with previous $FePS_3$ results that no further restructuring is observed past the HP-I to HP-II transition.

Similarly in $MnPS_3$, between 27.8 GPa and 28.8 GPa, the (001) spacing is reduced by 12 % from 5.56 Å to 4.882 Å. In the manganese compound, the steady near-linear decrease in this spacing through the HP-I phase with pressure is reduced above 24 GPa where it is seen to flatten. Observation of this effect in $NiPS_3$ is not possible to eliminate from the PXRD data due to the lack of closely spaced pressure points near to the transition. In contrast to $NiPS_3$, the (001) spacing in the HP-II phase remains almost constant with no clear linear reduction with increasing pressure. Under the assumption of a similar structure in the two HP-II phases, this suggests that the inter-planar separation in the HP-II phase of $MnPS_3$ is more rigid with pressure than in $NiPS_3$.

From PXRD data alone, whole pattern fitting methods were not able to properly fit the observed HP-II phases in either $NiPS_3$ or $MnPS_3$ leading to the suggestion that the second transition in these materials is qualitatively different to that observed in the iron compound. This was attempted using both a similar $P\bar{3}1m$ space group as observed in the iron compound as well as using the related trigonal hexagonal space group $R3$. Neither Pawley refinement was able to correctly fit measured intensity above the (001) peak. This requires comparison to single crystal diffraction data to determine whether this feature is spurious, arising from some combination of diffraction from the sample environment and strain in the the powder sample. A Pawley refinement of the $NiPS_3$ structure at 29.9 GPa using a $P\bar{3}1m$ space group is shown in figure 4.17.

Contrary to the HP-II phases, from powder diffraction results, the HP-I phases of $NiPS_3$ and $MnPS_3$ may be fit using the same principle as determined by Haines et al. for $FePS_3$: an effective shearing of the weakly coupled *ab* planes giving a reduction the the angle β, but with little effect on the inter-planar separation. With their similar ambient pressure structures differing in β by no more than 0.4°, this angle in both compounds falls to slightly under 90° in an identical transition to $FePS_3$. Diffraction patterns across this transitions for $NiPS_3$ and $MnPS_3$ are shown in figures 4.14 and 4.15 respectively. Both of these transitions to the HP-I phase are also similar to the published data on the iron compound in that the shift of weight from diffraction peaks of the ambient pressure phase to those of the HP-I phase occurs over a pressure window of $\sim$3 GPa.

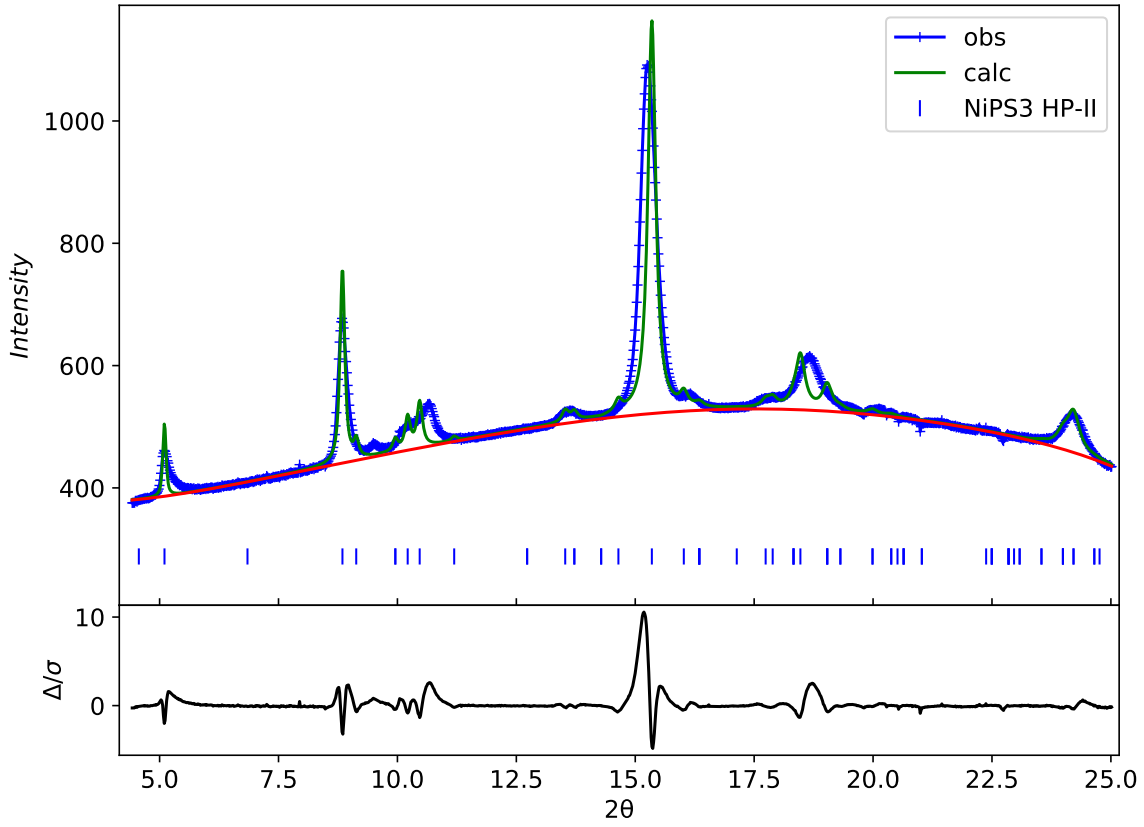

Fig. 4.17 Pawley refinement of powder diffraction data of $NiPS_3$ at 29.9 GPa using a cell determined from single-crystal x-ray results. At this pressure, $NiPS_3$ is in the HP-II phase. Key differences are observed between the single crystal and powder x-ray results, most notably at low angles, where the single crystal proposed structure suggests that the lowest angle observed peak at 5.1° is indexed as the (100) and not the (001).

Similar pressure behaviour is seen again in the higher pressure transition to the HP-II phase, with a gradual shift of spectral weight between the peaks of the two structures and a pressure range of apparent coexistence. In this transition, $MnPS_3$ differs from the two other members of the family with splitting of the (330) and (060) peaks (in the indexing of the HP-I $C2/m$ cell), observable above 28 GPa in figure 4.13, which may indicate that the observed transition to higher symmetry observed in the other two compounds is qualitatively different in $MnPS_3$.

4.3.2 Single Crystal results

Single crystal x-ray diffraction results offer greater clarity to identify and characterise the high pressure crystal structures in Ni and $MnPS_3$ and serve to verify the previously reported high pressure structures of $FePS_3$ from powder data.

At all pressures, the single crystal data show significant loss of resolution of diffraction peaks along the monoclinic c^* direction. This is attributed to the stacking faults in the compounds, with the lack of consistent long-range along that direction resulting in smearing of intensity from sharp peaks in reciprocal space. The effect of this disorder is to reduce the accuracy with which the structure, particularly components normal to the crystal planes, may be determined. This requires utilising the clearer information on the (001) peak from the powder diffraction data to inform starting structures for analysis of the single crystal data.

In $NiPS_3$, two structural transitions are visible from the single crystal diffraction data, at pressures in agreement with experiments carried out on powder samples. The first transition in this compound in single crystal data occurs between the measured pressure points of 5.7 GPa and 10.4 GPa. The scan taken at 8.1 GPa is unable to be confidently indexed at the present time, which suggests that at this pressure the sample is most likely composed a significant mixture of both the ambient pressure and HP-I phases. Attempts to fit this dataset with a mixture of both phases is yet unsuccessful in part due to the presence of stacking faults and the resultant uncertainty in long range order along the crystallographic c direction. The HP-I phase obsered at higher pressures is well fit again by a structure maintaining a $C2/m$ space group but with a reduction of the angle β to 90° within uncertainty. Lattice parameters for the HP-I $C2/m$ cell at 10.4 GPa are given in table 4.7. Within uncertainties, this is in agreement with the first transition from the $FePS_3$ and what is observed from powder diffraction. It is again fit by a maintained space group with the most notable difference being a reduction in the angle β to approximately 90°, describing a sliding of the weakly coupled planes along the a direction.

The critical pressure of the second transition is in agreement with the powder data, being observed between 24.9 GPa and 26.9 GPa. The key difference observed between the

a (Å)	b (Å)	c (Å)	α	β	γ
5.656(11)	9.853(5)	5.74(5)	90.0(3)°	89.4(6)°	90.27(7)°

Table 4.7 $NiPS_3$ lattice parameters derived from single crystal x-ray diffraction measurements at 10.4 GPa. At this pressure the sample has undergone a structural transition to the HP-I phase which maintains a $C2/m$ space group.

a (Å)	b (Å)	c (Å)	α	β	γ
5.423(7)	5.461(6)	5.34(5)	89.3(4)°	89.7(4)°	120.14(12)°

Table 4.8 $NiPS_3$ lattice parameters derived from single crystal x-ray diffraction measurements at 31.1 GPa. At this pressure the sample has undergone a structural transition to the HP-II phase.

a (Å)	b (Å)	c (Å)	α	β	γ
5.906(2)	10.236(3)	5.97(2)	90.11(8)°	90.29(9)°	90.00(3)°

Table 4.9 $MnPS_3$ lattice parameters derived from single crystal x-ray diffraction measurements at 8.0 GPa. At this pressure the sample has undergone a structural transition to the HP-I phase which maintains a $C2/m$ space group.

powder and single crystal diffraction data is the extent of the inter-planar separation which accompanies the increase in symmetry of the second transition. In contrast to results from powder diffraction, single crystal patterns from the HP-II phase of $NiPS_3$ are successfully fit by a trigonal hexagonal $P\bar{3}1m$ structure similar to that of $FePS_3$. The fact that this is not in agreement with powder diffraction data both with and without a helium pressure medium may indicate that preferred orientations in the sample used for the powder diffraction experiment are more significant than previously considered.

Disparity is observed between $NiPS_3$ single crystal and powder x-ray diffraction results in the extent of the collapse of c-axis which takes place in the HP-I to HP-II transition. This is shown in figure 4.18. Under the assumption that the structure determined from single crystal data is correct, it appears that the feature attributed to the (001) in the powder diffraction experiments may instead be due to the (100), with the (001) being reduced in the transition but not to the extent which was previously considered. A comparison of expected peak positions from the unit cell found from single-crystal diffraction compared to observed powder diffraction data is shown in figure 4.19. This explanation that what is counted as the (001) in powder diffraction may instead be the (100) appears unlikely however due to the relative intensity predicted from the single crystal unit cell, as the (001) intensity is approximately 750 times larger than the (100).

Pawley refinement of the powder data at 29.9 GPa using the single crystal derived structure as shown in figure 4.17 fails to fit the position of all peaks well. Using this structure the peak just above 5° and the largest peak above 15° are indexed as the (100) and (300) respectively. As visible from the figure if the position of the lower peak is fit well with a spacing $d = 5.333\,\text{Å}$, the fit of the (300) is misaligned. The positions of maximum intensity of the features at 11° and 19° also do not align with the positions of any indexed peaks, even with the application of corrections for strain and peak broadening in the material.

Assuming that the structures observed in powder and single crystal diffraction are distinct, there are a number of possible effects which may cause the observed difference in the second high-pressure transitions. First, due to the maximum achieved pressure in the powder diffraction experiment being lower with a helium pressure medium, the transition was only observed in powder $NiPS_3$ without medium. In contrast, all experiments on single crystal samples were performed with helium medium. At the high measurement pressures, interaction between the MPS_3 sample and the helium pressure medium cannot be excluded which may in turn effect the critical pressure and nature of the observed structural transitions. Previous studies have been performed into the intercalation of both $FePS_3$ and $NiPS_3$ with lithium. Helium itself is known to penetrate into anvils during such high pressure experiments, further indication that such an effect may be at play in the samples studied here. If this is

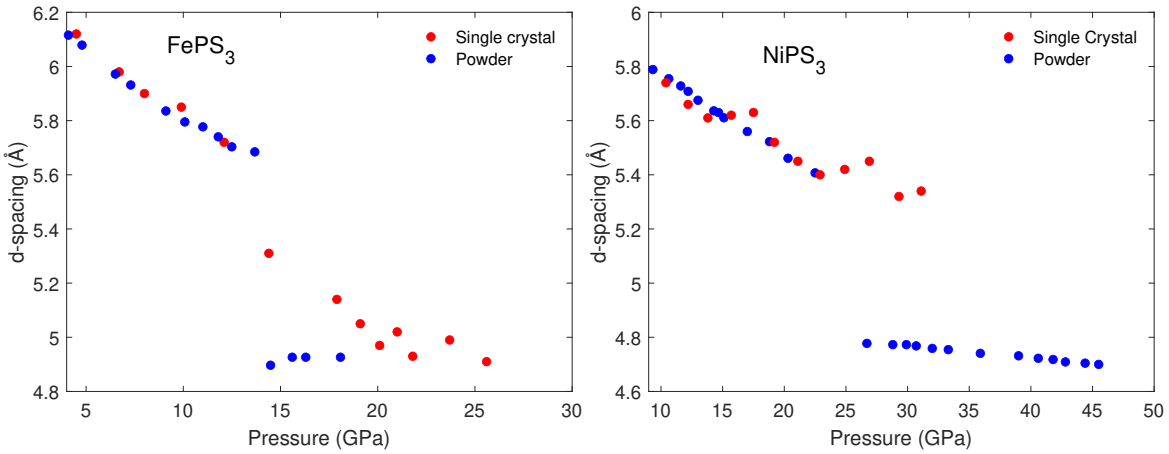

Fig. 4.18 Comparison of the d-spacing of the (001) reflection from powder diffraction to the c-axis determined from single crystal diffraction for $FePS_3$ (left) and $NiPS_3$ (right) above their respective transitions to the HP-I phase. Above this transition the angle β in both crystals is approximately 90° and so these two properties may be directly compared. In both materials the transition to the HP-II phase is visible by the collapse of this spacing in the powder data.

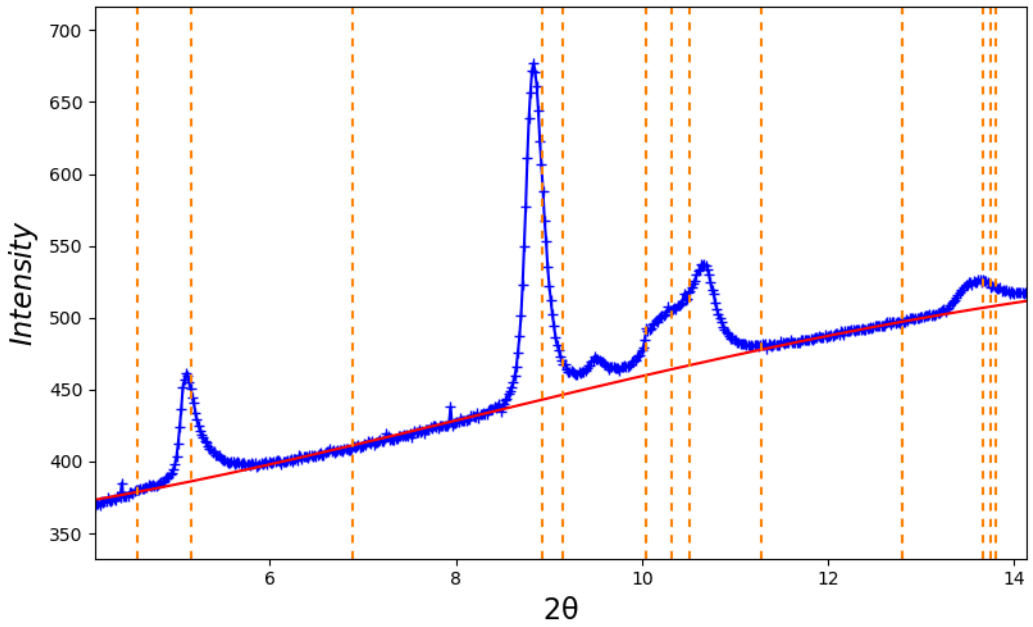

Fig. 4.19 Observed powder diffraction patter of $NiPS_3$ at 29.9 GPa at low 2θ. Vertical lines show predicted peak positions from the $P\bar{3}1m$ unit cell determined from single crystal at similar pressure. The marked position at lowest 2θ is the expected (001), whilst the position at 5.1° overlapping with the observed powder peak is the expected (100).

indeed significant, no effect is observed below the HP-II transition, as noted by the good agreement below that pressure between the powder data with and without medium.

The single crystal study of $FePS_3$ may be directly compared to the published high-pressure powder data published by Haines et al.[60]. As is observed in experiments here for the nickel compound, the two published structural transitions are observed. The highest pressure phase with an onset measured between 14.4–17.9 GPa is again well fit with a trigonal hexagonal $P\bar{3}1m$ space group and consistent with the previously observed critical pressure.

As shown in figure 4.18, comparison of new single crystal results to the published powder data shows a similar effect to the $NiPS_3$ results in which the extent of the reduction in the inter-planar spacing is reduced and observably less abrupt. Whilst the c lattice parameter reaches a similar value of $\sim$4.9 Å in the single crystal, this is only above pressures of 20 GPa. The point measured at 14.4 GPa is noteworthy for a c axis value of 5.31 GPa. From fitting of the diffraction at this pressure, the sample has not undergone the HP-I to HP-II transition and still possesses a $C2/m$ space group. This value of c lies between the two extremes measured in PXRD, at a pressure also between the two either side of the transition. The PXRD results therefore do not exclude the possibility of capturing an intermediate value of c at this pressure.

Alternatively the observation of this intermediate c axis value in $FePS_3$ may challenge the assumption from previous work that structural transition is strongly first order. Previously both transitions have been treated as such, with the coexistence of phases attributed to pressure inhomogeneities in experimental set ups.

Due to constraints on experimental equipment, single crystal data was only measured in $MnPS_3$ at pressures of 0.9 GPa, 2.1 GPa and 8.0 GPa, which was sufficient to measure above the expected pressure of the HP-I transition but well below that of the expected transition to HP-II. A structural transition which maintains the ambient pressure $C2/m$ space group is again seen between the measured pressures of 0.9 GPa and 2.1 GPa, in good agreement with both the powder diffraction results and the pattern of behaviour across the family of compounds. Lattice parameters for the HP-I phase are given in table 4.9. As the pressure of the HP-II transition was not reached in this run, the emergence in powder data of additional peaks suggesting a different symmetry change than observed in Fe and $NiPS_3$ could not be explored further.

4.3.3 High Pressure Magnetic Structure of $FePS_3$

Neutron diffraction results were successfully measured up to a maximum pressure of 18.3 GPa which represents the highest pressure experiment performed to date at the ILL facil-

ity. The viability of the use of double-toroidal diamond anvil cells for this type of experiment is certainly shown. Despite the inherent experimental difficulties, these diffraction results show two distinct changes in the magnetic structure of $\mathrm{FePS_3}$ with increasing pressure which suggest that the arrangement of spins is modified significantly under pressure by the two previously observed structural transitions.

Ambient pressure neutron diffraction patterns at temperatures of 80 K and 300 K are shown in figure 4.20. The data at 300 K my be indexed and refined using the known ambient pressure structures of $\mathrm{FePS_3}$ and the Pb manometer to check that the sample structure is as expected and to exclude from analysis peaks arising from the manometer.

The lowest Q peak observed in the 300 K data appears at $Q = 0.974\,\text{Å}^{-1}$. This is near to the calculated position of the (001) peak of $\mathrm{FePS_3}$ and is indexed as such. This is the lowest Q allowed peak for the material and the absence of any features in the diffraction below this value is confirmation of the purity of the sample and absence of other contamination.

At higher Q, two of the stronger peaks, at $Q = 2.199\,\text{Å}^{-1}$ and $2.538\,\text{Å}^{-1}$ are attributable to the lead manometer as the (111) and the (002) respectively. With the wavelength used, these are the only peaks expected from the unit cell of lead in the angular range 10° to 70°.

Two other strong diffraction peaks are visible at ambient pressure at $2.138\,\text{Å}^{-1}$ and $2.487\,\text{Å}^{-1}$ arising from the $\mathrm{FePS_3}$ sample. The lower Q of these peaks is indexed as a combination of the $(20\bar{1})$ and the equivalent (130) and $(1\bar{3}0)$ peaks, which are unresolvable with an expected difference of $\sim 5 \times 10^{-4}\,\text{Å}^{-1}$ and predicted intensities equal to fractions of a percent.

A weak feature is resolvable at a position near $Q = 2.66\,\text{Å}^{-1}$. This is near the expected position of the $(\bar{1}32)$ and (201) $\mathrm{FePS_3}$ peaks which whilst weaker have expected non-zero intensity.

As expected, additional peaks are observed in the low temperature pattern which may be attributed to te magnetic ordering in the system. At ambient pressure, there is no sharp peak at the expected position of the $(01\frac{1}{2})$ peak, $Q = 0.782\,\text{Å}^{-1}$, and scattering intensity is smeared towards lower angles and the expected (010) position at $Q = 0.610\,\text{Å}^{-1}$. As previously discussed, this is reported in other studies[51] and is expected due to worsening of stacking faults in the compound when crystals are ground to a powder.

A sharper feature is observed at 80 K which is absent in the 300 K data centred at $1.623\,\text{Å}^{-1}$. This feature does show some observed asymmetry which may arise from the peak being a combination of two peaks from the magnetic order. Taking both (010) and $(01\frac{1}{2})$ as being present, these may be combined with extant nuclear peaks to give additional magnetic features as observed.

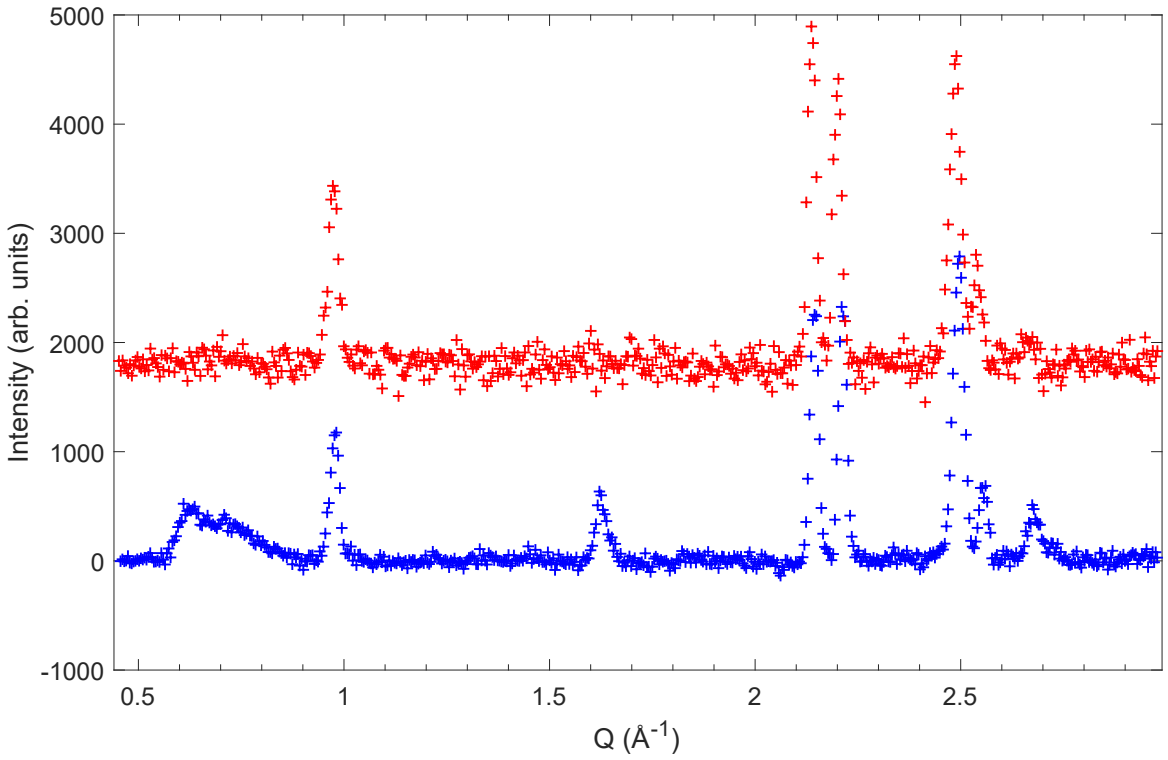

Fig. 4.20 Ambient pressure powder neutron diffraction data of $FePS_3$. Data taken from the experiment using the BN anvils Paris-Edinburgh cell. Data at 300 K shown in red and at 80 K in blue. Data has had background subtracted, and is normalised and offset for clarity.

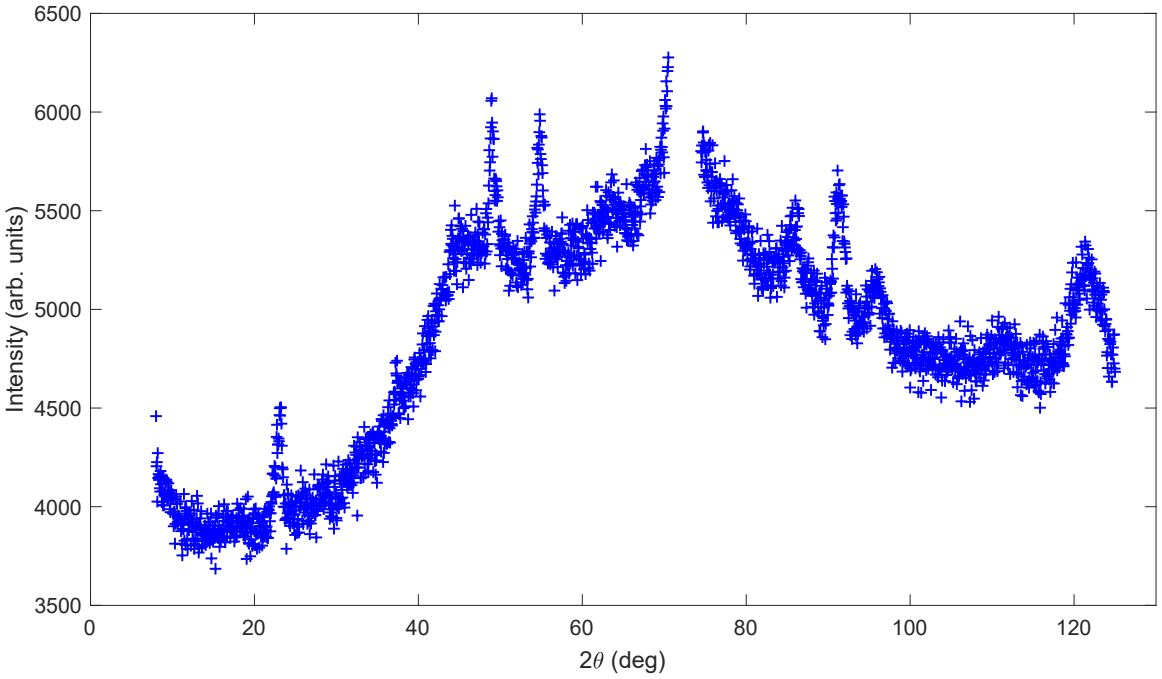

Fig. 4.21 Raw powder neutron diffraction data of $FePS_3$ at 3.3 GPa at 300 K. A region from 70.5° to 74.5° featuring an extremely strong Bragg peak from the diamond anvils has been excluded so that the rest of the range is observable.

The calculated d-spacing and so Q value of the (120) peak, being a combination of the nuclear (110) and a magnetic (010) is very close to that of the $(12\frac{\bar{1}}{2})$, being the combination of the nuclear $(11\bar{1})$ and the magnetic $(01\frac{1}{2})$ at 1.647 Å^{-1} and 1.622 Å^{-1} respectively. Both of these positions fall under the observed peak, with the $(12\frac{\bar{1}}{2})$ position being on the higher Q side where the shallower asymmetry is observed. With magnetic intensity being distributed unevenly between the two magnetic propagation vectors, the observed feature is best fit as a combination of these two magnetic features.

An increase in scattering intensity is also observed at the position of the $(\bar{1}32)$ which appears weakly in the high temperature data. This increase intensity may be due to a reduction in background at low temperature or an additional peak from the magnetic (031) which is structurally forbidden in the $C2/m$ space group but may arise from combination of the magnetic (010) and the structural (022) which is permitted but not observed in either the low or high temperature scan.

Raw data from the lowest pressure point measured in the double-toroidal DAC at 3.3 GPa is shown in figure 4.21.

This illustrates a number of challenges in the analysis of this high-pressure diffraction data. Foremost at approximately 72°, and extremely strong Bragg peak is observed corresponding

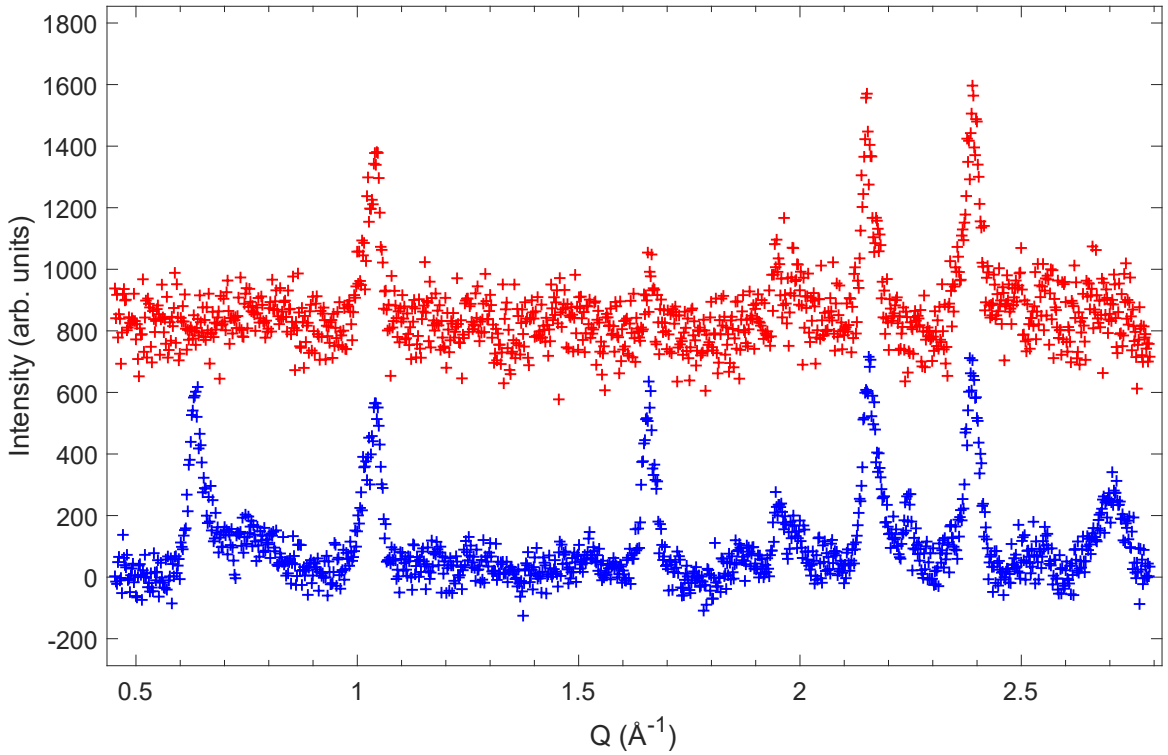

Fig. 4.22 Powder neutron diffraction data of $FePS_3$ at 3.3 GPa. Data at 300 K shown in red and at 80 K in blue.

to diffraction from the sintered diamond anvils. This is orders of magnitude more intense than the rest of the data range and so is excluded from all analysis and fitting. Secondly, away from distinct peaks in the diffraction, the broad diffusive background arising from the methanol-ethanol pressure medium is significant.

Figure 4.22 shows the observed diffraction patterns at 3.3 GPa at both 300 K and 80 K. The data at the temperature below T_N show better statistics and a smaller amount of noise, which is most clear in the background regions away from diffraction peaks. This is due the to the longer measurement time used for the low temperature scan, 180 min as opposed to 60 min for the high temperature scan.

The background has been removed from both of these scans by fitting a smoothing spline to selected background points in the raw data. The use of Chebyshev polynomials is seen to be unable to effectively remove the diffuse background due to the methanol-ethanol pressure medium without using a high number of orders. The simple approach of fitting a spline to manually defined points is effective, but requires confidence in which pattern features are due to external sources and so can be safely removed. A disadvantage of this technique is the requirement of choosing points on each scan to be considered, as the background may vary significantly with pressure due to small movements of the diamond anvils themselves as well

as the pressure transmitting medium. Expected positions of peaks were calculated for both the sample and the anvils, and points showing no observed features in the scan away from these points were selected to which the spline was fit.

In figure 4.22, a clear change in the magnetic structure is seen in the 80 K diffraction data taken at 3.3 GPa. The magnetic intensity which at ambient pressure smeared between the expected (010) and $(01\frac{1}{2})$ position is shifted towards a single sharp peak at the (010) position. By this pressure, $\mathrm{FePS_3}$ has begun to cross over into the HP-I phase, where the angle β has been reduced to close to 90°. This transition maintains the $C2/m$ space group and the indexing of the peaks remains the same.

Despite the emergence of the (010) magnetic peak, a broader feature at higher Q value is still observed at the position of the ambient pressure $(01\frac{1}{2})$, indicating that some fraction of the sample retains this magnetic propagation vector. Haines et al. suggest from their powder x-ray diffraction data that the weight percentage of the two phases at this pressure is approximately 65 % of the ambient pressure phase, and 35 % of HP-I. With the ambient pressure and 3.3 GPa data being taken on different samples, a direct comparison of the distribution of magnetic intensity between the two sets is challenging, as the initial distribution will be skewed by different times grinding the powders and other sample dependent issues.

The magnetic (120) peak which would be expected at a position of 1.65 $\mathrm{Å}^{-1}$ is seen to overlap with a stronger reflection which is attributed to diffraction from the diamond anvils. Whilst with the utilised neutron wavelength of 2.42 Å no diamond peaks are expected in the region of interest, the three peaks at 1.01 $\mathrm{Å}^{-1}$, 1.66 $\mathrm{Å}^{-1}$ and 1.95 $\mathrm{Å}^{-1}$ can be indexed with the unit cell of diamond and a wavelength of $\frac{\lambda}{3}$. This indicates that despite the graphite monochromator used, some intensity of $\frac{\lambda}{3}$ neutrons were incident on the sample and must be accounted for in analysis. At 3.3 GPa, these additional diamond peaks overlap with two feature of interest in the $\mathrm{FePS_3}$ diffraction: the aforementioned magnetic (120) and the structural (001). The change of d-spacing of the (001) plane does not change drastically on the ambient to HP-I transition and should gradually move to shorter d-spacing (higher angle) as pressure is increased. In comparison to the sample, any change in the position of diffraction peaks from the diamond is expected to be minimal.

This change to long-range (010) ordering represents a halving of the magnetic unit cell such that it now the same as the structural unit cell. It indicates a change in the magnetic coupling between the $\mathrm{Fe^{2+}}$ planes from being antiferromagnetically to ferromagnetically coupled. The shear of the ab planes alters the stacking of the metal and ligand ions which likely results in a change of the magnetic exchange pathways between the layers in the compound. The ambient pressure interlayer exchange is very small ($J' = -0.0073(3)$ meV)

and so changing this to a positive value corresponding to ferromagnetic inter-planar coupling is reasonable for the energy scales involved.

The ambient to HP-I structural transition coinciding with a transition to ferromagnetic inter-planar magnetic order is qualitatively consistent with the magnetic order observed in ambient pressure powder samples being limited in extent along the crystallographic c direction due to stacking faults. The act of grinding $FePS_3$ may result in shearing of the ab planes parallel to the a-axis similar to that which occurs in the HP-I transition. This incomplete shearing then gives rise to short-range rod-like ordering with the $\mathbf{k}_M = [010]$ propagation vector, with some fraction of the sample retaining the pristine $\mathbf{k}_M = [01\frac{1}{2}]$. In the measured transition under pressure, this transition in consistent throughout the powder sample and so gives instead the long-range $\mathbf{k}_M = [010]$ magnetic order. This change to long range order is also consistent with the expected behaviour of the crystal becoming more three-dimensional.

Diffraction scans taken whilst the sample was being warmed from 80 K to 300 K allow for the evolution of magnetic features to be tracked as a function of temperature. This is shown for the 3.3 GPa data in figure 4.23. T_N is determined by observation of the temperature at which the (010) feature at 0.64 Å^{-1} is no longer resolvable. Due to the noisy data from the shorter scans on warming, confidant determination of this temperature is non-trivial. With increasing temperature about the critical temperature, the relative intensity of the (010) diffraction peak is reduced until it is no longer present above T_N. Starting at lower temperatures, a gaussian was fit to the diffraction peak using the `fit(x,y,'gauss1')` function in MATLAB. Before this process, the data was cut down to an angular range $\sim 3°$ either side of the relevant peak and a linear background subtracted over this region. The magnetic feature was characterised with the three parameters of the gaussian function: a, the height of the peak; b, the position of the peak centre; and c, the standard deviation determining peak width. A discontinuous jump or increase in the uncertainty of two of more of the parameters was taken as showing that the peak was no longer reliable distinguishable from the background. Due to the noisy nature of the data, in this study, T_N was not extrapolated from the intensity of the gaussian, but determined to lie somewhere between the highest temperature where the peak was resolved and the lowest where it was not. An example of this fitting for scans taken at 7.8 GPa is shown in figure 4.24, in which it can be seen that the magnetic feature is no longer fit by the function at 138 K and above.

For the 3.3 GPa data, the feature is seen to disappear at $127(2)$ K, which at slightly above the ambient pressure T_N value, follows the expected trend of increasing T_N with increasing pressure. Structural features of $FePS_3$ and diamond are observed to be unchanged

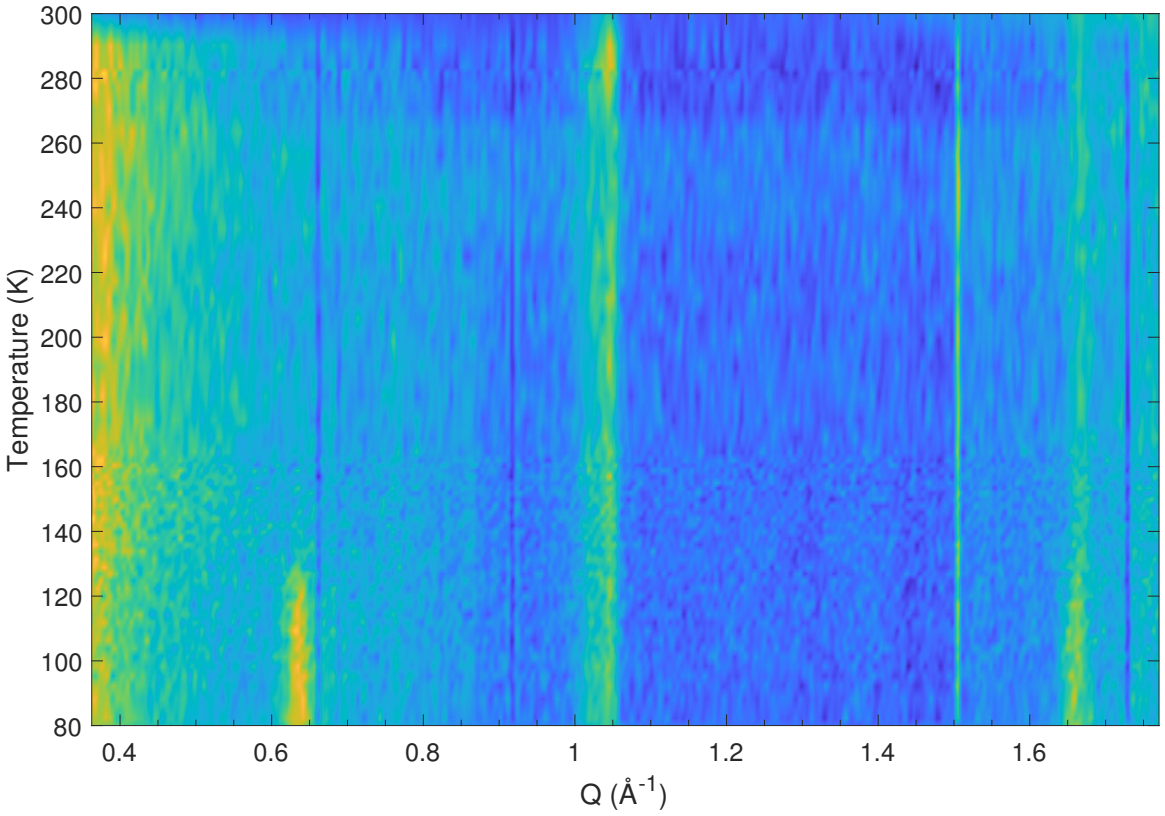

Fig. 4.23 Scattered neutron intensity as a function of Q and temperature at 3.3 GPa. Note the reduction in temperature resolution above 165 K due to the increase in temperature ramp rate at that point.

in temperature. Whilst structural peaks of $FePS_3$ may be expected to move in Q with temperature due to thermal contraction, this is not observed with the resolution of this study.

The comparative temperature evolution of the broad $(01\frac{1}{2})$ magnetic feature and that of the sharper (010) peak is difficult to determine, with the former not being well resolved in the shorter scans taken whilst warming. No difference is naively expected if indeed this change to $\mathbf{k}_M = (010)$ is the same as is seen on grinding of the powder sample, as the ambient pressure data shows, the broad magnetic feature falls to zero above the background at the ambient Néel temperature.

With regards to the crystal structure itself at 3.3 GPa, the structural peaks observable in the neutron diffraction pattern are as expected from both the published crystal structure and from the single crystal x-ray experiment discussed in this work.

Increasing the pressure to 7.8 GPa, the relative intensity of the (010) peak is seen to increase further. At this pressure the system should be almost entirely in the HP-I phase, and so a greater shift of magnetic intensity to the (010) peak from $(01\frac{1}{2})$ is consistent with

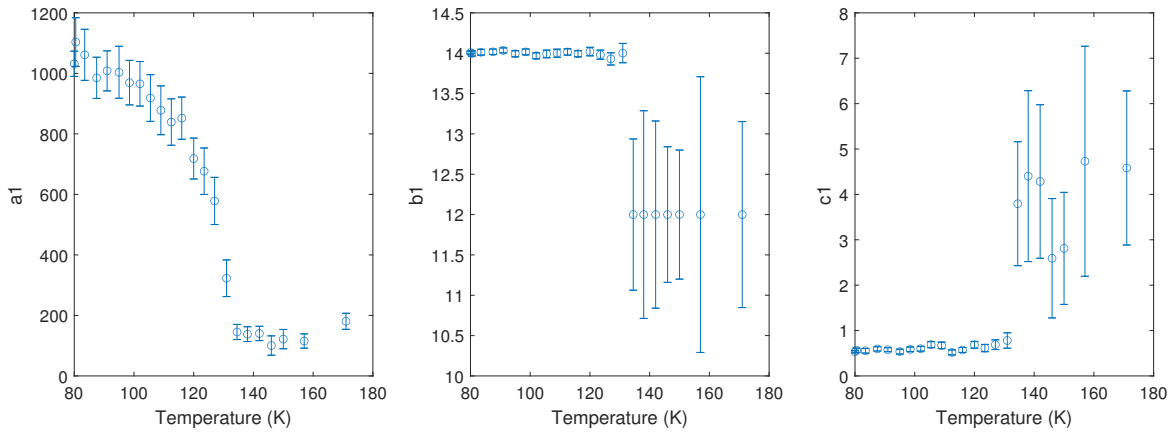

Fig. 4.24 Parameters of the gaussian fit to the (001) magnetic scattering feature at 7.8 GPa. The breakdown of a common trend at 138 K in both b and c is evidence that the feature can no longer be reliable resolved from the background.

losing intensity from any fraction of the sample remaining in the ambient pressure phase. Diffraction patterns above and below T_N at this pressure are shown in figure 4.25. Continuing the trend, T_N is increased further from the data taken at lower pressures. By the evolution of the (010) peak with temperature, $T_N = 136(2)$ K at 7.8 GPa.

By this pressures, the (001) peak of $FePS_3$ may be distinguished from the $\frac{\lambda}{3}$ diamond (111) peak. The sample peak is shifted by the increasing pressure to a position $Q = 1.05\,\text{Å}^{-1}$ whilst the diamond peak is resolvable at the lower $Q = 1.02\,\text{Å}^{-1}$. This fits with the asymmetrical peak observed around this position at 3.3 GPa, with the shoulder on the low-Q side arising from the diamond anvils.

Additional magnetic features may resolved in this scan, again consisting of combinations of magnetic and nuclear $FePS_3$ peaks. The feature at $1.66\,\text{Å}^{-1}$ persists up to 300 K but loses intensity above the T_N which is derived from the (010) peak. This is attributable to the overlap of the (022) peak from the diamond anvils and the (120) $FePS_3$ peak (which arises as a combination of the magnetic (010) and the nuclear (110)). The nuclear (110) itself is weak and barely resolvable above the background at around $1.26\,\text{Å}^{-1}$.

Another feature is seen in the long scan at 80 K between $Q = 2.24$–$2.29\,\text{Å}^{-1}$. Likely candidates for this are the (210) or (012) peaks again arising from the magnetic (010) with the nuclear (200) and (002) peaks respectively. Whilst this feature is clear in the long 80 K scan, resolution in the warming scans is insufficient to track its temperature evolution with certainty, though its absence is apparent in the 300 K measurement.

Diffraction patterns taken at a pressure of 10.3 GPa are shown in figure 4.26. From previous studies, at 10.3 GPa, $FePS_3$ should still be almost entirely in the HP-I phase, with the onset of the transition to HP-II beginning at $\sim$12 GPa. Nonetheless, as with the transition

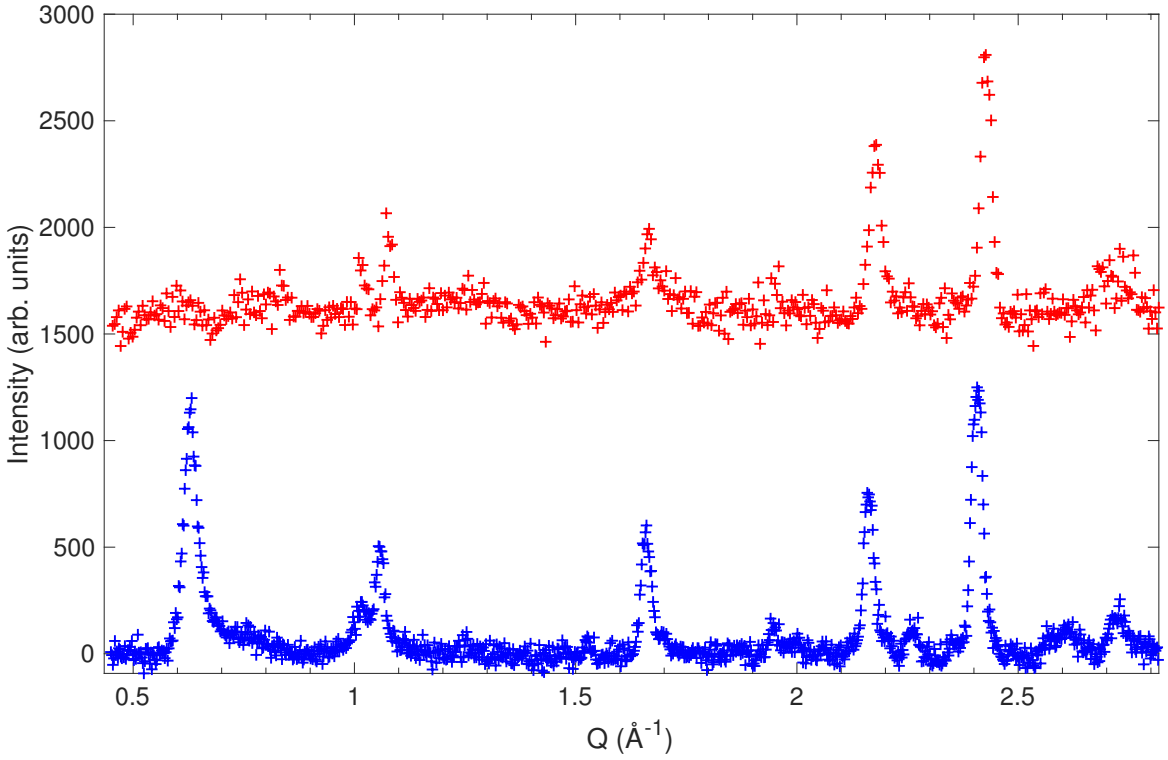

Fig. 4.25 Powder neutron diffraction data of $FePS_3$ at 7.8 GPa. Data at 300 K shown in red and at 80 K in blue. Patterns have had a background subtracted and are offset for clarity.

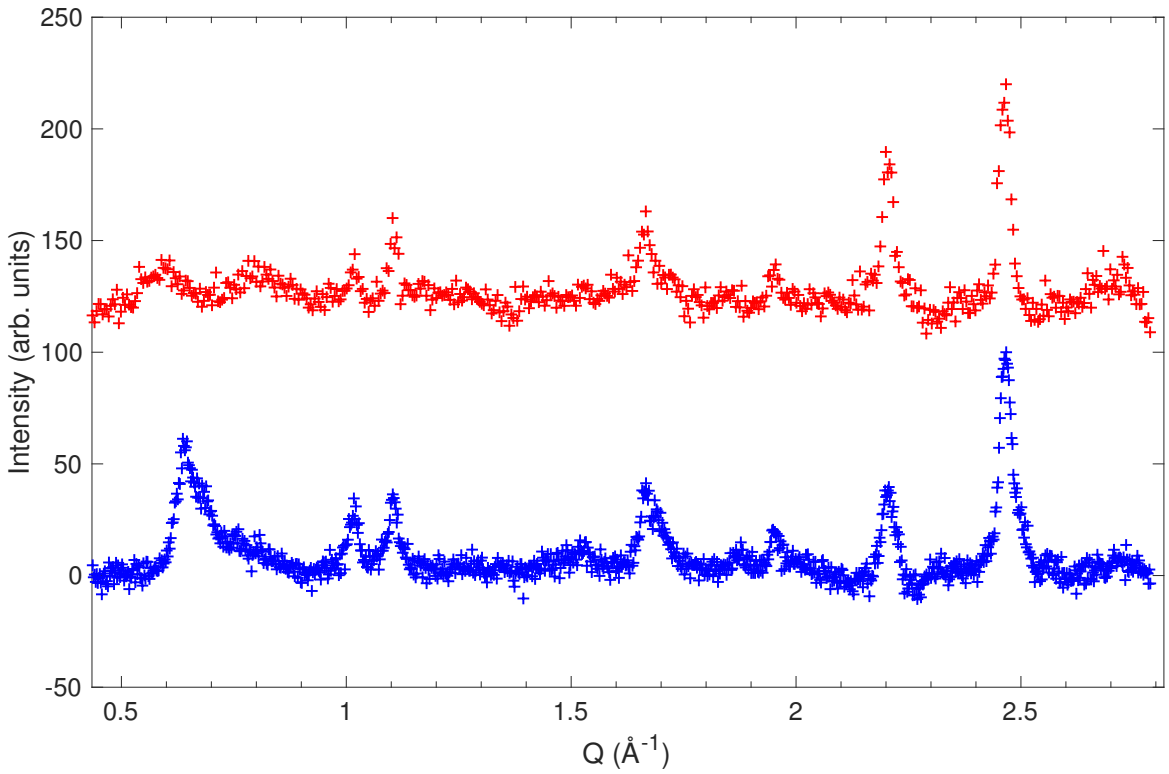

Fig. 4.26 Powder neutron diffraction data of $FePS_3$ at 10.3 GPa. Data at 315 K shown in red and at 80 K in blue. Patterns have had a background subtracted and are normalised and offset for clarity.

from $\mathbf{k}_M = (01\frac{1}{2})$ to $\mathbf{k}_M = (010)$ magnetic order, some crossover to the highest pressure magnetic state is seen in the diffraction data taken at 10.3 GPa. Whilst the magnetic peak at the (010) position is still observed, asymmetry has developed with additional weight on the high-Q side. Additionally above the (010) peak, scattering intensity is seen out to 0.8 Å^{-1}, at the position at which the broad feature corresponding to the high-pressure short range order is seen clearly at 18.3 GPa.

Again, if the structural transition is strongly first order, the coexistence of these two magnetic phases is most likely due to pressure inhomogeneity and gradients in the pressure cell, with some fraction of the sample experiencing a greater pressure causing it to undergo the transition to HP-II and the new magnetic state. The magnetic (210) or similar is no longer well resolved around 2.25 Å^{-1}, which may be due to the overall loss in intensity compared to the 7.8 GPa scans of approximately one third.

At 300 K at 10.3 GPa, a feature is visible in the scattering data at 0.58 Å^{-1}, corresponding to longer range than even the $\mathbf{k}_M = [010]$ magnetic order seen at low temperature. The feature is broad but distinct from the increasing low-Q background seen in all scans. Such a feature

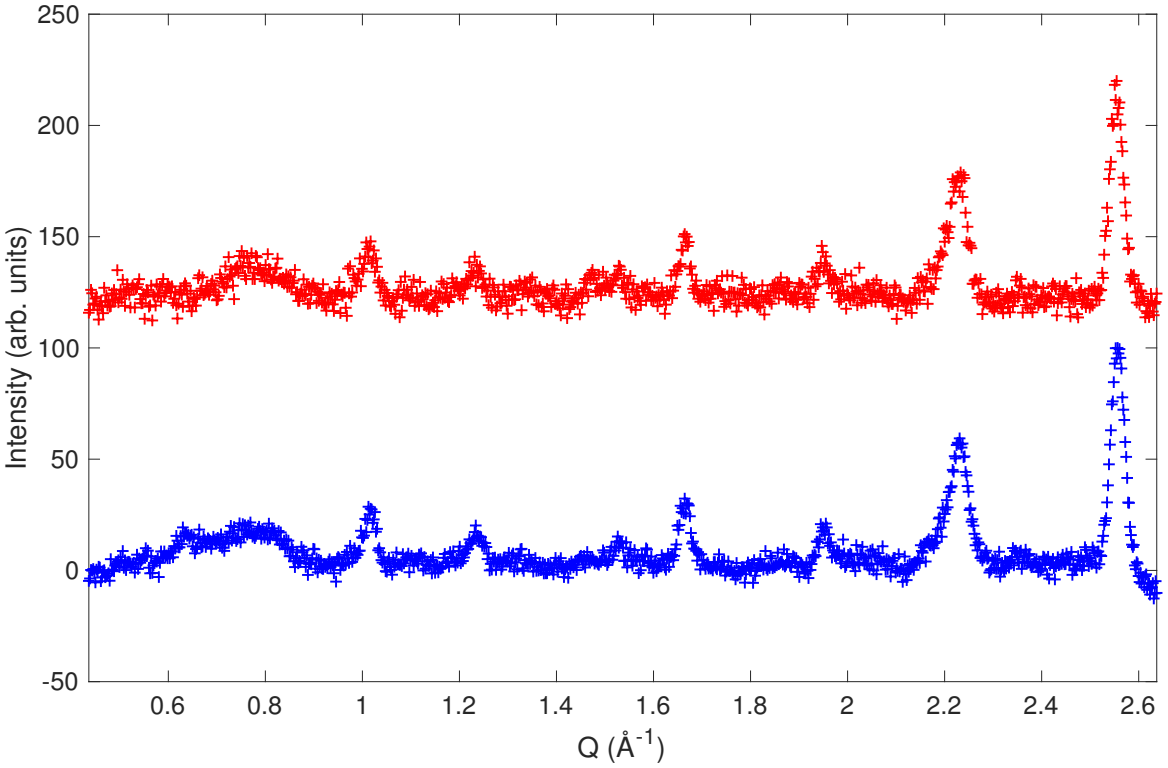

Fig. 4.27 Powder neutron diffraction data of $FePS_3$ at 15.7 GPa. Data at 300 K shown in red and at 80 K in blue. Patterns have had a background subtracted and are normalised and offset for clarity.

is observed but less intense in the data at 7.8 GPa. In the $FePS_3$ structures there is no reasonable explanation for such a feature, and its lack of visibility at 80 K suggests it arises from some background feature from the pressure apparatus, as does the underlying increasing background at the lowest values of Q. This further illustrates the challenges of treating complex backgrounds in high pressure data whilst preserving all features of interest.

The general form of the higher Q scattering peaks is largely unchanged from scans taken at 7.8 GPa save for the absence of the magnetic (210). Asymmetry is observed of the diamond peak at 1.66 Å^{-1}, with additional spectral weight on the higher Q side. In a similar manner to the separation of the (001) peak from the diamond peak at 1.02 Å^{-1}, this is most likely the emergence of the magnetic (120) to higher Q, as is seen to a lesser degree in scans at ambient pressure.

At 15.7 GPa, the majority of the sample of $FePS_3$ has undergone the HP-I to HP-II structural transition and exists in the trigonal-hexagonal $P\bar{3}1m$ structure. Diffraction patterns at 15.7 GPa are shown in figure 4.27.

From observation of the scattering features at low-Q, it is evident that there is once again some coexistence of features from the $\mathbf{k}_M = [010]$ ordering and from the short range order observed at the highest pressures. A small peak is present at $Q = 0.63\,\text{Å}^{-1}$ which follows from the continued suppression of the lower pressure structure. Below this at $Q = 0.50\,\text{Å}^{-1}$ another small peak is weakly resolvable over the decreasing background which is not apparent in measurements at either higher or lower pressures. This feature may also be present in the data taken at 300 K and does not appear attributable to the $FePS_3$ sample itself. Further separating the $\mathbf{k}_M = [010]$ magnetic order from the higher pressure short range order is the persistence of the latter up to at least 300 K where the (010) peak is not visible. At this pressure, determination of T_N for the lower pressure order is not possible due to the prohibitively long scan times required. This difference of temperature evolution is good evidence that the magnetic orders are separate and distinct which is in agreement with the expected first-order nature of the transition. As with results from x-ray diffraction, co-existence of the two phases is likely due to pressure inhomogeneities within the sample environment.

With the sample having undergone the transition to the HP-II $P\bar{3}1m$ structure, the indexing of the prominent diffraction peaks seen at this pressure is altered. At $1.24\,\text{Å}^{-1}$, the (001) remains similar in form to that in the lower pressure $C2/m$ phase due due to the value of β in that phase being very close to 90°. In comparison to the 10.3 GPa data, the position of the structural (001) peak is shifted to higher Q by $0.132\,\text{Å}^{-1}$, corresponding to a reduction of the (001) spacing in real space by 0.610 Å. The greater change with pressure between these points is in agreement with what is expected from the HP-I to HP-II transition in powder x-ray data, as a result of the c-axis collapse.

At higher Q, the two most prominent diffraction peaks observed at $2.23\,\text{Å}^{-1}$ and $2.56\,\text{Å}^{-1}$ are indexed as the trigonal (110) and (111) respectively. Besides the near-constant diamond peaks, the feature at $1.53\,\text{Å}^{-1}$ is more prominent than at lower pressures. At lower pressures, this feature was only present in measurements at 80 K and was not well resolved in warming measurements up to T_N likely to due to the reduced counting time and the low intensity. At this pressure however some signature of the peak remains at 300 K. This may be further evidence of the magnetic origin of this feature. However unlike most features arising from the $FePS_3$ sample, this peak remains fixed in Q which is of note considering the significant change in both the lattice parameters and the unit cell itself across the pressure range.

In the highest pressure HP-II phase, the onset of which coincides with metallisation of the material, a second distinct change in the magnetic structure is observed. The sharp (001) peak from the previous magnetic structure is lost, and no sharp Bragg peak which can be associated to any long-range order is observed at the highest pressure of 18.3 GPa. Instead, a

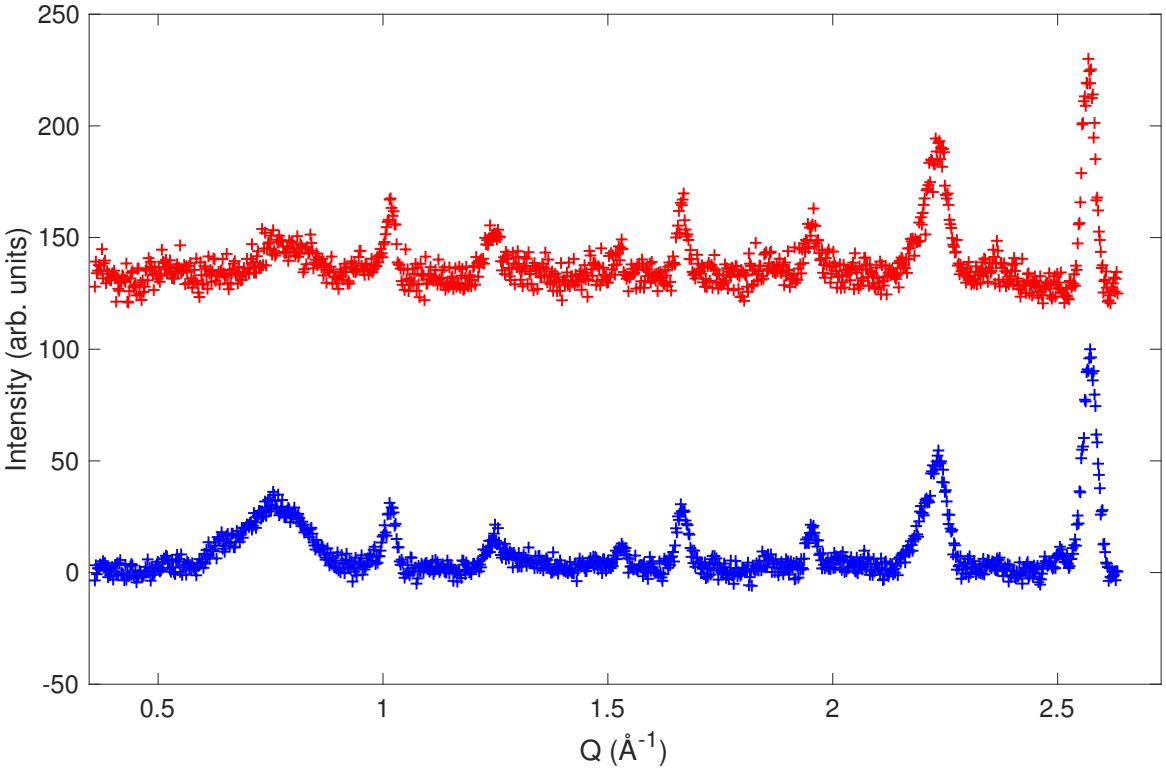

Fig. 4.28 Powder neutron diffraction data of $FePS_3$ at 18.3 GPa. Data at 300 K shown in red and at 80 K in blue. Patterns have had a background subtracted and are normalised and offset for clarity.

broad feature at lower Q, between 0.5–0.95 Å^{-1} maximal at 0.76 Å^{-1}, appears in scans at both 80 K and 300 K. Scans as a function of temperature at this pressure are coarse due the the necessary collection time, but extrapolation from these results suggests that this feature would be extinct above 360 K. Diffraction patterns at 80 K and 300 K are shown in figure 4.28.

The HP-I to HP-II structural transition is first order, with Haines et al.[60] reporting a range of approximately 12–16 GPa for complete transformation, but coexistence of the two magnetic structures seen in powder neutron diffraction results in the existence of a shoulder on the low Q of the broad feature at at Q value which can be attributed to the (010) position in the monoclinic indexing. As in other cases this is most likely attributed to pressure inhomogeneities in the sample region, with some fraction of the sample still remaining in the lower pressure magnetic phase.

Such a broad feature at this positions is indicative of short range magnetic order, and attempts to characterise this were carried out with assistance from J. Paddison (ORNL). Reverse Monte Carlo (RMC) simulations of potential configurations of spins within the unit

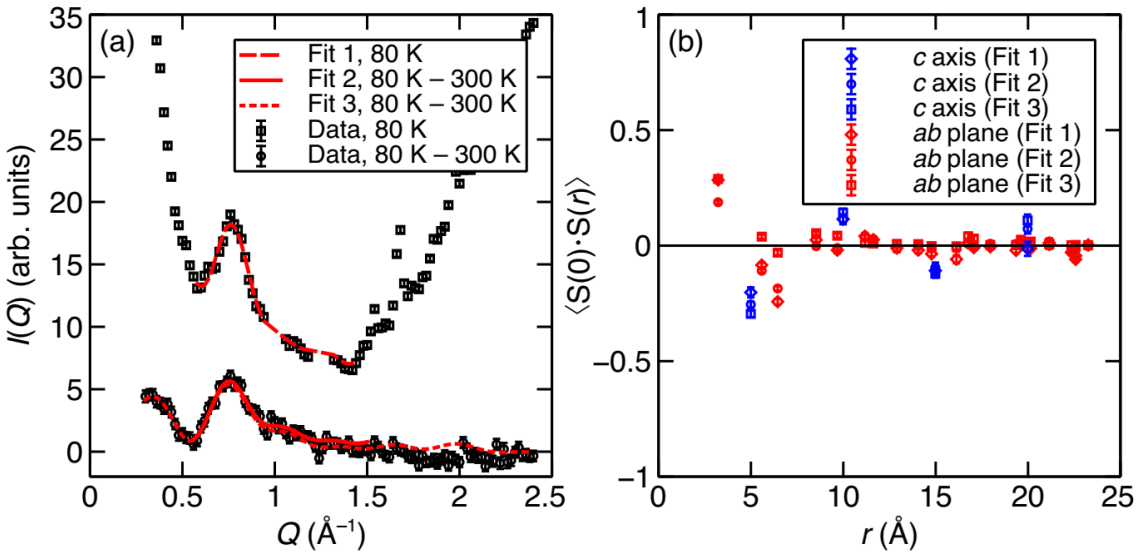

Fig. 4.29 (Left) Experimental neutron diffraction data from $FePS_3$ at 18.3 GPa with fits produced by reverse Monte Carlo simulations. (Right) Spin-spin correlation functions $< \underline{S}(0) \cdot \underline{S}(r) >$ as a function of inter-atomic spacing in $FePS_3$ at 18.3 GPa, found by reverse Monte Carlo simulations. Values are normalised such that perfect ferromagnetic exchange is a value of $+1$ and perfect antiferromagnetic exchange is a value of -1.

cell were carried out and resultant simulated diffraction patterns fit to the experimental results. These simulations were performed using Spinvert software[89, 90]. To reduce the impact of background scattering on the fit, several fits were performed the results of subtracting the 300 K data from that taken at 80 K (both at 18.3 GPa). Due to the persistence of the SRO feature to above 300 K, this subtraction results in the loss of some apparent intensity which requires consideration for interpretation of its results. Three fits were performed, each limited to a low Q range encompassing the SRO feature. Fit 1 was to the raw 80 K data without subtraction over a range of $Q = 0.58$–1.42 Å^{-1}; fit 2 to temperature-subtracted data from $Q = 0.56$–1.50 Å^{-1}; and fit 3 from $Q = 0.30$–2.40 Å^{-1}.

From this fit, the spin-correlation function $< \underline{S}(0) \cdot \underline{S}(r) >$ is extracted, which quantifies the extent of magnetic interaction between sites. These values are normalised to the range -1 to 1, where 1 corresponds to complete ferromagnetic exchange and -1 to perfect antiferromagnetic correlation. $< \underline{S}(0) \cdot \underline{S}(r) >= 0$ for two sites separated by a distance r indicates no magnetic interaction between those sites and thus the absence of any magnetic order on that length scale. Results from this fit are shown in figure 4.29.

The precise correlation functions extracted from fits to the three data sets differ numerically but show consistent trends from which the magnetic structure may be qualitatively described. It can be seen that the nearest neighbour (intra-planar) interaction is ferromagnetic,

whereas the interaction between the hexagonal Fe^{2+} planes is antiferromagnetic with the neighbouring planes and this interaction persists over several unit cells along c. The next and next-nearest neighbour intra-planar interactions are also antiferromagnetic. This arrangement of interactions is qualitatively similar to the ambient pressure $\mathbf{k}_M = [01\frac{1}{2}]$ structure, noting the antiferromagnetic inter-planar coupling. As discussed for the first magnetic transition, the low value of the inter-planar exchange means that the system is highly sensitive to changes of the crystalline structure, and a return to a negative value of J' is physically reasonable. The value of $< \underline{S}(0) \cdot \underline{S}(r) >= 0.19$ for intra-planar nearest neighbours is indicative that ferromagnetically coupled chains likely persist in the HP-II phase, although unlike the lower pressure phases, the Fe^{2+} layers in HP-II are formed of perfect hexagons, meaning that these chains may not have a preferred direction as they do along the crystallographic a-axis in the lower pressure structures. The value indicates that only some fraction of the nearest neighbour ions are coupled in this manner, giving the order the short range nature which is observed in the diffraction patterns.

Normalisation of the data in this fitting process using nuclear Bragg profiles yields a large effective magnetic moment of 6.6 μ_B per Fe^{2+} ion. This is larger than the ambient pressure value of 5.7 μ_B from literature[68] but within uncertainties due to the calculation technique. The value found here is calculated under the assumption of an accurate crystal structure from the neutron data and in the absence of absorption effects, which is not trivially true for such high pressure experimental studies. With the observed short-range order persisting up to above 300 K, the temperature subtraction used for the moment determination underestimates the true value of the scattering feature, and so the effective moment in the HP-II phase may be higher than the calculated value.

4.4 Discussion

It is apparent from the powder diffraction experiment presented here that the magnetic structure of $FePS_3$ undergoes significant modifications under the application of pressure which appear to coincide with the previously reported transitions in the crystal structure. As the material passes through the first transition to the HP-I structure, an overall antiferromagnetic is retained but the type of this antiferromagnetism is modified from an arrangement of ferromagnetic chains along the crystallographic a direction being antiferromagnetically coupled to both their neighbours within the ab plane and the nearest chains in adjacent planes along c, to a structure in which the latter relation is modified so that the the inter-planar coupling becomes ferromagnetic.

The observation of this first magnetic transition is significant for the understanding of previously observed changes in magnetic order which occur on grinding the compound to a powder. Previous work has indeed noted the inducement of a two-dimensional nature of the principal magnetic peak by sample grinding and suggested a link to the well known existence of stacking faults in the material, but this work for the first time demonstrates the microscopic origin of this effect. Grinding samples to powder most likely replicates the observed ambient pressure to HP-I transition: a shearing of the weakly couples planes along the crystallographic *a* direction. This work demonstrates that this is accompanied by a change in the inter-planar magnetic coupling, which may likely be attributed to the change in the stacking of the metal and ligand ions in the transition. This is visible from the sharpening of the (010) diffraction peak from the sample in which in which some amount of magnetic intensity exists there at ambient pressure due to grinding effects, accompanied by a loss of intensity at the known value of the ambient pressure magnetic scatting vector (in the absence of stacking faults or similar effects) of $(01\frac{1}{2})$. Establishing this link between stacking faults, strain and changing magnetic order in the system, even at very low pressures is has significant implications for the growing area of device physics using this family of materials, in which such effects must be accounted for.

The higher pressure structural transition to the higher symmetry $P\bar{3}1m$ trigonal hexagonal structure involves collapse of the *c*-axis causes a dramatic reduction in the separation of the Fe^{2+} planes which may be expected to result in a greater magnetic exchange between the planes. What we observe from experiment is the gradual suppression of any long-range magnetic order in the system and instead we observe the emergence of another new magnetic arrangement indicated by a broad feature in the diffraction data which indicates a new form of short-range magnetic order in the HP-II phase. From simulation, the nature of this short-range order bears a degree of similarity to the ambient pressure phase of the compound, with a return to antiferromagnetic inter-planar coupling.

The observation of any form of magnetic order in the HP-II phase is strikingly in contradiction to previous published results from x-ray emission spectroscopy which report a crossover to a zero spin state coinciding with the HP-II transition and metallisation. Certainly the nature of the magnetism in this phase is different to that in the ambient compound or in HP-I. The metallic state will require that some electrons in the system be of a more itinerant nature, which will be important for any description of this new magnetism. Furthermore, possible pathways for magnetic superexchange are changed by the structural transition, and inter-planar interactions will play a greater role. The observation that the magnitude of the magnetic moment is not reduced in the HP-II phase as the sample becomes conducting suggests that this transition does not involve significant changes to the valence or electron

sharing of the Fe ions and also precludes the possibility of fractional occupancies or mixtures of high and low spin domains. The conduction then seems mostly likely to arise from the ligand species. The collapse of the c in this second structural transition reduces the separation of P ions to a length typical of a P – P bond, the formation of which will impact the valence and carrier donation from the P sites. The insulator-metal transition being due to the changes of the P ions is in agreement with recent theoretical work[91], which finds that the 3p states of the P atoms are the main contributors to the bottom of the conduction band before the band cap collapses.

The inference of a spin-crossover from x-ray emission spectroscopy results may instead be due to a number of factors related to the situation and environment of the Fe^{2+} ion across the HP-II transition. Other results already predict changes in bonding the material, and such changes to the local environment may induce changes in spectroscopic results which could account for changes which have been attributed to a spin-crossover.

The pressure-temperature magnetic phase diagram of $FePS_3$ may be greatly expanded by the measurements described here. Whist the uncertainty of T_N becomes more significant at higher pressures, a persistent increase up to the emergence of the new short-range order is clear. The phase diagram is shown in figure 4.30.

T_N in the ambient and HP-I phases increases with a gradient of $2.3(7)\,\mathrm{K\,GPa^{-1}}$. It should be noted that these transition temperatures possibly underestimate the true values by the order of 1–10 K as they are determined by the point at which a magnetic feature can no longer be resolved in the diffraction data. With the significant noise in the high pressure data, this temperature may be lower than the actual T_N. For similar reasons extrapolation from the intensity of the peak also shows significant uncertainty. Nonetheless, the increase in T_N is consistent with what is seen from magnetometry measurements under pressure up to 2 GPa, albeit with a lower rate of change. The decreased gradient of T_N with pressure compared to these magnetometry measurements may be a result of the change in inter-planar coupling which is seen as the system is pushed into the HP-I structure.

The critical temperature for the emergence of short-range magnetic order in the HP-II phase is also difficult to determine. Certainly the corresponding feature is seen in neutron diffraction measurements taken at 300 K, though with less intensity than is seen at 80 K. Estimation of the temperature at which the feature would be totally extinct is not trivial due to the complex background from the sample environment and the long time required for scans on warming, but through extrapolation of the peak fitting of those scans it is estimated to be around 360(20) K.

The persistence of the short range order up to such higher temperatures than the lower pressure magnetic orderings is indicative of much stronger magnetic interactions between

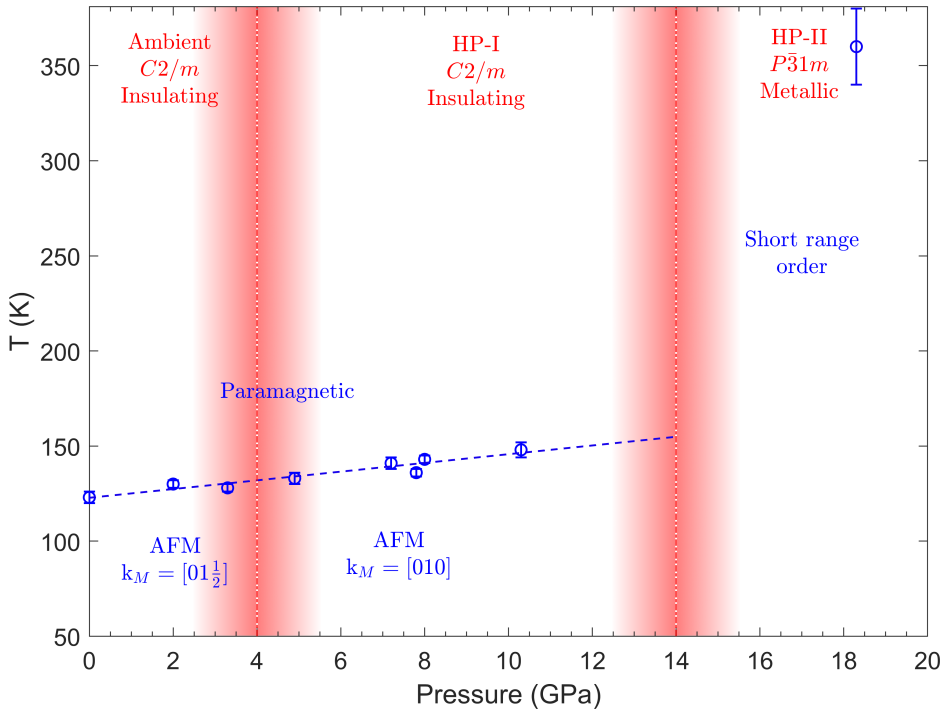

Fig. 4.30 Pressure-temperature magnetic phase diagram for $FePS_3$ with structural transitions also shown. The critical temperature for the short-range magnetic order in the HP-II phase is not directly measured and is estimated at the highest pressure by the observed temperature evolution of the magnetic scattering feature.

Fe^{2+} ions arising from the change in the crystal structure: both the reduced separation of the ions between layers and the change in the stacking of the ligands affecting superexchange pathways.

The work carried out in measuring the high pressure magnetic structure of $FePS_3$ used a double-toroidal diamond anvil cell as part of a user experiment for the first time at the ILL. The successful measurement of diffraction from the small volume of sample supports the viability of this technique for more general application in neutron scattering measurements. The experiments do illustrate several of the challenges that must be considered when using this technique: perhaps most importantly awareness of any expected diffraction peak from the diamond anvils. With the mass of the anvils far exceeding that of the sample, the impact of wavelengths which are nominally removed through the use of monochromators may be significant: as seen in this study, diamond peaks arising from $\frac{\lambda}{3}$ wavelengths are similar in intensity to relevant λ peaks from $FePS_3$ despite the orders of magnitude difference in the incident intensity of these two wavelengths. The importance of similar consideration of peaks from a separate monochromator if used is demonstrated by the earlier experiment utilising BN anvils with a Pb manometer. Secondarily, as pressure is increased and the separation of the anvils is further reduced, the neutron intensity incident on the sample is reduced as a result, which requires longer scan times. As such measurements as a function of temperature as would be valuable for this study are require prohibitively long timescales. Determination the critical temperature for the HP-II short range order would be improved by slower warming to allow measurements with greater granularity in temperature.

The asymmetry in sample peaks and the weak intensity of all but the strongest reflections due to the small sample volume further requires good knowledge of the underlying crystal structure for the determination of the magnetic structure from neutron diffraction using this technique. The further advantage of this is the capability it allows to avoid the use of a separate manometer which potentially complicates analysis.

MPS$_3$ Structures

Both powder and single crystal x-ray experiments suggest a similar pattern of structural transitions under pressure in the MPS$_3$ family for M = Fe, Ni, Mn. Across the three compounds, two distinct transitions are observed: the first of which at least is qualitatively similar across the family. This lower pressure transition to the HP-I structure maintains the shared ambient pressure $C2/m$ space group but involves a reduction of the angle β by the shearing of the weakly van der Waals coupled ab planes along the crystallographic a direction. The effect of this transitions on the inter-planar separation is minimal, following broadly what is observed for the gradual compression in the ambient pressure phase. Nonetheless,

the shearing action of the transition changes the stacking and arrangement of ions, which is sufficient to measurably change the magnetic order in $FePS_3$.

The order of the studied materials in terms of the critical pressure for the observed structural transitions is different for the HP-I and HP-II transitions, indicating that they may be influenced by different effects. That the lower pressure transitions appears similar across the family suggests that the sliding of the weakly coupled plains is favourable despite the differences in the materials' ambient pressure magnetic structures. This transition requires the highest pressure for the nickel compound, at 10 GPa compared to 2 GPa and 4 GPa for the manganese and iron. This may be due to the impact of the orientation of the magnetic moments in $NiPS_3$ being oriented predominantly along the a axis, with only a small component normal to the transition metal ion planes which is dissimilar to the other two materials in which the moments are oriented predominantly or entirely along c^*. The coupling of the moments between the van der Waals planes cannot immediately be used to explain the critical pressures for this transition: in Mn and $NiPS_3$, the planes are coupled ferromagnetically in contrast to $FePS_3$, yet the latter is in the middle in terms of the necessary pressure for the HP-I transition. The neutron studies do however show that the inter-planar magnetic coupling is flipped from anti- to ferromagnetic in $FePS_3$ across the transition, and so it will be of interest for future experiments to establish if the existing ferromagnetic coupling is retained in the other compounds.

The similarity of the sliding transition across the family exists also despite the significantly different magnetic natures of the compounds. The Ising $FePS_3$ and Heisenberg $MnPS_3$ undergo the transition at comparable pressures. Dynamics in the HP-I phases remain to be studied which may show that the sliding transitions induces a change in the magnetic interactions, which seems likely due to the changing distances between magnetic ions as well as the altered stacking of ligand ions affecting any superexhange pathways. This similarity further motivates not high-pressure magnetic studies of the other compounds as has been demonstrated for $FePS_3$, but also beginning high pressure measurements of dynamics by inelastic neutron scattering.

The effect of the second transition is similar across the family, being to reduce the separation of the can der Waals planes and where possible, single crystal x-ray results indicate an increase in symmetry to a $P\bar{3}1m$ group. In the HP-II phase, powder diffraction results indicate the inter-planar distance is minimum for $NiPS_3$ which is consistent with it having the smallest starting lattice parameters under ambient conditions. Previous DFT calculations of $FePS_3$ suggest the formation of intra-planar P-P bonds in the HP-II phase following this c-axis collapse. With the spacing in Ni and $MnPS_3$ being similar or less than in the iron compound such bond formation may also be expected in the other materials.

In both compounds in which the second transition was measured by single crystal diffraction, the extent of the c-axis collapse is reduced from that which is observed in similar experiments on powder samples. What remains to be determined is if this result is intrinsic to the sample or influenced by other details of the respective experiments. Besides the state of the samples used, which may in itself be a factor as is observed in neutron scattering experiments on $FePS_3$, there exist key differences between the experiments which may influence the observed structural transitions. In both powder studies of the iron compound reported by Haines et al. and the nickel compound reported here, observation of the c-axis collapse is made only in high-pressure studies without the use of a pressure transmitting medium. In the single crystal experiments, a helium pressure medium was used. To eliminate the possibility of interaction between the samples and the pressure medium, powder diffraction experiments with an helium medium would be necessary up to higher pressures, however the the results obtained thus far make this appear an unlikely explanation due to the strong agreement between powder data with and without medium in Ni and $MnPS_3$ up to the maximum measured pressures, as well as the structural information on $FePS_3$ which may be inferred from the high pressure neutron experiment.

The accuracy to which the c-axis could be measured in single-crystal measurements was limited by the accessible range of reciprocal space defined by the sample orientation and the opening angle of the diamond anvil cell. To allow this to be more confidently measured in future, several approached may be taken. A pressure cell with a larger opening angle may be used where possible, but for the greatest advantage the single crystal samples will need to be cut such that the c^* direction is no longer normal to the faces of the diamond anvils. This will require cleaving samples across the platelets whilst retaining enough layers to give a good scattering signal. Such an approach appears experimentally more challenging than the more natural arrangement used here but ultimately achievable. This increased access to information along the c^* direction will necessarily come at the cost of reduced observable reciprocal space along another direction.

The HP-II transition in $FePS_3$ and $FePSe_3$ is linked to either metallisation or the emergence of superconductivity respectively. Electrical transport measurements have not been performed in Ni or $MnPS_3$ to sufficient pressure to observe a direct equivalence, but lower pressure measurements follow a similar trend to that seen in $FePS_3$. The observation of these similar structural for the first time in Ni and $MnPS_3$ establishes that similar behaviour may be expected and determines the critical pressures above which future resistivity measurements will need to be performed in search for similar insulator-to-metal transitions.

Chapter 5

Magnetocaloric Properties of $EuTiO_3$

5.1 Overview of Previous Work

$EuTiO_3$ (ETO) is an antiferromagnetic dielectric in which previous work has revealed strong coupling between both the magnetic and electrical ordering and strain. These magnetoelastic and magnetoelectric effects are good indication that hydrostatic pressure is a viable tuning parameter for exploring the phase space of this material. ETO is a quantum paraelectric similar in many ways to $SrTiO_3$ and recent work by Coak et al. on that material under pressure gives further support that pressure will be a valuable method to exploring new behaviour in this similar system with the addition of magnetic order. A new area of interest in ETO has arisen due to a significant observed magnetocaloric effect of a magnitude similar to that in a number of commonly used materials for magnetic refrigeration.

Structurally, ETO is a perovskite oxide, having at room temperature a cubic crystal structure with space group $Pm\bar{3}m$ and lattice parameter $3.9082(2)$ Å[92], and being effectively isostructural with $SrTiO_3$ (STO). Similarly to STO and $CaTiO_3$, ETO undergoes a structural cubic $Pm\bar{3}m$ to tetragonal $I4/mcm$ transition on cooling attributed to antiferrodistortive tilting of the TiO_6 octahedra[93, 94]. The temperature of this first order transition in ETO has proven difficult to properly identify due to a number of complicating factors[95]. Bussman-Holder et al. in 2011 observed an anomaly in the specific heat attributed to this transition at $282(1)$ K[96]. Shortly thereafter, high-resolution synchrotron x-ray diffraction experiments performed by Allieta et al. determined a critical temperature of the transition of 235 K[93]. This disparity results from a complex evolution of the length-scale of the lower symmetry phase. At 240 K, pair distribution function analysis shows that the correlation length-scale of the tetragonal phase is $\sim$20 Å, which combined with the random orientation of the tetragonal axis throughout any crystal means that the large-scale structure of ETO appears cubic even below the structural transition.

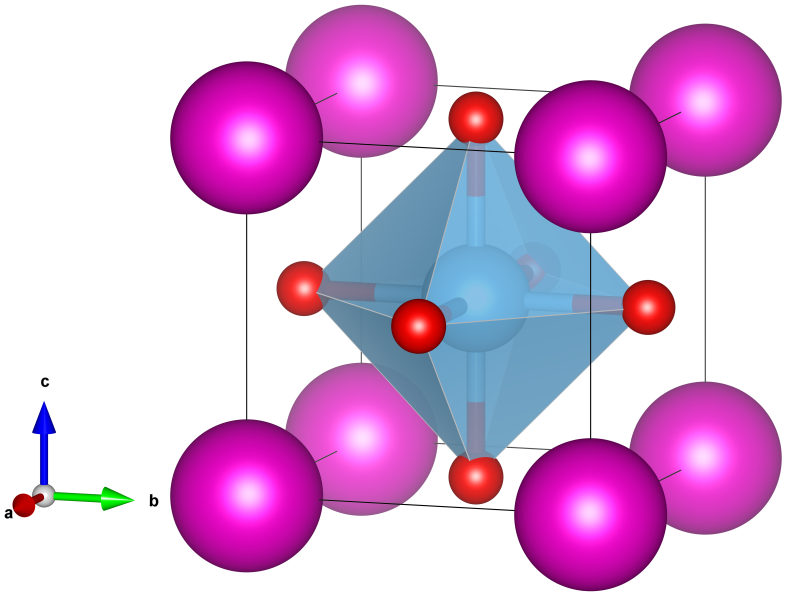

Fig. 5.1 Crystal structure of $EuTiO_3$ at 293 K and ambient pressure. Eu^{2+} ions are shown in purple, Ti^{4+} in blue and O^{2-} in red. The oxygen octahedron is shaded in blue. Made using VESTA software[48].

The dielectric properties of ETO show complex dispersive behaviour at high temperatures which transition to a well defined quantum paraelectric regime at lower temperatures. The magnetoelectric effect in the material is clearly visible from dielectric measurements in the form of a drop of 3.5 % in the real part of the dielectric constant between 2 K and T_N and an increase in the dielectric constant under the application of an external magnetic field [97, 98]. Above T_N, the dielectric constant saturates below ∼30 K to a of ∼400[99] as predicted for a quantum paraelectric material and is well fit by Barrett's formula. As a counterpart to these dielectric properties, electrical resistivity increases by five orders of magnitude on cooling from room temperature to 100 K.

Work on STO has shown that hydrostatic pressure can tune the material away from a ferroelectric quantum critical point, which is seen in an increase in the temperature of the crossover from classical high temperature paraelectric to lower temperature quantum paraelectric behaviour. Alongside this is observed the emergence of new behaviour at low temperature attributed to the coupling of the soft optical phonon associated with ferroelectricity with a transverse acoustic phonon. ETO exhibits similar dielectric behaviour linked to its quantum paraelectric state but is thought to be further from a ferroelectric quantum critical point. The addition of antiferromagnetic ordering in the compound invites further

investigation to examine how this influences the evolution of the quantum paraelectric state with pressure, as strong magnetoelastic coupling in ETO is well established..

Below 5.5 K ETO exhibits *G*-type antiferromagnetic ordering of the spins of the Eu^{2+} ions[99, 100, 101, 102]. The coexistence of (anti)ferroelectric and magnetic ordering in ABO_3 perovskite oxides is uncommon due to competing electronic requirements. Most commonly ferroelectricity arises from a d^0 state on the transition metal B ion, whereas magnetism occurs when this ion has a d^n $(n > 0)$ configuration[103]. ETO retains a $3d^0$ configuration on the B species (Ti), but has a magnetic ion (Eu^{2+} with $4f^7$ moments)[104]. These ions have a large total angular momentum: $J = S = \frac{7}{2}$ and $L = 0$[105].

Below T_N, torque magnetometry measurements performed by Petrović et al. suggest the antiferromagnetic structure is aligned with easy axis of magnetisation parallel to [001] with a first-order transition occurring at $T_{ab} = 2.75$–3 K decreasing with larger applied magnetic fields, to an easy plane of magnetisation in the *ab* plane (normal to [001])[106]. Neutron diffraction measurements performed by Scagnioli et al. however find that moments lie in the *ab* plane at all temperatures below T_N[107], which may suggest that the realignment occurs measurably only in a poled system created by, for example, cooling under applied electric field after Petrović et al.

A spin-flop transition is also reported by Petrović et al. and Shvartsman et al.[98], occurring at 5.3 K in minimal field, and under an applied field $H_{SF} = \sim 0.2$ T at 2 K. The two antiferromagnetic sub-lattices realign to a canted state being nearly perpendicular to the direction of the applied field. Under further applied field, these rotate towards the field direction until at sufficient field an effectively paramagnetic phase is realised ($H_c = 0.9$ T at 2 K).

It is noted that a single-crystal, tetragonal antiferromagnet such as ETO would be expected to exhibit this spin-flop phenomenon when the magnetic field is applied parallel to the direction of easy alignment. ETO however is seen to behave similarly for fields applied along all three orthogonal axes, which is further evidence for the existence of disordered structural domains persisting below T_N. An experimental magnetic phase diagram determined by Petrović et al. is shown in figure 5.2.

Work by Katsufuji and Tagaki[99] in 2001 demonstrated a strong coupling between the magnetic and dielectric properties of ETO. The dielectric constant is reduced by ~ 7 % under an applied magnetic field of 1.5 T due to the modification of the soft-mode phonon frequency by the Eu magnetism. As in ferroelectric $BaTiO_3$ and quantum paraelectric $CaTiO_3$ and STO, the T_{1u} phonon mode with the motion of the cation opposing that of the oxygen octahedra is responsible for the dielectric properties[108].

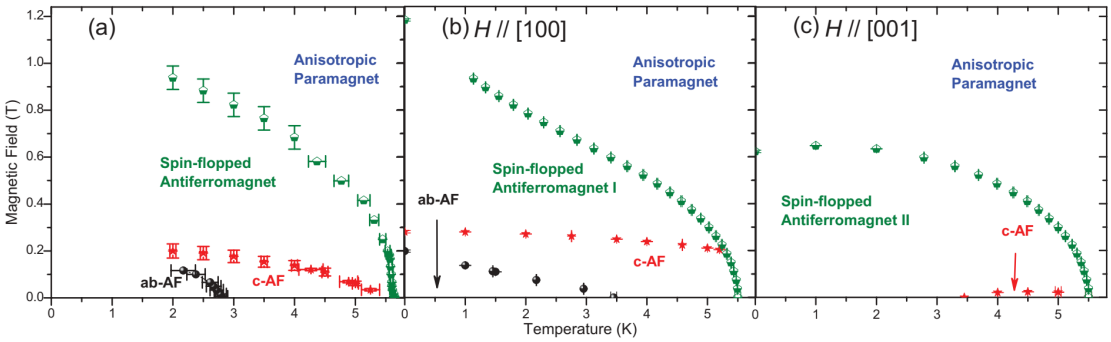

Fig. 5.2 Magnetic phase diagram of ETO determined experimentally by Petrović et al.[106]. (a) is the overall phase diagram, (b) and (c) to two sublattices with field applied along different axis in the tetragonal phase. With the random orientation of tetragonal domains at low temperatures, (a) is an effective superposition of (b) and (c).

	ΔT_{ad} (K)	$-\Delta S$ (J kg^{-1} K^{-1})	RC (J kg^{-1})
Single crystal	16.6	42.4	353
Polycrystal	16.5	40.4	300

Table 5.1 Adiabatic temperature change, isothermal magnetic entropy change and refrigeration capacity for ETO from reference [105]. All values are for demagnetising from a field of 5 T.

This coupling has been exploited to explore the potential multiferroic properties of ETO. Fennie and Rabe in 2006 predicted from density-functional[109] theory that ETO under a compressive strain $\varepsilon_s > 1.2\,\%$ would possess a spontaneous magnetisation of $\sim$7 Bohr magnetons per Eu ion alongside a spontaneous polarization of over 10 μC cm^{-2}.

Similar behaviour is experimentally realised in ETO samples grown by molecular beam epitaxy[110]. ETO thin films under epitaxial tensile strain of $\varepsilon_s = 1.1\,\%$ were measured to be simultaneously ferroelectric and ferromagnetic with ordering temperatures of approximately 250 K and 4.24 K respectively.

ETO has a significant magnetocaloric effect and its large values of both magnetic entropy change $-\Delta S_M$ and adiabatic temperature change ΔT_{ad} which compare favourably to materials commonly used for magnetic refrigeration. Midya et al. report magnetocaloric properties of both single crystal and polycrystalline samples of ETO using magnetisation and heat capacity measurements[105]. These values are given in table 5.1. These magnetocaloric properties have been explored as a function of doping with both chromium[111] and lanthanum[112], but the effect of hydrostatic pressure on the pristine sample remains to be investigated.

Recent work on STO has proven pressure to be an effective tuning parameter for dielectric properties[3, 4]. Given the similar structure and quantum paraelectric nature of STO and ETO, and previous work finding strong magnetoelastic and magnetoelectric coupling in the the latter, an investigation into the effect of pressure on both the dielectric properties of ETO as well as magnetism was carried out.

The crystal structure of ETO has been previously studied as a function of pressure and temperature up to 50 GPa from 50–500 K[113]. Increasing pressure is seen to induce an antiferrodistortive cubic-to-tetragonal transition which is the same as is observed at ambient pressure on cooling. The critical temperature of this transition is increased from its ambient pressure value linearly up to ∼500 K at 10 GPa. Such transitions are also at ambient temperatures in mixed $Eu_{1-x}Sr_xTiO_3$ in line with the octahedral tilting in both of the pure systems. The critical pressure for this transitions increases as the Sr fraction is increased, which is in agreement with the higher transition temperature at ambient pressure in pure ETO than STO due to the presence of the magnetic moments.

The evolution of the magnetism in ETO with pressure has been experimentally investigated by Guguchia et al.[114] up to 5.5 GPa in powder samples. They report a linear increase of T_N with pressure up to 1 GPa, with a superlinear dependence above this, with a maximum $T_N \approx 8.5$ K at the maximum pressure. This is fit using a Bloch power law, with the increase in T_N arising from increased overlap of the 4f orbitals with pressure. This non-linear evolution of T_N is notably different from similar systems. Alongside this is observed a reduction in the effective magnetic moment at T_N which is also non-linear in pressure.

5.1.1 Aims

This work will explore how hydrostatic pressure affects the magnetism in single crystal ETO, framing this in terms of its significant magnetocaloric properties. The effect of pressure will also be considered in relation to potential quantum criticality in the system with reference to recent work on the closely related quantum paraelectric $SrTiO_3$ and measured enhancements of the magnetocaloric properties of other materials tuned towards magnetic quantum critical points.

5.2 Preparation of Samples

Single crystal samples of ETO, previously used in studies by L. Spalek[97], were grown by S. Saxena, M. Shimuta and T. Katsufuji by a floating zone method outlined in reference [115]. This method uses the melting of a rod of the reagents Eu_2O_3, Ti and TiO_2 under

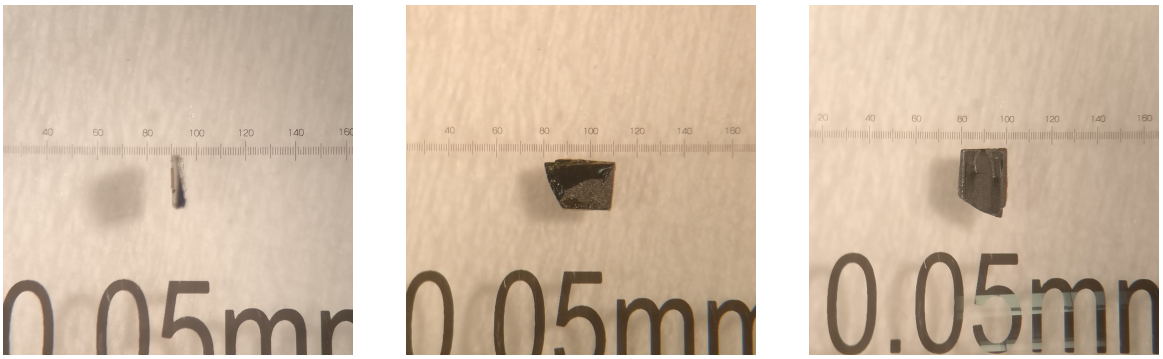

Fig. 5.3 ETO sample used for high-pressure magnetisation measurements. The sample is cut such that the <100> direction is normal to the largest face, with the orthogonal directions aligned to the other cut edges. The mass of the sample is measured to be 1.7 mg.

an Ar atmosphere. The single crystals produced by this procedure have been previously measured to have less than 1 % impurities. These ETO crystals were aligned using a Laue camera set-up at the University of Warwick, with a $\sim$1 cm^3 sample being cut with a diamond wheel saw with orthogonal faces normal to the crystallographic <001> directions under the assumption of a cubic room temperature symmetry.

From this crystal and pieces cut in its making, smaller oriented samples were cut using a wire saw system in the Cavendish in a plate geometry to allow for effective capacitance measurements to be performed as well as magnetometry.

Using the SQUID pressure cell set-up as described in 3.4.1, measurements of magnetic susceptibility were performed at cell loads of 2–6 kN corresponding to a pressure range of 0.26–1.09 GPa as determined by measurement of the superconducting transition temperature of a lead manometer in the sample space. The sample used for magnetometry measurements is shown in figure 5.3 and had a mass of 1.7 mg. Its longest axis was cut parallel to the [001] direction, with the [100] being normal to the largest cut face. The sample was of sufficient length that rotation inside the pressure cell cap was minimal.

For all magnetic measurements, the external field was applied along the longest axis of the sample. This was along the <100> direction, which upon cooling would split into the equivalent [100] and [010] and the unique direction of the tetragonal structure [001]. Measurements were performed on cooling from room to base temperature without applied field, such that there should not be a preferred direction for the unique axis due to magnetoelastic coupling[116, 117]. For each loading force, measurement of the lead superconducting transition was performed before sample measurements, at a minimal field of 10 Oe.

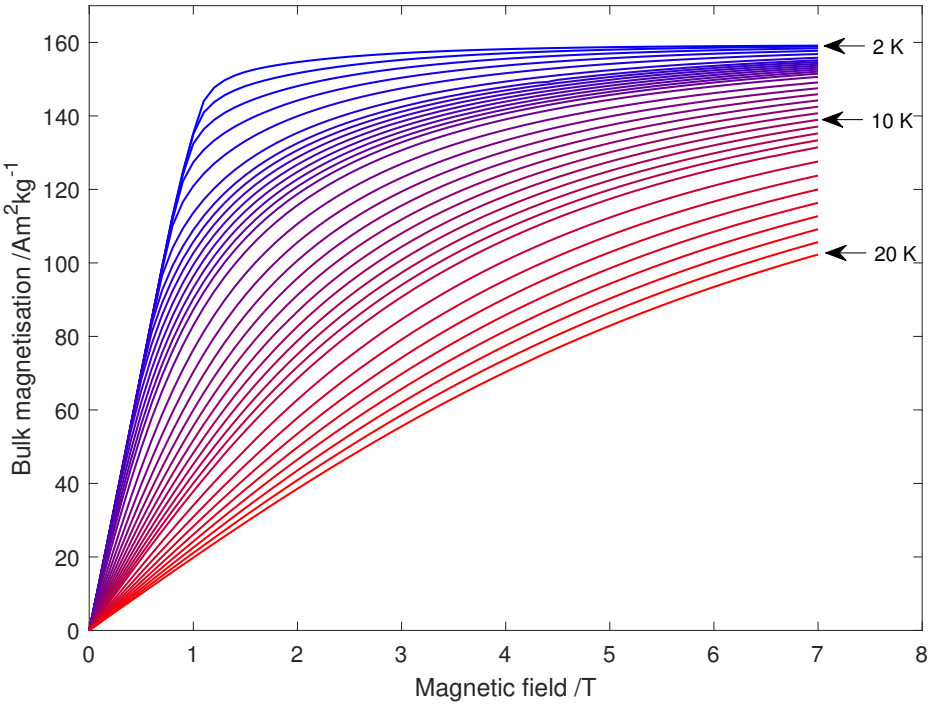

Fig. 5.4 Bulk magnetisation of ETO as a function of applied field at ambient pressure. The dense region of measurements in temperature is focused around $T_N = 5.5\,\mathrm{K}$. 2 to 5 K in 0.5 K steps, 4.8 to 6.2 K in 0.2 K steps, 6.5 to 12 K in 0.5 K steps, 13 to 20 K in 1 K steps.

Starting from 2 K and warming, sample scans were taken at field increments of 1000 Oe from 0–7 T. Between each temperature point, the magnetic field was oscillated to zero from the maximal value.

5.3 Results

Ambient pressure bulk magnetisation versus applied field over the measured temperature range is shown in figure 5.4. To each curve, a smoothing spline is fit using MATLAB and its integral up to a chosen field determined numerically using MATLAB's `integrate` function. These integrals are used with the equations in 2.4 to determine magnetic entropy change. For the measured results, the use of a trapezoidal method for integration using MATLAB's `trapz` function is seen to make a negligible difference to the calculated values.

At the lowest temperature of 2 K, bulk magnetisation begins to saturate above 1 T, reaching a maximal value of $159\,\mathrm{A\,m^2\,kg^{-1}}$ at 7 T. This can be seen in the value of mass susceptibility χ_{mass} in figure 5.5 which peaks at 0.7 T and falls rapidly with field above 0.9 T. The position of this χ_{mass} peak in field decreases with increasing temperature up to T_N, above which the maximum value of χ_{mass} is at the lowest value of applied field and

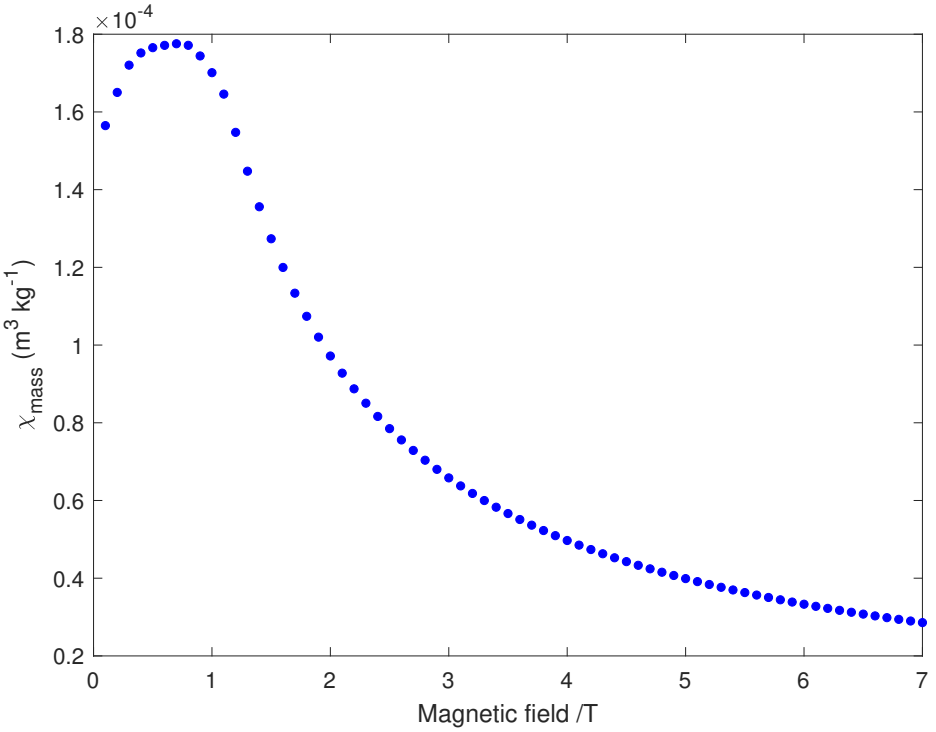

Fig. 5.5 Mass susceptibility of ETO as a function of applied field at ambient pressure and 2 K.

decreases for all higher fields, which is illustrated in figure 5.6. From the literature, this saturation of magnetisation corresponds to a change in the magnetic phase from a spin-flopped antiferromagnetic state to a field-induced ferromagnetic state at a critical field H_c. At lower temperatures, the spin-flop state is more resistant to applied field and the necessary field to suppress this and induce an effectively paramagnetic state is higher.

Above T_N, magnetisation versus applied field measurements show the paramagnetic state of ETO, not saturating up the maximum applied field of 7 T. Increasing in temperature up to the maximum measured of 20 K, the magnetisation versus field response tends closer to linearity as expected.

From magnetisation versus applied field measurements, coarse magnetisation versus temperature data may be extracted. A derived Curie plot of inverse mass susceptibility against temperature for the lowest value of applied field is shown in figure 5.7. This data shows the expected linear behaviour in the paramagnetic phase and may be fit with a Curie-Weiss law $\chi = \frac{C}{T-\theta}$ where C is the material specific Curie constant and θ is the Curie-Weiss temperature.

Least squares fitting to the ambient pressure χ_v results at 0.1 T from 6–20 K yields a Curie temperature $\theta = 3.5(1)$ K. A positive Curie-Weiss temperature is unusual for an

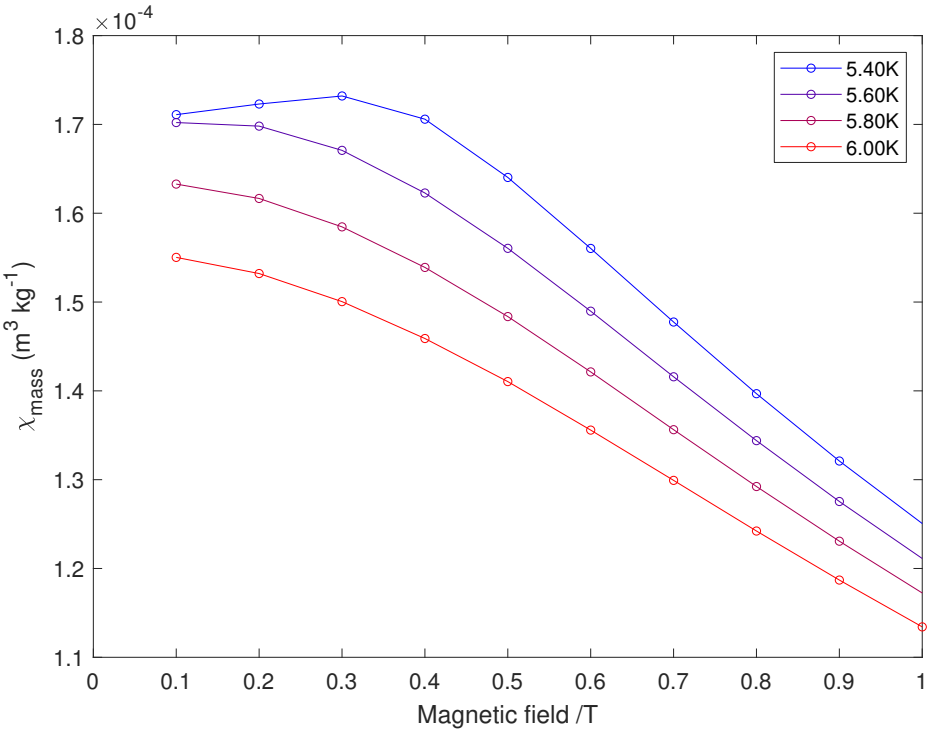

Fig. 5.6 Mass susceptibility of ETO as a function of applied field for temperatures around T_N. Only the data taken at 5.4 K which is below T_N increases above minimal field and has a peak at 0.3 T.

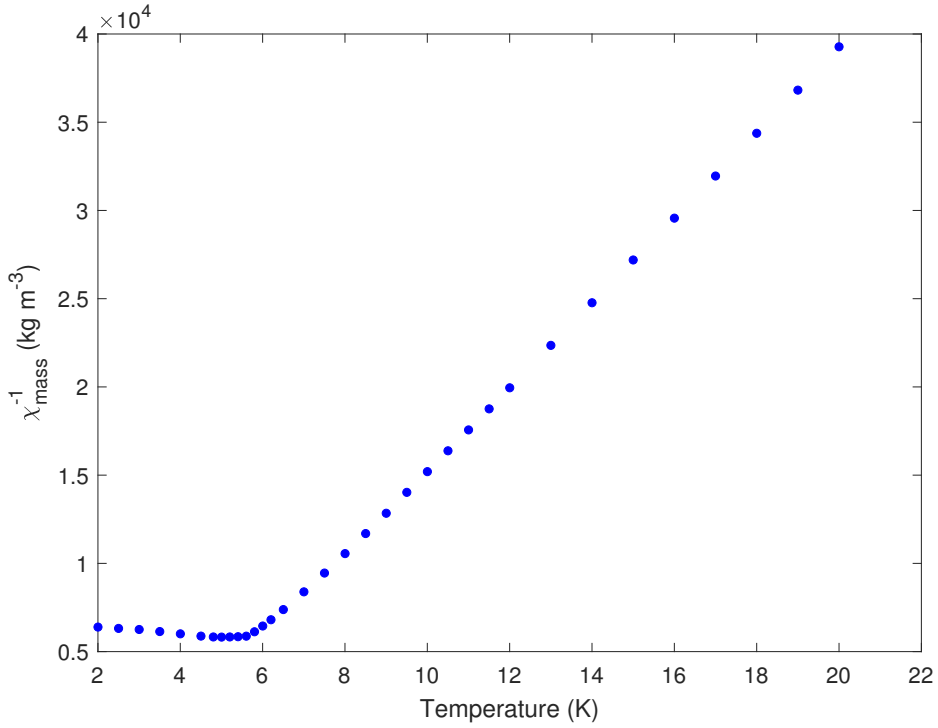

Fig. 5.7 Curie-Weiss plot of inverse mass magnetic susceptibility against temperature at ambient pressure for an applied field of 0.1 T.

antiferromagnet but is in agreement with previous results for $EuTiO_3$[99]. The Curie constant calculated using a density of $6.90\,\mathrm{g\,cm^{-3}}$ is 3.0(1). χ^{-1} deviates from linear behaviour slightly above T_N as expected due to the limitation of the mean-field approximation in the region where critical behaviour dominates.

Derived values of χ_{mass} for an applied field of 0.1 T at increasing pressures are shown in figure 5.8. From this it is apparent that the magnetic susceptibility of ETO is continually suppressed by the application of hydrostatic pressure. At ambient pressure the maximum value is $\chi_{\mathrm{mass}} = 1.718 \times 10^{-4}\,\mathrm{m^3\,kg^{-1}}$ at a temperature of 5.0 K. By the lowest applied pressure of 0.26 GPa, this is reduced to $1.609 \times 10^{-4}\,\mathrm{m^3\,kg^{-1}}$ at 5.2 K, although due to the relative sparsity of measured temperatures the true maximum likely lies somewhere in the range 5.0–5.2 K.

Increasing pressure further continues to reduce the maximal value of χ_{mass} and increase its temperature. At the maximum pressure of 1.09 GPa, $\chi^{max}_{\mathrm{mass}} = 1.220 \times 10^{-4}\,\mathrm{m^3\,kg^{-1}}$ at 5.6–5.8 K, representing a suppression of 29 % of the ambient pressure value.

T_N increases with pressure up to 6.0 K at 10.9 GPa from its ambient pressure value of 5.5 K. This would seem to correspond to a stabilisation of the antiferromagnetic state, arising

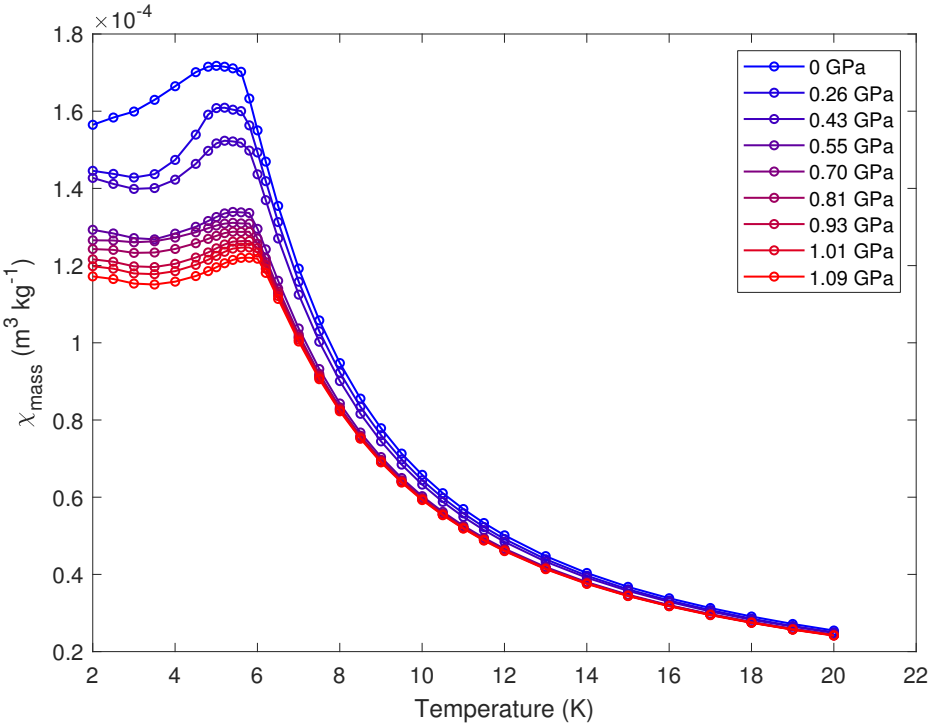

Fig. 5.8 Mass susceptibility of $EuTiO_3$ versus temperature for an applied field of 0.1 T at increasing pressure.

from increased magnetic exchange between Eu^{2+} ions due to their separation being reduced by the hydrostatic pressure and a corresponding increased overlap of the 4f orbitals.

In all pressures above ambient, there is some upturn in χ_{mass} below 3.5 K which may arise from the spin-reorientation discussed in the literature. This is most apparent in the data taken at 0.26 GPa and 0.43 GPa. As discussed for this material, even in this single crystal sample which is at these temperatures in a tetragonal structure, the alignment of the unique tetragonal axis is likely distributed randomly along the three possible <001> axes in the cubic system and so some fraction of the sample experiences the applied field H perpendicular rather than parallel to the tetragonal axis.

Another potential cause for the upturn in susceptibility at low temperature is a result of some paramegnetism of the pressure cell which is not compensated for by background subtraction. This would be consistent with the absence of this feature in the ambient pressure data.

Also apparent is the change in rate of suppression of χ_{mass} between 0.43 GPa and 0.55 GPa. The reduction of χ_{mass} between these two pressure points is greater than that observed at other points. Above 0.55 GPa, the reduction in χ_{mass}^{max} is approximately linear with a gradient of $-2.1(2) \times 10^{-5}\,\text{m}^3\,\text{kg}^{-1}\,\text{GPa}^{-1}$, as shown in figure 5.9.

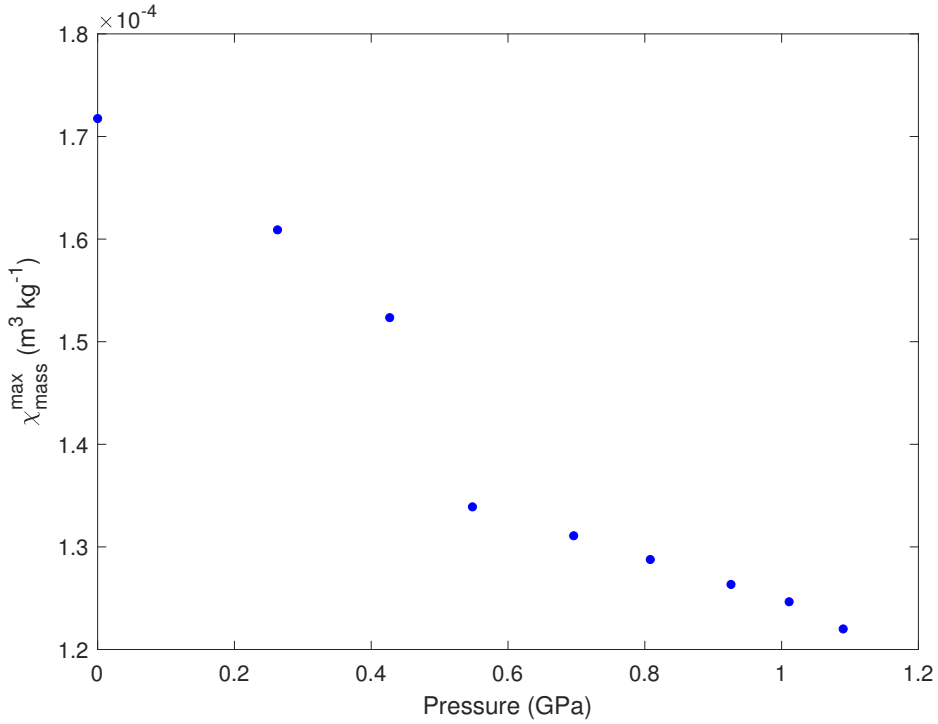

Fig. 5.9 Maximum value of the mass susceptibility as a function of pressure for an applied field of 0.1 T.

From higher pressure data at 0.1 T, Curie-Weiss temperatures may be derived as a function of pressure through fitting of χ^{-1}. Uncertainties on these values are large due to the limited temperature range of 6–20 K used for the fit, but it is seen that θ is reduced by increasing pressure as shown in figure 5.10 whilst remaining positive over the full range. As with other magnetic properties, the rate of change with pressure is discontinuous around 0.5 GPa.

The crossover from a spin-flopped antiferromagnetic phase is seen most clearly at 2 K. As can be seen from figure 5.11, the field required to induce this crossover, H_c is increased as a function of pressure. In this study the steps in field are too coarse to see the lower field crossover from the zero-field antiferromagnetic ordering to the spin-flop phase. H_c decreases with increasing temperature in the at all pressures as expected, being reduced to zero at T_N as required. Alongside the observed increase in T_N, this suggests a stabilisation of the spin-flopped and antiferromagnetic phase, persisting both higher in temperature and in field than it does at ambient pressure.

Magnetocaloric Properties

The ambient pressure negative magnetic entropy change, $-\Delta S_M$ of ETO as function of temperature for a range of field changes $\mu_0 \Delta H = 1$–7 T is shown in figure 5.12. The

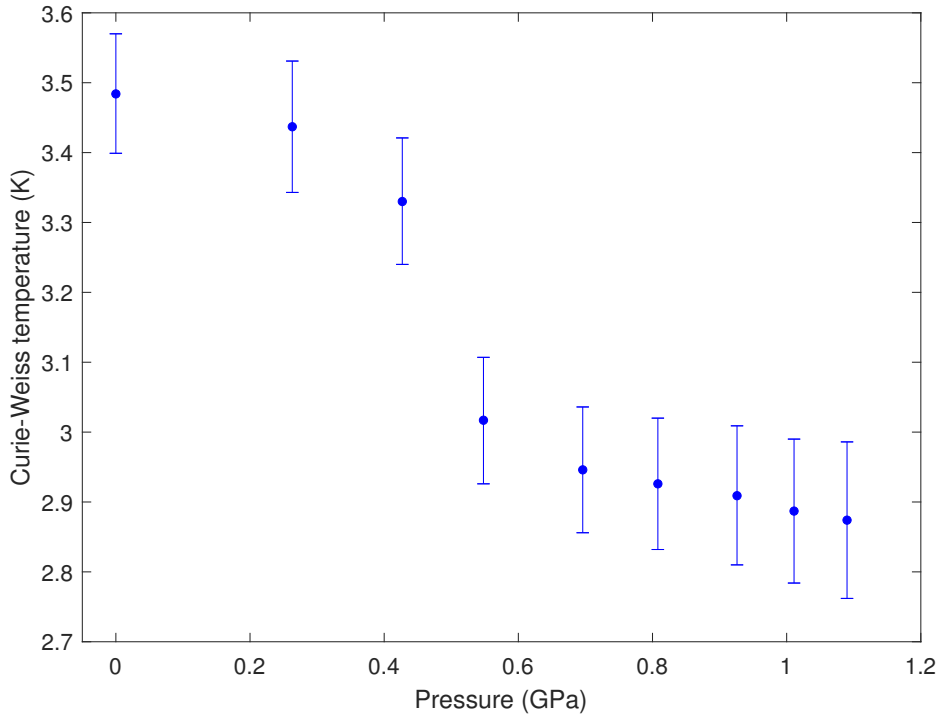

Fig. 5.10 Curie-Weiss temperature, θ, as a function of pressure from fitting of the linear paramagnetic region of χ^{-1}.

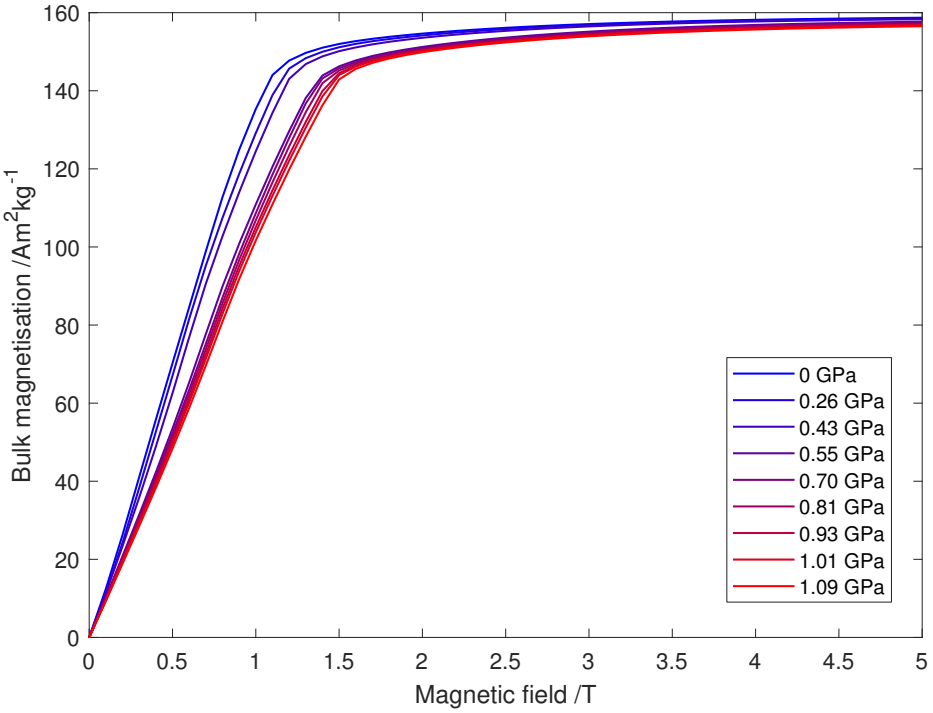

Fig. 5.11 Bulk magnetisation as a function of applied field and pressure at a temperature of 2 K.

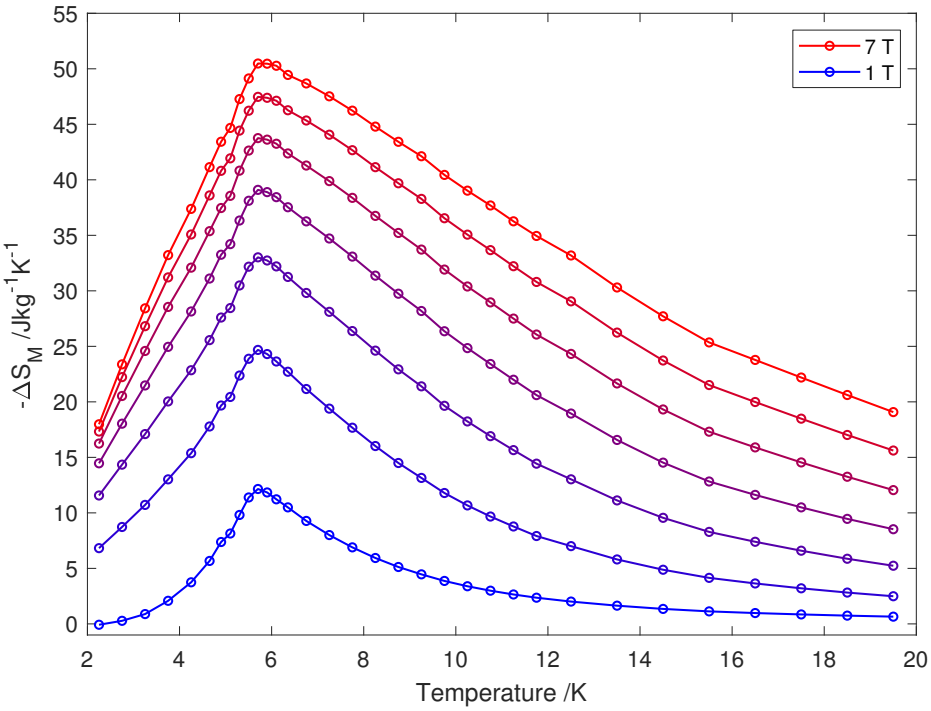

Fig. 5.12 Negative magnetic entropy change as a function of temperature for a range of field changes 1–7 T $\rightarrow$ 0 T at ambient pressure.

maximum calculated value for $\mu_0\Delta H = 5\,\mathrm{T}$ is $43.8\,\mathrm{J\,kg^{-1}\,K^{-1}}$ at 5.7 K. This is in reasonable agreement with the value of $42.4\,\mathrm{J\,kg^{-1}\,K^{-1}}$ reported by Midya et al.[105] from a single crystal sample of the same material and field change.

As expected from a material undergoing a paramagnetic to antiferromagnetic transition the magnitude of the entropy change is seen to peak at a temperature close to the Néel temperature in the paramagnetic phase. This peak value is larger for higher values of $\mu_0\Delta H$ and the rate of change of this value is greatest at lower values of field change. The temperature of the maximum in $-\Delta S_M$ is independent of the field change at 5.7 K. Below T_N, down to 2 K, ΔS_M is close to linear for fields above 1–2 T. After reference [105], this is likely due to the transition from a spin-flopped antiferromagnetic phase to a field-induced ferromagnetic phase above $\sim$1 T.

A general suppression of ΔS_M is observed with increasing pressure as well as an increase in the temperature of the maximum. This is shown for $\mu_0\Delta H = 5\,\mathrm{T}$ in figure 5.13. In agreement with inferred magnetisation versus temperature results, increased pressure increases the temperature of the maximum in $-\Delta S_M$ which implies an increase in T_N. The maximum magnitude of ΔS_M is also reduced by $\sim$7 % by 10.9 GPa, suggesting a reduction in the maximum magnetocaloric temperature change which can be extracted from the material.

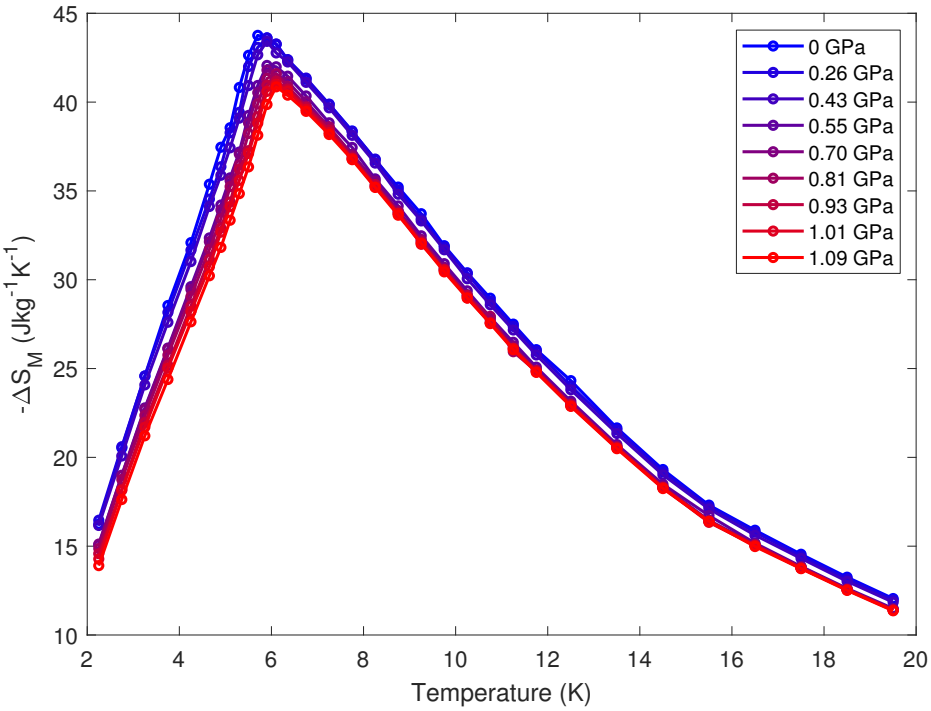

Fig. 5.13 Negative magnetic entropy change as a function of temperature and pressure for a field change $5 \rightarrow 0\,\mathrm{T}$.

The change in ΔS_M gives further evidence for the existence of some significant change occurring between the measured pressures of 0.43 GPa and 0.55 GPa. $-\Delta S_M^{max}$ is reduced by $0.34\,\mathrm{J\,kg^{-1}\,K^{-1}}$ from ambient pressure to 0.43 GPa, then by $1.36\,\mathrm{J\,kg^{-1}\,K^{-1}}$ from 0.43 GPa to 0.55 GPa and finally from that pressure up to the maximum 1.09 GPa by only $1.20\,\mathrm{J\,kg^{-1}\,K^{-1}}$.

As can be inferred from the lower gradients of bulk magnetisation vs applied field seen in figure 5.11, the relative effect of pressure on the change in $-\Delta S$ is greatest for lower values of $\mu_0 \Delta H$, below the crossover to the induced paramagnetic state. Figure 5.14 shows that demagnetising from a field of 1 T, the maximum magnetic entropy change is reduced by a third between ambient pressure and the maximum.

This greater change in ΔS reinforces the notion that the relative effect of pressure on the susceptibility of ETO is greatest at lower values of the applied field. Again from figure 5.11, we see that whilst some small suppression of the magnetisation is observed above the spin-flop to paramagnetic transition, the relative change is much smaller than that for fields below the crossover. From this we can say that the impact on magnetic exchange interactions is most important for the antiferromagnetic phases in ETO, though most of the observed points here are in the spin-flopped rather than the zero field structure.

Demonstrated in figure 5.14, when normalised to their maximum values, the gradient of $-\Delta S$ in temperature is steeper below T_N with applied pressure, giving a near-flat linear

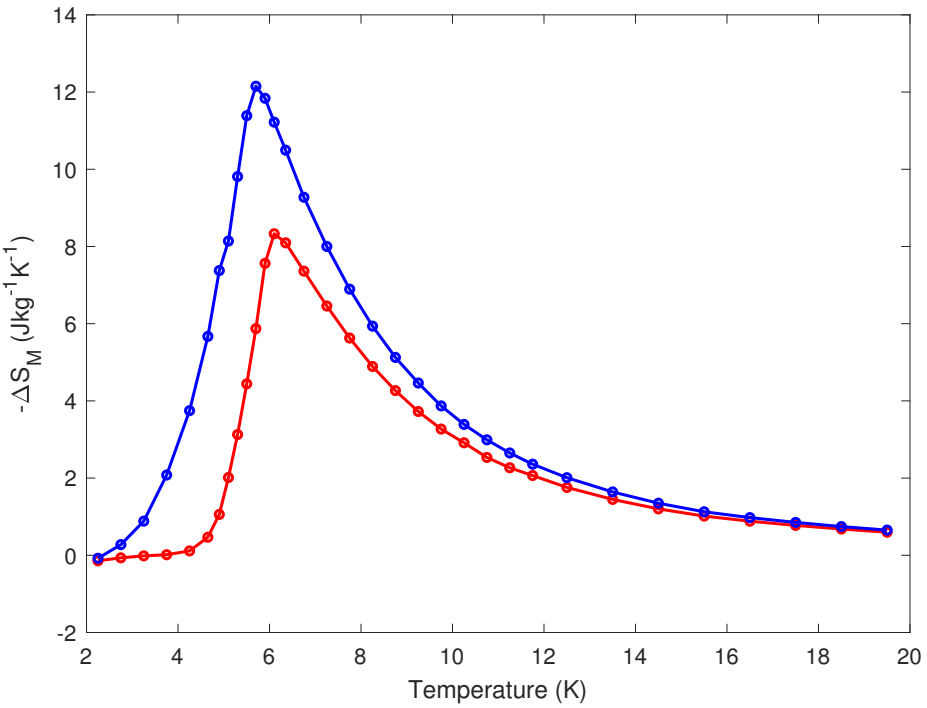

Fig. 5.14 Negative magnetic entropy change as a function of temperature when demagnetising from an applied field of 1 T. Ambient pressure data is shown in blue, and that at 1.09 GPa in red.

region at the lowest temperatures. As result the useful temperature range over which a magnetocaloric effect may be exploited is reduced by increasing pressure.

This effect only apparent at lower values of $\mu_0\Delta H$, and for applied fields greater than 3 T the normalised behaviour of $-\Delta S$ below T_N is identical across the range of applied pressures.

5.4 Discussion

Hydrostatic pressure up to 1 GPa has been shown to have a consistent effect of the magnetism of $EuTiO_3$ and hence its magnetocaloric properties. Foremost, the magnetic susceptibility of the system both above and below its Néel temperature is continuously reduced. Alongside this, the Curie Weiss temperature taken from fits to the inverse susceptibility in the paramagnetic phase is also reduced from its positive ambient pressure value.

The fact that the rate of change of both of these magnetic properties of the system changes discontinuously around 0.5 GPa suggests that there is some physical change in the system at this pressure which is not simply a gradual compression of the unit cell as would seem to fit the steady suppression seen away from this pressure point. Whilst pressure is reported to induce structural transitions in this material[113], in the temperature range of this study the system is expected to be the tetragonal $I4/mcm$ phase, being below the transition temperature from the cubic $Pm\bar{3}m$ structure. Pressure is only reported to increase this transition temperature.

It should be noted however that this previous study used a minimum pressure of $\sim$1.1 GPa and only down to the lowest temperature of 50 K. At the lower temperatures studied here where magnetic interactions are relevant the occurrence of other structural changes under pressure cannot be excluded.

The results found here are initially consistent with the work of Guguchia et al.[114]. As reported by that group, from ambient up to 1 GPa, T_N is seen to increase up to 5.8 K. This linear increase with pressure is consistent with results found in other perovskites and is generally attributed to increasing overlap of the 4f orbitals with pressure which stabilises the antiferromagnetic order. This study also observes a non-linear decrease of the magnetic moments at T_N but does not make specific comment on the specific decrease at 0.5 GPa. This previous study was carried out on powder samples of ETO using similar pressure apparatus as this work. Differences between powder and single crystal samples is interesting due to the presence of microdomains of tetragonal orientation in the single crystal samples.

From calculated magnetocaloric results, it seems that the effect of pressure is most significant at low values of the applied magnetic field. The greatest changes are seen for values of $\mu_0\Delta H$ less than approximately 1 T, which suggests that it is the (spin-flopped)

antiferromagnetic phase which is most susceptible to alterations of its magnetic properties by pressure. The field-induced paramagnetic state below T_N appears largely unchanged.

The apparent suppression of bulk magnetisation corresponds directly to a reduction of the magnetic entropy change which can be extracted from the system and the magnetocaloric effect. Still the ambient pressure results confirm results that ETO's properties are favourable in comparison to a number of commonly used magnetocalorics. Over the range of field changes 1–7 T, the magnetic entropy change is consistently larger than that which can be achieved from $Gd_3Ga_5O_{12}$, Eu_3O_4 or $EuHo_2O_4$.

With respect to future investigations into the coupling of quantum critical effects in magnetic and electrical ordering within a single system, these results suggest that ETO is not a system in which this can be easily explored using a single tuning parameter. Whilst the effects of pressure on the material's dielectric properties remain to be investigated, the increase in T_N with pressure is contrary to what is seen in conductive antiferromagnetic materials such as $CeIn_3$. Such a reduction in T_N to force ETO towards a magnetic quantum critical point is not however ruled out for the case of other tuning parameters such as electric fields or chemical substitution. This may represent an alternative to the theoretical approach to potential multiferroic quantum criticality in ETO discussed in reference [118], which suggests that the critical temperatures for both magnetic and dipole ordering in ETO may be simultaneously tuned by alloying with both Ba and Sr to a theoretical quantum bicritical point at a composition of $Eu_{0.3}Ba_{0.1}Sr_{0.6}TiO_3$.

Such an alternative approach to accessing at least a magnetic quantum critical point will be necessary to explore the potential enhancement of these reported magnetocaloric properties due to critical effects as discussed by Wolf et al.[11, 12]. The favourable magnetocaloric properties possessed by ETO at ambient conditions would suggest that any potential enhancement accessible by tuning towards a quantum critical point would make it a very favourable choice for magnetic refrigeration, outside of the initial difficulty in reaching this point.

Chapter 6

Conclusions

6.1 MPS$_3$ Outlook

Through record high pressure experiments, the magnetic phase diagram of $FePS_3$ has been expanded above its previously measured structural transitions. This has revealed that the two structural transitions are both accompanied by coincident changes in the magnetic structure: alongside the sliding transition to the HP-I crystal structure, an antiferromagnetic structure is retained, but with the Fe^{2+} planes being ferromagnetically coupled instead of antiferromagnetically; alongside the increase in symmetry and collapse of the c axis at higher pressures, the loss of long range magnetic order and the emergence of a newly observed short range order being qualitatively similar to the ambient pressure structure.

These results present several opportunities for further study in this area. The observation of short range magnetic order in the metallic phase being counter to expectations from published x-ray emission spectroscopy results raises the question of potential magnetic order in the related high-pressure superconductor $FePSe_3$. The critical pressure for superconductivity in this material is reported as 9 GPa, which using the double-toroidal diamond anvil cell apparatus described in this work has been shown to be achievable for neutron diffraction studies.

$FePSe_3$ is, at ambient conditions, antiferromagnetic below $T_N = 119\,\mathrm{K}$, with a magnetic propagation vector $\mathbf{k}_M = \left[\frac{1}{2}0\frac{1}{2}\right]$ [119], corresponding to ferromagnetic chains along the b direction being antiferromagnetically coupled to their neighbours along a and c, with moments oriented parallel to the c direction. This should be readily measurable on the D20 beamline as was done for $FePS_3$. A c-axis collapse is also reported in this material much like the MPS$_3$ materials reported here which coincides in pressure with the superconductivity. If a spin-crossover to a spin zero state is not observed alongside the emergence of superconductivity, this will have significant consequences for the nature of the superconducting state. With its

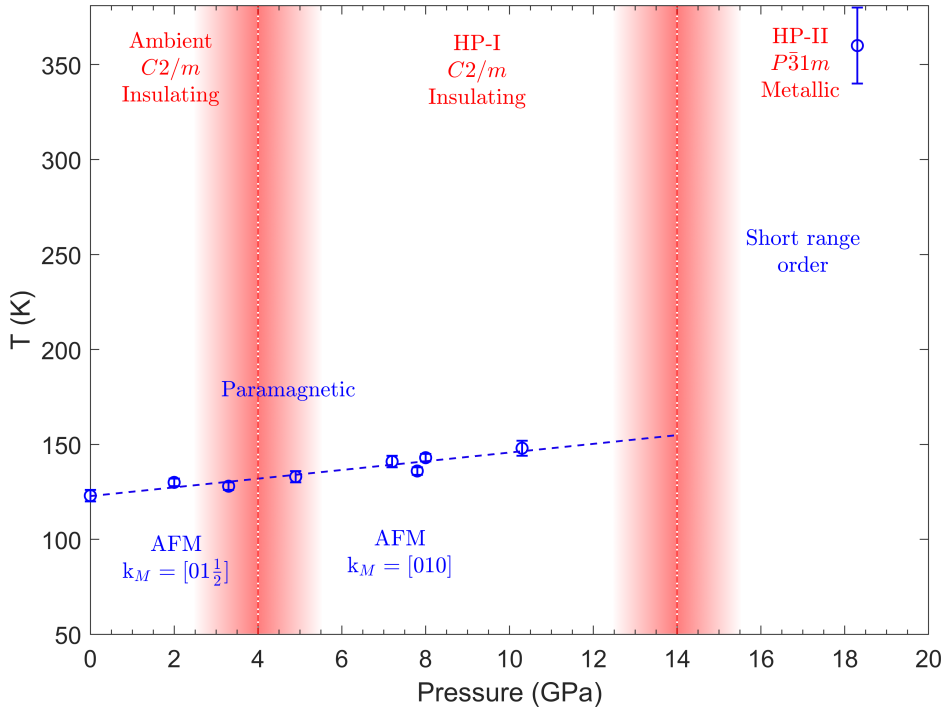

Fig. 6.1 Structural, magnetic and electrical phase diagram of $FePS_3$. Magnetic phases and the Néel temperature are shown in blue, with structural transitions and phases in red. Shaded regions denote pressure regions in which the adjacent structural phases coexist in powder diffraction patterns.

noted similarities to the selenium compound, future work to explore the possibility of similar superconductivity in $FePS_3$ may also be performed. With the metallisation and emergence of superconductivity in $FePSe_3$ coming at approximately 8 GPa and 9 GPa respectively, further transport measurements of $FePS_3$ should be performed although superconductivity is not currently reported up to 40 GPa down to at least 2 K. Measurements over this pressure range at lower base temperatures may likely be necessary. With the persistence of magnetism into the metallic phase, the next step for understanding superconductivity in this class of system will be the observation of how it responds as superconductivity is approached.

Within the family, it will be of interest to effectively complete the series of measurements begun here. With the qualitative similarity of the structural transitions in Fe, Ni and $MnPS_3$, it is desirable that the neutron diffraction experiment performed on the iron compound be replicated on the other two members. Reaching HP-I in both $NiPS_3$ and $MnPS_3$ is again achievable using standard pressure apparatus and will allow us to examine if there is a change in inter-planar coupling as has been found for $FePS_3$. With both Ni and $MnPS_3$ having ferromagnetic inter-planar coupling under ambient conditions unlike $FePS_3$, a difference in behaviour may be expected. Further motivation for this work is found in the contrast

between Ising magnetism in FePS$_3$ compared to the Heisenberg Hamiltonian appropriate for the other compounds. This difference is significant given the near two-dimensional nature of the materials, and further study of this family presents a good opportunity to study how these different models evolve when tuned between two and three dimensions.

Further development of high pressure apparatus will be necessary to perform neutron scattering experiments exploring the HP-II phases of NiPS$_3$ and MnPS$_3$ above 26 GPa and 28 GPa. With the knowledge of the high pressure structures that has been found, searching for the occurrence of similar short range magnetic order as in FePS$_3$ emerging from dissimilar starting magnetic structures will be valuable to determine the microscopic origin of this new order.

This work is further evidence for the applicability and utility of double-toroidal anvils for use with Paris-Edinburgh presses at neutron scattering facilities, and particularly for use outside of those specific communities involved in their development. The next step for application to further this work will be the adaptation of this type of high-pressure apparatus to inelastic scattering experiments. This will necessarily require continued cooperation with researching designing and constructing these cells, as well as with sample environment teams and the scientists responsible for specific beamlines at scattering facilities.

The apparent dissimilarity of the HP-II phases of Fe and NiPS$_3$ from powder and single-crystal x-ray results also remains to be reconciled. The results from single crystal data themselves require further refinement to give full structural models including such details as the atomic positions, rather than just the overall space group. The challenge of this remains successfully integrating the diffraction data in the presence of significant background from the cell and smearing of sample peaks from stacking faults. If disparity is still observed, most notably in the identification of the $(001)/(100)$, future experiments using more closely aligned sample parameters (including pressure medium etc.) may be necessary to isolate the cause of the change in the observed transition between powder and single MPS$_3$ samples.

In the ambient pressure phase of FePS$_3$, a change in the lattice parameters is observed on cooling through T_N, below which b begins to increase with decreasing temperature. Through the addition of temperature control to the x-ray diffraction experiments which have been reported here, it should be possible to see if this magnetoelastic effect persists into the higher pressure magnetic phases in the compound. The observed change in interplanar coupling into the HP-I phase may have an effect, and the higher symmetry structure of HP-II remains to be measured by x-ray diffraction down to below T_N to observe if the effect persists outside of the monoclinic phases.

6.2 ETO Outlook

It has been shown that pressure measurably suppresses the magnetic susceptibility and magnetocaloric entropy change of single crystal ETO whilst increasing the antiferromagnetic T_N. It has been well established by previous work that the material exhibits significant magnetoelastic and magnetoelectric coupling, and that through epitaxial strain, a multiferroic state be induced. The natural extension of this is the pursuit of similar phenomena in a bulk, rather than thin film, sample.

The growth of new, high quality, single crystal ETO samples should allow for the systematic measurement of its dielectric properties under pressure, allowing for a temperature-pressure phase diagram of its quantum paraelectric phase to be mapped. From this point, the use of multiple simultaneous tuning parameters may be explored. Dielectric measurements under the under the application of pressure and magnetic field should be achievable to explore new regions in the phase space of the coupled electric and magnetic order parameters. Theoretical predictions of the behaviour of coupled order parameters as a quantum bicritical point is approached[120] may begin to be explored in this way, if not in ETO, then using it model system for development of methods using simultaneous tuning parameters. Within ETO itself, magnetic and electric quantum critical points may be approached through other tuning parameters including chemical substitution. Through this methods it may be possible to investigate the enhancement of magnetocaloric properties due to quantum critical effects. This would be a valuable expansion of previous work in this field which shows enhancement in low-dimensional magnetic systems, and three-dimensional materials with xy ordering. Substituted ETO may allow not only the exploration of this in a more complex three-dimensional magnetic system, but also to examine a similar effect is observed near a electric quantum critical point in a material with strong magnetoelastic coupling.

Through the use of other tuning parameters including external electric field, more work will be possible also on exploring the effect of the tetragonal microdomains at low temperatures. Previous work has shown that the cubic to tetragonal transition may be polled by cooling under an applied field to eliminate a possible direction for the tetragonal axis, attaining something closer to a monodomain sample. This should yield enhancement of magnetic susceptibility and magnetocaloric properties as a greater fraction of the sample will experience field along the direction of easy polarisation. Based on the established magneto-electric coupling in the material, an effect on the dielectric properties is also expected. This will remove certain effects at low temperatures, such as the spin flop being seen with field applied along each of the orthogonal axes.

Further work may be performed to explore the observed discontinuity in the rate of change of magnetic susceptibility and related properties around 0.5 GPa. Detailed x-ray

experiments are reasonable to perform over this pressure range, and would provide a good baseline of understanding to identify the origin of these effects.

The successful determination of magnetocaloric properties under pressure demonstrated here further show that as well as the exploration of new materials for use in refrigeration, the use of pressure as a tuning parameter in materials which have previously shown use in this are may be useful for modifying both the magnitude as well as the peak temperature of the observed magnetocaloric effect. In this way the design of new materials through substitution etc. may be informed by how pressure affects existing systems of a similar type.

Chapter 7

Search for superconductivity in the MPS$_3$ and MPSe$_3$ systems

The observation of superconductivity in $FePSe_3$ but not yet in the similar $FePS_3$ presents a number of interesting questions.

Through comparison of the data shown in figures 7.1, 7.2 and 7.3, it is apparent that at least in these studies, the residual resistance ratio (RRR) is significantly higher in the measured superconducting $FePSe_3$. In the best case for the bridgman series of measurements for $FePS_3$ this value is less than 2, or $\sim$5 for more recent diamond anvil cell measurements, whereas in $FePSe_3$ it may be extrapolated to 15–20. The implication of this is that the samples of the selenium compound are much cleaner in terms of impurities, imperfections and other sources of scattering. Using the approximate sample dimension measurements in reference [66], low-temperature resistivity above the superconducting transitions in the selenium compound may be very approximately estimated to be on the order of 1–20 $\mu\Omega$cm. This remains significantly lower than that found in the similar studies of $FePS_3$ discussed here.

The implication of these higher values of low-temperature resistance and lower RRR in the sulphur compound is that the observation of superconductivity in this material remains unlikely unless a point in the phase diagram is reached where the critical temperature for such a transition is much higher than that of the selenium material. If the transition is expected to be largely similar between the two materials, the electron mean free path in $FePS_3$ is likely too low in comparison to any expected superconducting correlation length for the transition to occur. This must be addressed by the production of higher quality samples of $FePS_3$ and the removal of other obstacles arising from measurement techniques (a step which is already visible by comparison of M. Coak's data from Bridgman anvils versus diamond anvil cell measurements.)

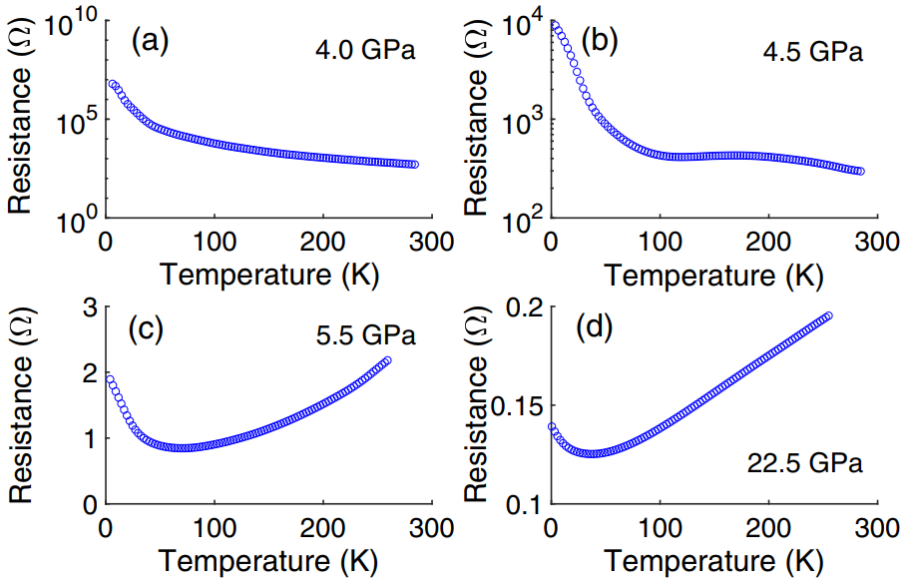

Fig. 7.1 Resistance measurements of $FePS_3$ from references [3] and [60]. High pressure measurements were performed using a Bridgman anvil cell set up.

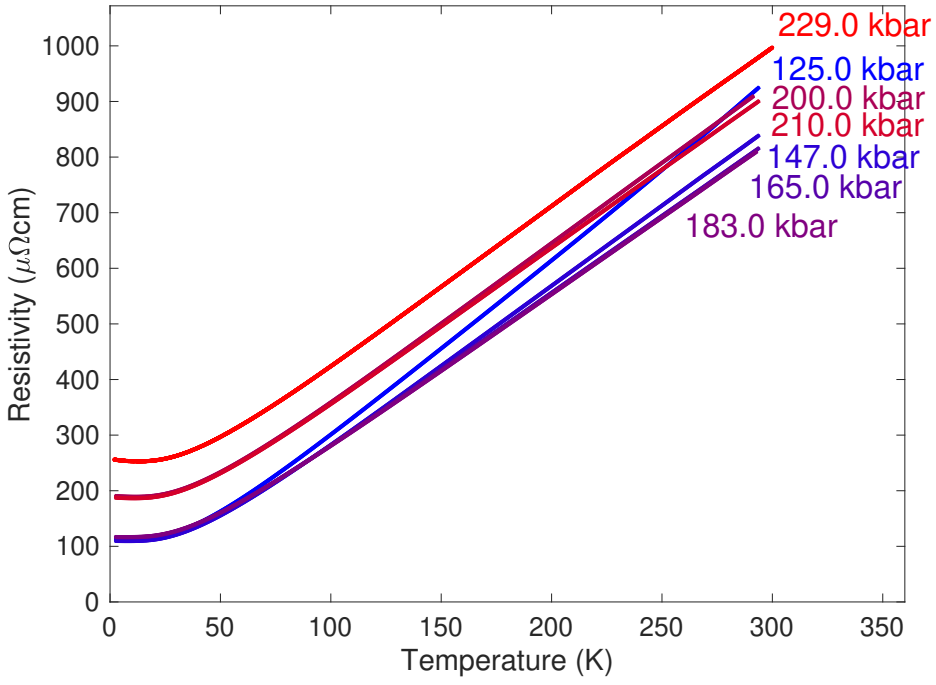

Fig. 7.2 Further recent resistivity measurements of $FePS_3$ provided by M. Coak. Measurements are taken in a diamond anvil cell, rather than a Bridgman anvil cell.

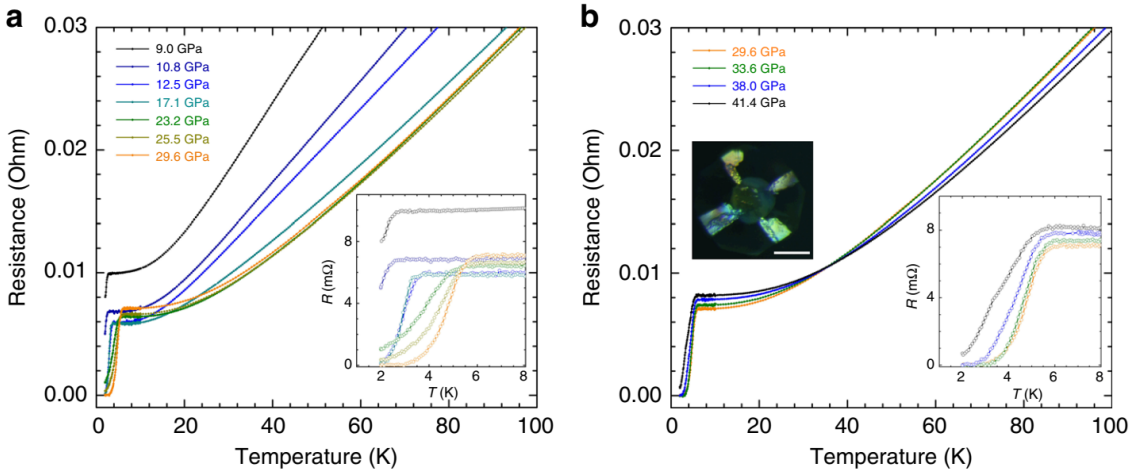

Fig. 7.3 Resistance measurements of $FePSe_3$ from reference [66]. A superconducting transition is observed above pressures of 9 GPa, again achieved using a diamond anvil cell.

At the level of detail available, the growth processes for the two compounds are largely similar, and so differences in the quality of the final product must arise from details of growth but also perhaps from the selection of samples used for measurement: the requirements for electronic studies are different to those for x-ray or neutron diffraction and this must be considered. A closer examination of the comparative growth methods used for previous studies of $FePS_3$ and $FePSe_3$ will be useful for any future investigations into superconductivity in the former. If necessary, greater cooperation between groups may be advantageous, including with the group of Je-Guen Park at Seoul National University which has many successful studies on compounds of this type, or as an alternative beginning new cooperation with other established crystal growth groups such as that of Satoru Nakatsuji at the University of Tokyo.

Outside of the quality of samples themselves, difficulty has previously been encountered in resistivity measurements of MPS_3 compounds in making good electrical contacts to the pristine faces of the samples. This issue is two-fold in high pressure experiments: making contacts structurally sufficient to remain attached inside the pressure region of anvil cells, and making the contact resistance low enough that is does not interfere prohibitively with the intended measurements. Progress is already seen in the differences between bridgman and diamond anvil cell studies. Previously DAC experiments on $FePS_3$ have been performed using sputtering to deposit layers of nickel-chrome and then silver onto the sample in the requisite geometry for a four-point resistivity measurement. To these, gold wire was attached using a silver epoxy. This process was seen to reduce contact resistances by a factor of ten at low temperatures, when compared to wires epoxied directly to the sample surface.

It is desirable, then, to explore methods utilising contactless methods of measurement to circumvent these issues. Such applicable techniques are high-pressure measurement of AC susceptibility in diamond cells as outlined by P. Alireza in reference [121] which have had great success in the observation of such superconducting transitions. Related work by Y. T. C. Ko[122] and others in using contactless techniques with extreme sensitivity will also be invaluable for this search and should help avoid several of the issues causing difficulty in direct resistivity measurements. Similarly, this will help to motivate the use of new techniques to the groups involved, for instance the use of nitrogen-vacancy (NV) centres in diamond anvils themselves to act as extremely sensitive probes for strain and magnetic field, as has been demonstrated in recent work including that focused on superconductivity[123, 124].

The search for superconductivity in FePS$_3$ and related compounds will continue to be aided not only by the calculation of high-pressure crystal structures, but by band structure calculations utilising these results. For this to be successful, certain details will need to be carefully considered. For example, the persistence of some form of magnetic order in the metallic phase of FePS$_3$ which is reported here may impact the band contributions arising from the Fe ions. Improving the chances of success of such calculations is a major motivation for the continuation of work detailed here to accurately determine these highest pressure crystal structures: resolution of the disparity in results of the inter-layer spacing in FePS$_3$ will be essential next step. Work on such calculations is currently underway in the group of S. Saxena into both high pressure crystal structures and band structures of these metallic phases and will continue to be a vital tool.

Another potential avenue for continued research into superconductivity of this type will be into hybridised S/Se systems. Examples which motivate this are not only the superconductivity in FePSe$_3$, but the metallic behaviour of VPSe$_3$, in contrast to the insulating VPS$_3$ (which itself is driven through an insulator-to-metal transition by pressure). It will be great interest to see, for example, if the same insulator-metal transition may be induced by doping. With existing concerns around the growth of good quality samples, and the added complexity in the need for controlled doping ratios, even greater care will need to be taken in the growth of such hybrid materials, though this may addressed with many of the same considerations as noted for production of the pure S or Se materials.

As a final note, it is worthwhile to re-emphasise the value of this future work. Several classes of materials which demonstrate unconventional and high-temperature superconductivity such as the cuprates and pnictides attract a great deal of interest and remain to be well understood. Superconductivity as it exists in the MPX_3 materials provides an alternative mechanism to be explored, compared and contrasted to these other systems to continue to develop our understanding of such emergent effects as a whole.

References

1. Saxena, S. S. *et al.* Superconductivity on the border of itinerant-electron ferromagnetism in UGe_2. *Nature* **406,** 587–592 (2000).
2. Grosche, F. M. *et al.* Superconductivity on the threshold of magnetism in $CePd_2Si_2$ and $CeIn_3$. *Journal of Physics: Condensed Matter* **13,** 2845–2860 (2001).
3. Coak, M. J. *Quantum Tuning and Emergent Phases in Charge and Spin Ordered Materials* Ph.D. Thesis (University of Cambridge, 2017).
4. Coak, M. J. *et al. Emergence of a Quantum Coherent State at the Border of Ferroelectricity* arXiv: 1808.02428 `[cond-mat]`.
5. Coak, M. J. *et al.* Dielectric Response of Quantum Critical Ferroelectric as a Function of Pressure. *Scientific Reports* **8,** 14936 (2018).
6. Monthoux, P. & Lonzarich, G. G. P-Wave and d-Wave Superconductivity in Quasi-Two-Dimensional Metals. *Physical Review B* **59,** 14598–14605 (1999).
7. Monthoux, P. & Lonzarich, G. G. Magnetically Mediated Superconductivity in Quasi-Two and Three Dimensions. *Physical Review B* **63,** 054529 (2001).
8. Monthoux, P. & Lonzarich, G. G. Magnetically Mediated Superconductivity: Crossover from Cubic to Tetragonal Lattice. *Physical Review B* **66,** 224504 (2002).
9. Monthoux, P., Pines, D. & Lonzarich, G. G. Superconductivity without Phonons. *Nature* **450,** 1177–1183 (2007).
10. Alireza, P. L. *et al.* Accessing the entire overdoped regime in pristine $YBa_2Cu_3O_{6+x}$ by application of pressure. *Physical Review B* **95,** 100505 (2017).
11. Wolf, B. *et al.* Magnetocaloric Effect and Magnetic Cooling near a Field-Induced Quantum-Critical Point. *Proceedings of the National Academy of Sciences* **108,** 6862–6866 (2011).
12. Wolf, B. *et al.* Magnetic cooling close to a quantum phase transition—The case of $Er_2Ti_2O_7$. *Journal of Applied Physics* **120,** 142112 (2016).
13. Mott, N. *Metal-Insulator Transitions* (CRC Press, 2004).
14. Hubbard, J. & Flowers, B. H. Electron Correlations in Narrow Energy Bands. II. The Degenerate Band Case. *Proceedings of the Royal Society of London. Series A. Mathematical and Physical Sciences* **277,** 237–259 (1964).
15. Ashcroft, N. W. & Mermin, N. D. *Solid State Physics* (Holt, Rinehart & Winston, 1976).
16. Reis, M. *Fundamentals of Magnetism* (Elsevier, 2013).

17. Rowley, S. E. *et al.* Ferroelectric Quantum Criticality. *Nature Physics* **10,** 367–372 (2014).
18. Springford, M. *Electron: A Centenary Volume* Google Books: qUipZ0pXzfQC (Cambridge University Press, 1997).
19. Barrett, J. H. Dielectric Constant in Perovskite Type Crystals. *Physical Review* **86,** 118–120 (1952).
20. Tishin, A. M. & Spichkin, Y. I. *The Magnetocaloric Effect and Its Applications* (CRC Press, 2016).
21. McMichael, R. D., Ritter, J. J. & Shull, R. D. Enhanced magnetocaloric effect in $Gd_3Ga_{5-x}Fe_xO_{12}$. *Journal of Applied Physics* **73,** 6946–6948 (1993).
22. Pecharsky, V. K. & Gschneidner, K. A. Magnetocaloric Effect from Indirect Measurements: Magnetization and Heat Capacity. *Journal of Applied Physics* **86,** 565–575 (1999).
23. *Subtracting the Sample Holder Background from Dilute Samples* MPMS Application Note 1014-213 (Quantum Design, 2002).
24. Brown, P. A. C. *High-Pressure States of Bismuth* Ph.D. Thesis (University of Cambridge, 2017).
25. Coak, M. J. *et al.* SquidLab—A User-Friendly Program for Background Subtraction and Fitting of Magnetization Data. *Review of Scientific Instruments* **91,** 023901 (2020).
26. Filik, J. *et al.* Processing Two-Dimensional X-Ray Diffraction and Small-Angle Scattering Data in DAWN 2. *Journal of Applied Crystallography* **50,** 959–966 (2017).
27. Toby, B. H. & Von Dreele, R. B. GSAS-II: The Genesis of a Modern Open-Source All Purpose Crystallography Software Package. *Journal of Applied Crystallography* **46,** 544–549 (2013).
28. Coelho, A. A. TOPAS and TOPAS-Academic: An Optimization Program Integrating Computer Algebra and Crystallographic Objects Written in C++. *Journal of Applied Crystallography* **51,** 210–218 (2018).
29. Baruchel, J. *Neutron and Synchrotron Radiation for Condensed Matter Studies: Theory, Instruments and Methods* (Springer-Verlag, 1993).
30. Von Dreele, R. B. Quantitative Texture Analysis by Rietveld Refinement. *Journal of Applied Crystallography* **30,** 517–525 (1997).
31. Bunge, H.-J. *Texture Analysis in Materials Science: Mathematical Methods* (Elsevier, 2013).
32. Sitepu, H., O'Connor, B. H. & Li, D. Comparative Evaluation of the March and Generalized Spherical Harmonic Preferred Orientation Models Using X-Ray Diffraction Data for Molybdite and Calcite Powders. *Journal of Applied Crystallography* **38,** 158–167 (2005).
33. Ungár, T. Microstructural Parameters from X-Ray Diffraction Peak Broadening. *Scripta Materialia. Viewpoint Set No. 35. Metals and Alloys with a Structural Scale from the Micrometer to the Atomic Dimensions* **51,** 777–781 (2004).
34. Sheldrick, G. M. A Short History of SHELX. *Acta Crystallographica Section A: Foundations of Crystallography* **64,** 112–122 (2008).

35. Farrugia, L. J. WinGX and ORTEP for Windows: An Update. *Journal of Applied Crystallography* **45,** 849–854 (2012).
36. Ressouche, E. Reminder: Magnetic Structures Description and Determination by Neutron Diffraction. *École thématique de la Société Française de la Neutronique* **13,** 02001 (2014).
37. Yokogawa, K., Murata, K., Yoshino, H. & Aoyama, S. Solidification of High-Pressure Medium Daphne 7373. *Japanese Journal of Applied Physics* **46,** 3636 (2007).
38. Murata, K., Yoshino, H., Yadav, H. O., Honda, Y. & Shirakawa, N. Pt Resistor Thermometry and Pressure Calibration in a Clamped Pressure Cell with the Medium, Daphne 7373. *Review of Scientific Instruments* **68,** 2490–2493 (1997).
39. Eiling, A. & Schilling, J. S. Pressure and Temperature Dependence of Electrical Resistivity of Pb and Sn from 1-300 K and 0-10 GPa - Use as Continuous Resistive Pressure Monitor Accurate over Wide Temperature Range; Superconductivity under Pressure in Pb, Sn and In. *Journal of Physics F: Metal Physics* **11,** 623 (1981).
40. Mao, H. K., Xu, J. & Bell, P. M. Calibration of the ruby pressure gauge to 800 kbar under quasi-hydrostatic conditions. *Journal of Geophysical Research: Solid Earth* **91,** 4673–4676 (1986).
41. Klotz, S. *et al.* Neutron Powder Diffraction at Pressures beyond 25 GPa. *Applied Physics Letters* **66,** 1735–1737 (1995).
42. Klotz, S. *et al.* Advances in the Use of Paris-Edinburgh Presses for High Pressure Neutron Scattering. *Journal of Neutron Research* **21,** 117–124 (2019).
43. Salmon, P. S. *et al.* Pressure induced structural transformations in amorphous $MgSiO_3$ and $CaSiO_3$. *Journal of Non-Crystalline Solids: X* **3,** 100024 (2019).
44. Klotz, S. *Techniques in High Pressure Neutron Scattering* (CRC Press, 2012).
45. Marshall, W. G. & Francis, D. J. Attainment of Near-Hydrostatic Compression Conditions Using the Paris–Edinburgh Cell. *Journal of Applied Crystallography* **35,** 122–125 (2002).
46. Ouvrard, G., Brec, R. & Rouxel, J. Structural determination of some MPS_3 layered phases (M = Mn, Fe, Co, Ni and Cd). *Materials Research Bulletin* **20,** 1181–1189 (1985).
47. Zhukov, V., Alvarez, S. & Novikov, D. Electronic band structure of the magnetic layered semiconductors MPS_3 (M = Mn, Fe and Ni). *Journal of Physics and Chemistry of Solids* **57,** 647–652 (1996).
48. Momma, K. & Izumi, F. VESTA 3 for Three-Dimensional Visualization of Crystal, Volumetric and Morphology Data. *Journal of Applied Crystallography* **44,** 1272–1276 (2011).
49. Wildes, A. R., Rule, K. C., Bewley, R. I., Enderle, M. & Hicks, T. J. The magnon dynamics and spin exchange parameters of $FePS_3$. *Journal of Physics: Condensed Matter* **24,** 416004 (2012).
50. Brec, R. Review on structural and chemical properties of transition metal phosphorous trisulfides MPS_3. *Solid State Ionics* **22,** 3–30 (1986).
51. Lançon, D. *et al.* Magnetic structure and magnon dynamics of the quasi-two-dimensional antiferromagnet $FePS_3$. *Physical Review B* **94,** 214407 (2016).

52. Le Flem, G., Brec, R., Ouvard, G., Louisy, A. & Segransan, P. Magnetic interactions in the layer compounds MPX_3 (M = Mn, Fe, Ni; X = S, Se). *Journal of Physics and Chemistry of Solids* **43,** 455–461 (1982).
53. Rule, K. C., McIntyre, G. J., Kennedy, S. J. & Hicks, T. J. Single-crystal and powder neutron diffraction experiments on $FePS_3$: Search for the magnetic structure. *Physical Review B* **76,** 134402 (2007).
54. Lee, J.-U. *et al.* Ising-Type Magnetic Ordering in Atomically Thin FePS3. *Nano Letters* **16,** 7433–7438 (2016).
55. Wang, Y. *et al.* Pressure-Driven Cooperative Spin-Crossover, Large-Volume Collapse, and Semiconductor-to-Metal Transition in Manganese(II) Honeycomb Lattices. *Journal of the American Chemical Society* **138,** 15751–15757 (2016).
56. Murayama, C. *et al.* Crystallographic features related to a van der Waals coupling in the layered chalcogenide $FePS_3$. *Journal of Applied Physics* **120,** 142114 (2016).
57. Bjarman, S., Jernberg, P. & Wäppling, R. $FePS_3$: A first order phase transition in a "two dimensional" antiferromagnet. *Hyperfine Interactions* **16,** 625–628 (1983).
58. Jernberg, P., Bjarman, S. & Wäppling, R. $FePS_3$: A first-order phase transition in a "2D" Ising antiferromagnet. *Journal of Magnetism and Magnetic Materials* **46,** 178–190 (1984).
59. Wildes, A. R. *et al.* High field magnetization of $FePS_3$. *Physical Review B* **101,** 024415 (2020).
60. Haines, C. R. S. *et al.* Pressure-Induced Electronic and Structural Phase Evolution in the van der Waals Compound $FePS_3$. *Physical Review Letters* **121,** 266801 (2018).
61. Zheng, Y., Jiang, X.-x., Xue, X.-x., Dai, J. & Feng, Y. Ab initio study of pressure-driven phase transition in $FePS_3$ and $FePSe_3$. *Physical Review B* **100,** 174102 (2019).
62. Aruchamy, A., Berger, H. & Levy, F. Photoelectronic properties of the p-type layered trichalcogenophosphates $FePS_3$ and $FePSe_3$. *Journal of Solid State Chemistry* **72,** 316–323 (1988).
63. Coak, M. J. *et al.* Isostructural Mott transition in 2D honeycomb antiferromagnet $V_0.9PS_3$. *npj Quantum Materials* **4,** 1–6 (2019).
64. Lifshitz, E., Francis, A. H. & Clarke, R. An ESR and X-ray diffraction study of a first-order phase transition in $CdPS_3$. *Solid State Communications* **45,** 273–276 (1983).
65. Boucher, F., Evain, M. & Brec, R. Phase transition upon d10 Cd^{2+} ordering in $CdPS_3$. *Acta Crystallographica Section B: Structural Science* **51,** 952–961 (1995).
66. Wang, Y. *et al.* Emergent Superconductivity in an Iron-Based Honeycomb Lattice Initiated by Pressure-Driven Spin-Crossover. *Nature Communications* **9,** 1–7 (2018).
67. Chandrasekharan, N. & Vasudevan, S. Magnetism and exchange in the layered antiferromagnet $NiPS_3$. *Journal of Physics: Condensed Matter* **6,** 4569–4579 (1994).
68. Joy, P. A. & Vasudevan, S. Magnetism in the layered transition-metal thiophosphates MPS_3 (M=Mn, Fe, and Ni). *Physical Review B* **46,** 5425–5433 (1992).
69. Prouzet, E., Ouvrard, G., Brec, R. & Seguineau, P. Room temperature synthesis of pure amorphous nickel hexathiodiphosphate $Ni_2P_2S_6$. *Solid State Ionics* **31,** 79–90 (1988).

70. Wildes, A. R. *et al.* Magnetic structure of the quasi-two-dimensional antiferromagnet $NiPS_3$. *Physical Review B* **92,** 224408 (2015).

71. Lançon, D., Ewings, R. A., Guidi, T., Formisano, F. & Wildes, A. R. Magnetic exchange parameters and anisotropy of the quasi-two-dimensional antiferromagnet $NiPS_3$. *Physical Review B* **98,** 134414 (2018).

72. Bramwell, S. T. & Holdsworth, P. C. W. Magnetization and Universal Sub-Critical Behaviour in Two-Dimensional XY Magnets. *Journal of Physics: Condensed Matter* **5,** L53–L59 (1993).

73. Jenjeti, R. N., Austeria, M. P. & Sampath, S. Alternate to Molybdenum Disulfide: A 2D, Few-Layer Transition-Metal Thiophosphate and Its Hydrogen Evolution Reaction Activity over a Wide pH Range. *ChemElectroChem* **3,** 1392–1399 (2016).

74. Kurita, N. & Nakao, K. Band Structure of Magnetic Layered Semiconductor $NiPS_3$. *Journal of the Physical Society of Japan* **58,** 232–243 (1989).

75. Kurita, N. & Nakao, K. Band Structures and Physical Properties of Magnetic Layered Semiconductors MPS_3. *Journal of the Physical Society of Japan* **58,** 610–621 (1989).

76. Jenjeti, R. N., Kumar, R., Austeria, M. P. & Sampath, S. Field Effect Transistor Based on Layered $NiPS_3$. *Scientific Reports* **8,** 1–9 (2018).

77. Kuo, C.-T. *et al.* Exfoliation and Raman Spectroscopic Fingerprint of Few-Layer $NiPS_3$ Van der Waals Crystals. *Scientific Reports* **6,** 1–10 (2016).

78. Haines, C. R. S. *Pressure Tuned Magnetism in d- and f-Electron Materials* (University of Cambridge, 2011).

79. Nahai-Williamson, P. *Tuning Ordered States in Transition Metal Chalcogenide Systems* (University of Cambridge, 2011).

80. Ressouche, E. *et al.* Magnetoelectric $MnPS_3$ as a candidate for ferrotoroidicity. *Physical Review B* **82,** 100408 (2010).

81. Wildes, A. R., Rønnow, H. M., Roessli, B., Harris, M. J. & Godfrey, K. W. Anisotropy and the critical behaviour of the quasi-2D antiferromagnet, $MnPS_3$. *Journal of Magnetism and Magnetic Materials. Proceedings of the 17th International Conference on Magnetism* **310,** 1221–1223 (2007).

82. Wildes, A. R., Roessli, B., Lebech, B. & Godfrey, K. W. Spin waves and the critical behaviour of the magnetization in $MnPS_3$. *Journal of Physics: Condensed Matter* **10,** 6417–6428 (1998).

83. Wildes, A. R., Rønnow, H. M., Roessli, B., Harris, M. J. & Godfrey, K. W. Static and dynamic critical properties of the quasi-two-dimensional antiferromagnet $MnPS_3$. *Physical Review B* **74,** 094422 (2006).

84. Grasso, V., Neri, F., Santangelo, S., Silipigni, L. & Piacentini, M. Electronic conduction in the layered semiconductor $MnPS_3$. *Journal of Physics: Condensed Matter* **1,** 3337–3347 (1989).

85. Susner, M. A., Chyasnavichyus, M., McGuire, M. A., Ganesh, P. & Maksymovych, P. Metal Thio- and Selenophosphates as Multifunctional van Der Waals Layered Materials. *Advanced Materials* **29,** 1602852 (2017).

86. Brec, R., Schleich, D. M., Ouvrard, G., Louisy, A. & Rouxel, J. Physical Properties of Lithium Intercalation Compounds of the Layered Transition-Metal Chalcogenophosphites. *Inorganic Chemistry* **18,** 1814–1818 (1979).
87. Wang, X. *et al.* Raman spectroscopy of atomically thin two-dimensional magnetic iron phosphorus trisulfide ($FePS_3$) crystals. *2D Materials* **3,** 031009 (2016).
88. Peschanskii, A. V. *et al.* Raman study of a magnetic phase transition in the $MnPS_3$ single crystal. *Low Temperature Physics* **45,** 1082–1091 (2019).
89. Paddison, J. A. M. & Goodwin, A. L. Empirical Magnetic Structure Solution of Frustrated Spin Systems. *Physical Review Letters* **108,** 017204 (2012).
90. Paddison, J. A. M., Stewart, J. R. & Goodwin, A. L. Spinvert: A Program for Refinement of Paramagnetic Diffuse Scattering Data. *Journal of Physics: Condensed Matter* **25,** 454220 (2013).
91. Evarestov, R. A. & Kuzmin, A. Origin of pressure-induced insulator-to-metal transition in the van der Waals compound $FePS_3$ from first-principles calculations. *Journal of Computational Chemistry* **41,** 1337–1344 (2020).
92. Köhler, J., Dinnebier, R. & Bussmann-Holder, A. Structural instability of $EuTiO_3$ from X-ray powder diffraction. *Phase Transitions* **85,** 949–955 (2012).
93. Allieta, M. *et al.* Role of intrinsic disorder in the structural phase transition of magnetoelectric $EuTiO_3$. *Physical Review B* **85,** 184107 (2012).
94. Kim, J.-W. *et al.* Emergent Superstructural Dynamic Order due to Competing Antiferroelectric and Antiferrodistortive Instabilities in Bulk $EuTiO_3$. *Physical Review Letters* **110,** 027201 (2013).
95. Goian, V. *et al.* Antiferrodistortive phase transition in $EuTiO_3$. *Physical Review B* **86,** 054112 (2012).
96. Bussmann-Holder, A., Köhler, J., Kremer, R. K. & Law, J. M. Relation between structural instabilities in $EuTiO_3$ and $SrTiO_3$. *Physical Review B* **83,** 212102 (2011).
97. Spalek, L. J. *Emergent Phenomena Near Selected Phase Transitions* Ph.D. Thesis (University of Cambridge, 2013).
98. Shvartsman, V. V., Borisov, P., Kleemann, W., Kamba, S. & Katsufuji, T. Large off-diagonal magnetoelectric coupling in the quantum paraelectric antiferromagnet $EuTiO_3$. *Physical Review B* **81,** 064426 (2010).
99. Katsufuji, T. & Takagi, H. Coupling between magnetism and dielectric properties in quantum paraelectric $EuTiO_3$. *Physical Review B* **64,** 054415 (2001).
100. Chien, C.-L., DeBenedetti, S. & Barros, F. D. S. Magnetic properties of $EuTiO_3$, Eu_2TiO_4, and $Eu_3Ti_2O_7$. *Physical Review B* **10,** 3913–3922 (1974).
101. McGuire, T. R., Shafer, M. W., Joenk, R. J., Alperin, H. A. & Pickart, S. J. Magnetic Structure of $EuTiO_3$. *Journal of Applied Physics* **37,** 981–982 (1966).
102. Wu, H. & Shen, W. Z. Magnetoelectric effect in perovskite quantum paraelectric $EuTiO_3$. *Solid State Communications* **133,** 487–491 (2005).
103. Hill, N. A. Why Are There so Few Magnetic Ferroelectrics? *The Journal of Physical Chemistry B* **104,** 6694–6709 (2000).

104. Caslin, K. *et al.* Lattice and polarizability mediated spin activity in $EuTiO_3$. *Journal of Physics: Condensed Matter* **26,** 022202 (2013).

105. Midya, A. *et al.* Large adiabatic temperature and magnetic entropy changes in $EuTiO_3$. *Physical Review B* **93,** 094422 (2016).

106. Petrović, A. P. *et al.* Electric field modulation of the tetragonal domain orientation revealed in the magnetic ground state of quantum paraelectric $EuTiO_3$. *Physical Review B* **87,** 064103 (2013).

107. Scagnoli, V. *et al.* $EuTiO_3$ magnetic structure studied by neutron powder diffraction and resonant x-ray scattering. *Physical Review B* **86,** 094432 (2012).

108. Jiang, Q. & Wu, H. Magnetic influence on frequency of soft-phonon mode in incipient ferroelectric $EuTiO_3$. *Journal of Applied Physics* **93,** 2121–2125 (2003).

109. Fennie, C. J. & Rabe, K. M. Magnetic and Electric Phase Control in Epitaxial $EuTiO_3$ from First Principles. *Physical Review Letters* **97,** 267602 (2006).

110. Lee, J. H. *et al.* A Strong Ferroelectric Ferromagnet Created by Means of Spin-Lattice Coupling. *Nature* **466,** 954–958 (2010).

111. Mo, Z.-J. *et al.* Observation of giant magnetocaloric effect in $EuTi_{1-x}Cr_xO_3$. *Journal of Alloys and Compounds* **649,** 674–678 (2015).

112. Rubi, K., Midya, A., Mahendiran, R., Repaka, D. V. M. & Ramanujan, R. V. Magnetocaloric properties of $Eu_{1-x}La_xTiO_3$ $(0.01 \leq x \leq 0.2)$ for cryogenic magnetic cooling. *Journal of Applied Physics* **119,** 243901 (2016).

113. Parisiades, P., Liarokapis, E., Köhler, J., Bussmann-Holder, A. & Mezouar, M. Pressure-temperature phase diagram of multiferroic $EuTiO_3$. *Physical Review B* **92,** 064102 (2015).

114. Guguchia, Z. *et al.* Nonlinear pressure dependence of T_N in almost multiferroic $EuTiO_3$. *Journal of Physics: Condensed Matter* **25,** 376002 (2013).

115. Katsufuji, T. & Tokura, Y. Transport and magnetic properties of a ferromagnetic metal: $Eu_{1-x}R_xTiO_3$. *Physical Review B* **60,** R15021–R15023 (1999).

116. Schiemer, J. *et al.* Magnetoelastic relaxations in $EuTiO_3$. *EPL (Europhysics Letters)* **109,** 57004 (2015).

117. Schiemer, J. *et al.* Magnetic field and in situ stress dependence of elastic behavior in $EuTiO_3$ from resonant ultrasound spectroscopy. *Physical Review B* **93,** 054108 (2016).

118. Narayan, A., Cano, A., Balatsky, A. V. & Spaldin, N. A. Multiferroic Quantum Criticality. *Nature Materials* **18,** 223–228 (2019).

119. Wiedenmann, A., Rossat-Mignod, J., Louisy, A., Brec, R. & Rouxel, J. Neutron diffraction study of the layered compounds $MnPSe_3$ and $FePSe_3$. *Solid State Communications* **40,** 1067–1072 (1981).

120. Morice, C., Chandra, P., Rowley, S. E., Lonzarich, G. & Saxena, S. S. *Hidden Fluctuations Close to a Quantum Bicritical Point* arXiv: 1611.04621 `[cond-mat]`.

121. Alireza, P. L. & Julian, S. R. Susceptibility Measurements at High Pressures Using a Microcoil System in an Anvil Cell. *Review of Scientific Instruments* **74,** 4728–4731 (2003).

122. Ko, Y. T. C. *Search for Unconventional Superconductivity in Transition Metal Compounds* Ph.D. Thesis (University of Cambridge, 2011).

123. Acosta, V. M. *et al.* Color Centers in Diamond as Novel Probes of Superconductivity. *Journal of Superconductivity and Novel Magnetism* **32,** 85–95 (2019).

124. Lesik, M. *et al.* Magnetic Measurements on Micrometer-Sized Samples under High Pressure Using Designed NV Centers. *Science* **366,** 1359–1362 (2019).